Electrical readout of orbital state transitions from fewer hydrogenic donors in silicon

Kristian Stockbridge

Advanced Technology Institute
University of Surrey

A thesis submitted to the Department of Physics in partial fulfilment of the degree of Doctor of Philosophy in Physics

2022

Abstract

Atomic defects in semiconductors have been studied as promising platforms for quantum technological applications in the solid state. The electron and nuclear spins of single substitutional group-V donor atoms in silicon are of particular interest due to their long quantum coherence times and potential ease of integration with already well established microelectronics fabrication technology. The donor electrons, when bound to group-V donor nuclei at low temperature, have not only quantised intrinsic spin but quantised orbital angular momentum. For donors in silicon, transitions between the allowed orbital states are accessible via THz excitation and the extent of the excited orbital wave function is large inspiring their use to gate interaction between neighbouring spin qubits. This body of work seeks to investigate the electrical detection of the orbital excitation dynamics of scaled down silicon devices whereby orbital excitation is of few defects.

Prior to fabrication of electrical devices that will require deterministic and precise placement of single donor atoms, it is worth checking that gated qubit interactions can't be realised in a system that might be far easier to fabricate e.g. one where dopants exist homogeneously in the bulk or are broad area ion implanted. A particular gating scheme whereby qubit entanglement is dependant on the orbital state of an intermediary donor has been proposed historically. In this thesis the viability of an even simpler system of orbitally gated interaction being achieved by a number of broad area ion implantations is investigated using point process statistics and the need for higher positional determinism in dopant placement realised.

The next investigation is of isolated donors present at a background concentration level in highly purified silicon wafer. Though not deterministically placed, the quantum coherence dynamics of these donors can be probed electrically via contactless photocurrent detection. The coherent dynamics of the donor ensemble subjected to a large external magnetic field was measured using Ramsey spectroscopy. External magnetic fields are typically used in spin qubit systems to lift the energy degeneracy of spin-up and spin-down states of the electron.

Finally, resistive photoconductance spectroscopy was performed on a bismuth ion implanted silicon-on-insulator (SOI) device containing <1 million defects in the optically active region of the device. The high electric fields that are more easily accessible in short channel devices is shown to introduce additional ionisation mechanisms that could aid in characterising donor orbital state transition dynamics at lower temperatures. The significant inhomogeneous broadening seen in the measured device photocurrent spectrum was attributed to the high density of active bismuth donors.

Acknowledgements

I would like to thank all of those who have be there throughout the duration of these studies. Primarily my PhD supervisors, Prof. Ben Murdin and Dr. Steven Clowes who foster a welcoming, stimulating and enjoyable research environment.

I am extremely grateful for the time and effort others have given to support the work contained. The discussions with Dr Eleanor Crane and Prof. Andrew Fisher particularly helped shaped the point process statistical analysis presented. The experimental work carried out at the FELIX facility would have been impossible without the expertise of the amazing beam-line and research staff. In particular I would like to thank Dr Nils Dessmann, Dr Viktoria Eless and Dr. Kamyar Saeedi for their support during shifts and their preparation time prior to upcoming shifts. I am also extremely grateful for the support of my research peers within the COMPASSS/ADDRFESS group who have been unhesitating in sharing their advice, support and friendship: Dr Steven Chick, Dr Tom Peach, Dr Gemma Chapman, Dr Nathan Cassidy, Dr Jess Smith, Dr David Cox and Dr Mateus Masteghin.

Finally, I would like to thank my friends, family and partner for their continued support and encouragement throughout my PhD. Without you this would not have been possible.

Dissemination

K. Stockbridge, S. Chick, E. Crane, A. Fisher, B. N. Murdin "Using non-homogeneous point process statistics to find multi-species event clusters in an implanted semiconductor" *J. Phys. Commun.* **4**(1) 015010 (2020)

T. Peach, K. Stockbridge, J. Li, K. Homewood, M. Lourenco, S. Chick, M. Hughes, B. Murdin, S. Clowes "Enhanced diffusion and bound exciton interactions of high density implanted bismuth donors in silicon" *Applied Physics Letters.* **115**(7) 072102 (2019)

C. Eleanor, C. Thomas, S. Alexander, H. L. Nguyen, K. Stockbridge, S. Chick, A. J. Fisher "Optically controlled entangling gates in randomly doped silicon" *Phys. Rev. B.* **100**(6) 064201 (2019)

K. Stockbridge, N. Dessmann, V. Eless, T. Peach, B. N. Murdin, S. Clowes "Photoassisted ionisation spectroscopy of few implanted bismuth orbitals in a silicon-on-insulator device" *Applied Physics Letters.* **120**(7) 073503 (2022)

Conference talk: K. Stockbridge et al. "Novel measurement of Si:P orbital dynamics at high field using FELIX+HFML" *Silicon Quantum Electronics Workshop* (2021)

Poster presentation: K. Stockbridge et al. "Using non-homogeneous point process statistics to find multi-species event clusters in an implanted semiconductor" *Silicon Quantum Electronics Workshop* (2019)

Poster presentation: K. Stockbridge et al. "Using non-homogeneous point process statistics to find multi-species event clusters in an implanted semiconductor" *Silicon Quantum Information Processing* (2018)

Statement of originality

This thesis and the work to which it refers are the results of my own efforts. Any ideas, data, images or text resulting from the work of others (whether published or unpublished) are fully identified as such within the work and attributed to their originator in the text, bibliography or in footnotes. This thesis has not been submitted in whole or in part for any other academic degree or professional qualification. I agree that the University has the right to submit my work to the plagiarism detection service TurnitinUK for originality checks. Whether or not drafts have been so-assessed, the University reserves the right to require an electronic version of the final document (as submitted) for assessment as above.

Kristian Stockbridge December 2022

Contents

List of Figures

List of Tables

Chapter 1

Introduction

Silicon based electronics has been at the forefront of the electronics industry since the early 20th century. The technological advances to lithographically fabricate electronic circuits on high purity semiconducting materials has allowed integrated circuits to reduce in size in accordance with the predictions of Gordon Moore in 1965 and 1975. Initially it was predicted that the number of components possible in an integrated circuit of a given size would double every year [1]. This projection was then reevaluated a decade later to be half as rapid as initially predicted [2]. This later prediction of doubling every two years held true for the remainder of the 20^{th} century and became known as Moore's law.

Solid state transistors are one of the most critical components in modern electronics. Their use as voltage controlled switches with high power efficiency and small physical size in digital electronics revolutionised computational speed and efficiency. The metal-on-silicon field effect transistor (MOSFET), invented in 1959, was the first transistor design that could be mass produced using what have since become industry standard lithographic techniques. One of the many challenges in packing larger numbers of transistors in integrated circuits is in defining channels with shorter gate lengths [3]. A gate terminal that is used to induce an electric field in the channel controls the flow of current between a source and drain terminal. Below channel lengths of around 10 nm it becomes increasingly difficult to switch that current off. This is because at these length scales quantum mechanical tunnelling of electrons directly from the source to the drain electrodes becomes increasingly probable regardless of the potential barrier height in the channel separating them. Advances in transistor designs such as the tri-gate geometry of FinFETs [4] whereby the gate electrode wraps around the channel, increasing the area of contact between the channel and gate by touching three sides of the channel rather than one. This has helped to further reduce the transistor channel length to 10 nm but a limit is reached where feature sizes approach the length scales of silicon-silicon bonds by which point conventional field effect transistor (FET) behaviour is not to be expected.

The quantum nature of nanoscale semiconducting devices has been embraced by the scientific community due to the opportunities such devices present for novel paradigms in electronics such as quantum computing, sensors and technologies that rely on state entanglement, superpositions of states or tunnelling effects.

1.1 Quantum computing in the solid state

Some basic concepts of quantum computing were first mentioned in a lecture given by Richard Feynman in 1959 [5] stating with regards to miniaturising computer circuitry, “We can use, not just circuits, but do some system involving the quantized energy levels, or the interactions of quantized spins”. There have been, and still are, many ideas for what states could be used and in what systems for quantum information processing. The general principles required for successful implementation for a quantum computer were outlined by DiVincenzo [6] in 2000. To physically implement a functional quantum computer which outperforms a classical computer in the ways predicted has proved to be a great engineering difficulty. In a quantum computer, information is stored in the form of superposition states of quantised energy levels, for two states this is referred to as a quantum bit or ‘qubit’ of information in analogy with classical, binary information stored as ‘bits’. With their ability to represent more than one state at a point in time, a suitable system of entangled qubits could solve problems that would take a classical computer an unreasonable amount of time to complete. Typical examples include Shor’s algorithm for integer factorisation [7] and Grovers algorithm for fast database search [8]. There are many investigated physical qubit implementations. These include: photon polarisation [9], charge flux in superconducting resonators [10,11], atomic spins in optically trapped atoms [12] and charge state of quantum dots [13,14].

There are many different qubit systems being studied which satisfy the DiVincenzo criteria. State-of-the-art systems of particular interest include: photonic qubits which are potentially free from decoherence but difficult to make entangle [15], superconducting qubits which are relatively simple to manufacture but prone to decoherence from electronic noise [10], topological qubits that are potentially very resistant to noise but are yet to be experimentally confirmed [16], and (free space) atomic qubits which [12] which have very long coherence times but are difficult to scale to systems of many qubits. The atomic qubits systems of interest in this thesis are those of solid state trapped atom qubits, specifically substitutional group-V donor atoms trapped in a silicon lattice. Even with this specific a system there are many options for qubit manifestations. The spin states of donor nuclei [17] and spins of donor bound electrons [18] are popular choices due to their long coherence times. Other options are the orbital states of the bound electrons or the charge states of quantum dots defined with gate electrodes [14] or single donors [19,20]. Silicon as a host for fabricating quantum devices is a convenient one because of the amount of research and advances made in improving classical computing hardware power via the miniaturisation of transistors. Many of the processing techniques used for making classical computers on a commercial scale are appropriate for fabricating at least parts of the circuitry involved in quantum processing.

Crystalline silicon is an indirect band gap semiconductor with a diamond cubic lattice whereby the four valence electrons of each atom are covalently bonded to four nearest neighbours silicon atoms in a tetrahedral arrangement. Replacing a silicon atom in this structure with an atom with five valence electrons results in one electron not used for bonding to the neighbouring silicon atoms. There remains a Coulomb attraction between the extra electron and the donor nucleus however the 4 electrons involved in the covalent bonding ‘screen’ the additional electron from all but one of the five protons. Provided the lattice temperature is low enough, the excess donor electron remains bound to the donor nucleus, trapped in the Coulomb potential well surrounding a single lattice site. This looks very similar to a hydrogen atom, only fixed in place in the silicon lattice.

Silicon provides a convenient substrate for solid state quantum information processing due to its low concentration of nuclear spins. Atoms in a substrate that have non-zero nuclear spin can interact with qubit spin states via the magnetic dipole-dipole interaction and have the effect of reducing the coherence time of a prepared superposition state thus limiting the available time in which one can complete a quantum computation. While the radioactively stable silicon isotopes ^{28}Si and ^{30}Si have the desired property of no nuclear spin, ^{29}Si has non-zero nuclear spin, $I = 1/2$, is also a stable isotope and comprises 4.67 % of naturally occurring silicon on Earth. For this reason it helps to produce isotopically enriched silicon, reducing the content of ^{29}Si, in preparation for its use in quantum technologies involving preserved spin superpositions. [21]

1.1.1 The Kane architecture

One of the most well known proposals for a Silicon-based quantum computer is the Kane quantum computer [17]. In this system an array of phosphorus donors (with nuclear spins $I = 1/2$) is placed in isotopically pure ^{28}Si and subjected to an external magnetic field to lift the degeneracy of donor nuclear and donor electron spin states.

The polarisation of nuclear and electron spins of the phosphorus donor are involved in this architecture. The well isolated nuclear spins store the qubit information with a coherence time measured to be greater than half an hour [22]. This state can be manipulated using RF electromagnetic pulses. The electrons are used to entangle the states of nearby nuclei. The so-called hyperfine interaction that couples the donor nuclear spin state to that of the electron is controlled by a gate electrode in the proximity of each donor. These gates are also critical for addressing individual nuclei to be in resonance with applied RF pulses that prepare their initial state. With the qubit now encoded in the electron spin, quantum entanglement can occur between neighbouring electron spins by enabling a spin-exchange interaction between them. Such an interaction is dependent on the distance between the spins. This is controlled by another gate located between the two phosphorus atoms. The time in which this must take place is now limited by the coherence time of the electron spin state which is reported to be as high as 10 s [23]. The information is then restored in the nuclear spin. Eventually, at the end of a quantum computation, when readout of a nuclear spin state is required, the polarisation is transferred again to the electron whose spin state can be measured from a spin-to-charge readout technique e.g. spin dependent tunnelling into a nearby quantum dot [24].

There is clearly a great engineering barrier to overcome in this architecture. This device requires the deterministic placement of phosphorus donors roughly 10 nm deep into an isotopically pure silicon sample. This depth must be deep enough that the bound electrons are isolated from the silicon surface but not so deep that surface patterned electrodes cannot address individual qubits. The metal gate electrodes must be placed in alignment with those donors with dimensions and separations also on the order of 10 nm. Individually, these criteria are achievable with modern fabrication techniques however none that are currently scalable to systems of many entangled qubits. Examples of techniques to introduce deterministically positioned single donors are hydrogen resist lithography and single ion implantation, both described later in this section. Each of these techniques presents their own difficulties but in principle positioning donors with sub-10 nm accuracy is possible.

In Si, the precise positioning of neighbouring donor qubits is made even more strict by the inter-valley interference causing the donor bound electron wave function to oscillate in magnitude with a periodicity comparable to the lattice spacing [25]. This interference effect arises due to the location of the conduction band minima in the silicon electronic band structure. The six, energy degenerate, conduction band minima exist 85% of the way between the central Γ point and the X point boundaries of the Brillouin zone. This effect is less apparent for adjacent donor electron orbitals in Ge as the conduction band minima are located at the L points of the Brillouin zone boundary.

The placement of correctly aligned gates on the silicon surface is also challenging even given cutting edge electron beam lithography (EBL) [26] and helium ion beam lithography (HIBL) [27] techniques to create exceedingly small features in lithographic masks prior to metal deposition and lift-off. Isotopic enrichment of silicon has been achieved by chemical vapour deposition of ^{28}Si followed by float zone (FZ) recrystallisation [28]. Since only the silicon close to the surface needs to be isotopically pure, other techniques to form ^{28}Si using readily available natural silicon wafers are also being explored. [29,30]

1.1.2 A gating scheme using silicon donor orbital states

Another proposed method of implementing entangled donor qubits in silicon is the Stoneham Fisher Greenland (SFG) scheme [31]. In this scheme, electron spin entanglement is gated not with an intermediate electrode but by orbital excitation of an intermediate donor impurity. Such an excitation increases the electron orbital radius and therefore increases the amount its wave function overlaps with those of the two neighbouring qubits whose spins are desired to be entangled. A schematic of this arrangement is depicted in fig. 1.1. This is possible because not only does the electron bound to the donor nucleus have intrinsic spin, but because the centre is hydrogenic, it has orbital states and a Lyman series of atomic transitions analogous to those of atomic hydrogen with caveats arising due to the surrounding Si lattice.

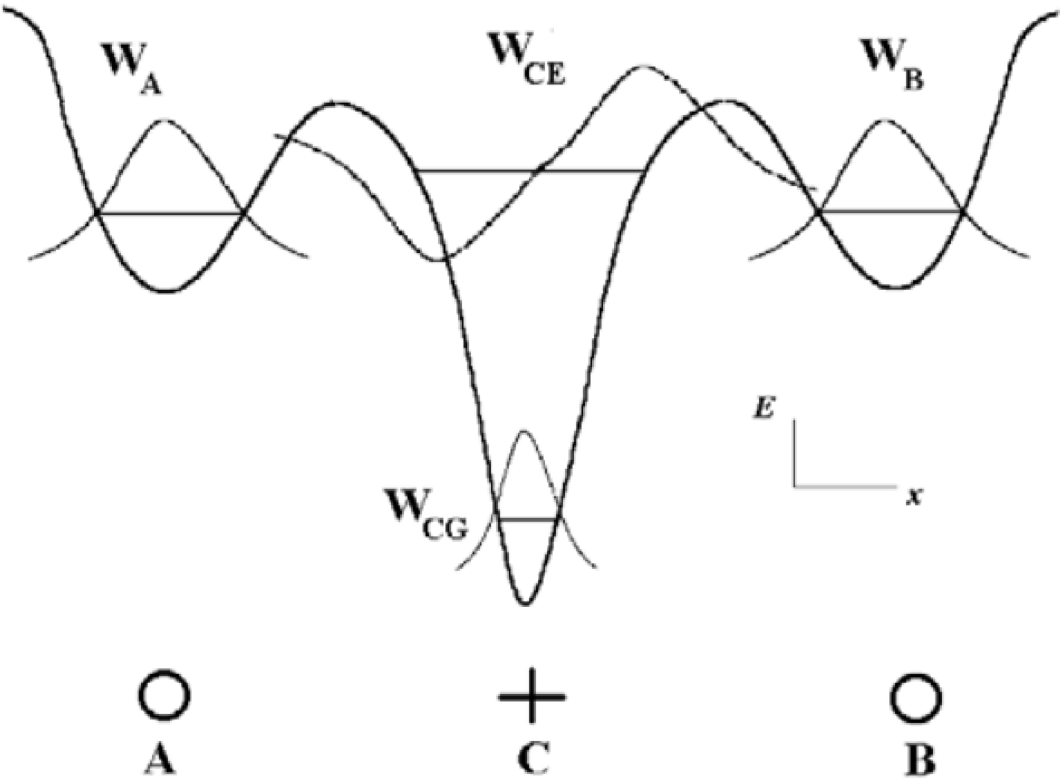

Figure 1.1: The proposed optical gating of spin entaglement as shown in [31]. A control impurity, C when in its excited orbital state, enables entanglement between neighbouring qubits A and B.

Silicon is an indirect band gap semiconductor with a conduction band minimum that is sixfold degenerate due to six equivalent valleys close to the X-points of its Brillouin zone. A substitutional donor in this crystal environment has a $1s$ ground state orbital that would be spherically symmetric if it were not perturbed by the surrounding lattice. Valley-orbit coupling occurs due to the disturbance the defect ion has on the cubic symmetry of the tetrahedral lattice and results in the ground state splitting into 3 distinct energy states $1s(A_1, T_2, E)$ (singlet, triplet and doublet states respectively). For donors in silicon, the $1s(A_1)$ state is the most tightly bound. [32] It is also the state whose binding energy is most affected by the particular group-V donor species since it has a large charge density near the donor site where the reduced charge screening of the nucleus by the donor inner shell electrons makes it appear less like a simple point charge at the donor lattice cite.

The radii of the donor-bound electron orbitals are much larger than those of atomic hydrogen in vacuum due to the smaller effective mass of the electron and the increased electric permittivity. From the Bohr model of atomic hydrogen, the radius of the ground state, $a_0 \propto \epsilon_0/m_e$ so with an electric permittivity roughly ten times that of vacuum and an effective mass a fifth of that in vacuum, the electron orbital states of a hydrogenic donor in silicon extend 50× further away from the nucleus than they would in atomic hydrogen. This means the Bohr radius of a hydrogenic donor is on the order of nanometres rather than 10s of picometres. The excited state radii scale with the square of the principle quantum number resulting in radii comparable to the resolution of modern semiconductor fabrication technology. As mentioned in the previous section, inter-valley interference also occurs particularly for donors in bulk silicon.

These caveats: that the electron orbitals are large, and that the orbital transition energies from the ground, $1s(A_1)$ state are species dependent are both exploited in the SFG scheme. The intermediate, ‘control’ donor species can be optically excited leaving the neighbouring ‘memory’ donors unaffected. Since the intermediary donor excited orbital states extend far, the spacing of the multi-species cluster can also be larger thus relaxing the neighbouring distance constraints. A high order excited state of the control donor can overlap with two well separated memory qubits and increase the exchange energy between them to cause a spin entanglement. In the original article [31] it is also claimed that the control elements may also be used for all-optical readout further simplifying the engineering requirements.

In both the Kane and SFG architecture implemented with donors in silicon, absolute control of the electron spin entanglement requires atomic positioning of the donors due to inter-valley interference. Despite this inconvenience, test-bed devices fabricated with coarser control of donor placement remain useful to try to produce such that other features of such a quantum device may be optimised. For example the time that a gating donor orbital remains in its excited state will determine how long neighbouring spins can interact. If such an interaction time can be made very long it may not matter that two qubits were not positioned with absolute accuracy as the intermediate gating orbital can be kept in its excited state for longer to compensate for such errors.

1.2 Motivation for deterministic shallow dopant incorporation into silicon

The ability to introduce a controlled density of extrinsic dopants into high purity silicon wafer is critical to the microelectronics industry even for classical electronics applications. On a single piece of silicon, regions doped with a controlled density of group-V donors and group-III acceptors can be defined to form well characterised circuitry at a length scale and power efficiency impossible using previous, thermionic valve technology. Silicon is therefore an extremely convenient platform for commercial quantum technologies due to the vast infrastructure for growing and doping very high purity silicon.

There are two commonly used methods to grow single crystals of silicon. The most economical of the two involves dipping a seed crystal of known crystallographic orientation into a crucible of molten silicon and slowly extracting it. This process, capable of growing large boules of single crystal silicon is called the Czochralski (CZ) method. During the growth of CZ silicon, donor and/or acceptor defects can be introduced via their addition to the crucible of liquid silicon to control the electronic properties of the final wafers. One possible downside with this growth method for quantum information applications is that oxygen and carbon defects are easily introduced into the crystal through contact with the crucible. These impurities can interact with the donor qubits and reduce coherence times. The common alternative growth method, is the FZ method. In this method a single crystal is produced by inductively melting the cross-section of a high purity polycrystalline rod, dipping the seed crystal into that and dragging the molten zone along the length of the rod. In the wake of the molten zone, the silicon recrystallises in a single orientation. By avoiding contact with a crucible and since impurities are dragged away by the moving molten zone, a high purity crystalline silicon boule can be grown free of dissolved defects such as oxygen.

Introducing substitutional dopants in the wafer bulk at the time of boule growth undoubtedly yields the best quality of doped silicon in terms of vacancy (unoccupied lattice sites) and interstitial (atom trapped in space between lattice sites) defect concentration. There is, however, no control over where the dopants exist as substitutional defects in the lattice; a homogeneously random dopant concentration (where the probability of finding a donor at any particular lattice site is uniform) over the entire wafer volume is achieved. To fabricate devices for single donor qubit applications such as the Kane quantum computer or SFG scheme, one must start with a dopant free silicon crystal and have control over the position of donors to control their separations. The simplest method worth exploring, only slightly more deterministic than bulk doping, is broad area ion implantation. By accelerating a beam of ions of the desired species towards a high purity silicon wafer a layer of that species is incorporated with a concentration profile centred at a mean depth. Due to random collisions with the lattice on entry and depending on the implant energy, the distribution of the dopant density can be very broad in depth. Beam acceleration energies used are typically in the range of 10 keV to 1000 keV to control the depth of an implanted layer. The final concentration of implanted species is controlled by the exposure time. This process, depending on the ion mass and kinetic energy, can significantly damage and even fully amorphize the crystal surface. To repair this damage and substitutionally incorporate the implanted atoms, annealing is required. Though this method provides some control over the dopant density in one dimension, it still results in homogeneous random doping in the other two.

Single ion implantation (SII) is a technique that addresses the lack of control over donor placement in broad area ion implantation. Positional accuracy is achieved in various ways. Some possibilities are: implanting onto the exposed windows of a hard mask [33] or by focussing the ion beam into a small spot size on the target surface. [34] The latter example is advantageous as it does not rely on the additional processing to define an implant mask. Despite a finite spot size limiting positional accuracy in the latter example, implant straggle also causes the ion to deviate from the initial position due to collisions with the lattice. Although not accurate to the exact lattice site, SII can provide good control (on the order of 10 nm) of dopant placement in all three dimensions.

For SII to be deterministic also in regards to the number of ions implanted one must improve upon the Poisson statistics describing the average number of ions in a beam over a given exposure time. If a target is exposed to an ion beam containing on average one ion there is a significant probability of implanting no or more than one ions making it difficult to define a pattern of many single ions. To overcome this, a successful implantation event can be detected to determine when to stop implanting into a particular location. [34,35] It is also possible to count and blank ions in the beam prior to collision with the target [36]. Implant event detection could be done by detecting secondary electrons ejected from the surface upon impact or even implanting into a device sensitive to the free charge carriers and/or damage created during an ion impact. [37,38] To reliably prevent more than one ion being implanted low current beams are used. The ion beam may be pulsed such that when eventually a pulse contains a non zero number of ions it is highly unlikely that it contained more than one. Using this method it is possible to create clusters and arrays of many accurately positioned single dopants of a vast selection of species.

In principle, any species that can be broad area implanted can be used in a single ion implanter although critical factors such as the positional accuracy will depend on the ion species and target material.

The method which achieves the highest spatial accuracy and precision of dopant impurities in semiconductors is hydrogen lithography. [39,40] Hydrogen lithography relies on the selective removal of hydrogen atoms from a target surface such that dopants existing in a precursor gas may incorporate at the exposed dangling bonds. The spatial precision of hydrogen lithography is limited by the ability to remove single hydrogen atoms with a scanning tunnelling microscope (STM) tip, and also by the number of dangling bonds required to remove for the surface chemistry dictating successful incorporation to work (usually more than one dangling bond must be exposed as is the case for phosphorus [40] and arsenic [41] on a <100> silicon surface). An encapsulating layer of the substrate material can then be grown over the doped layer to achieve the required depth. This incorporation method is non-destructive to the underlying substrate unlike the comparably violent process of ion implantation however there are currently very few species that can be incorporated with this method.

1.3 Manipulation and readout of group-V donor orbital states

No matter which method is used to incorporate the donors, it is critical to assess the quality of donor incorporation to determine its suitability in a proposed quantum computation scheme such as the Kane architecture or SFG scheme as introduced here. For the SFG scheme, not only must the spin states of the so called memory donors be well characterised but also the orbital states of the control donor. These orbital states are characteristic of electrically active neutral donors in a pristine crystalline environment.

For shallow donors in silicon to rest in their ground state the lattice temperature must be low enough that electrons are not thermally excited into higher energy orbitals. This is typically achieved at temperatures below 20 K requiring the use of liquid helium cooling. This upper temperature limit is such that the thermal energy $k_B T$ is no greater than the lowest energy transition. Whereas atomic hydrogen has a Lyman series accessible in the ultraviolet spectral region, the analogous transitions for hydrogenic donor centres in silicon exist in the far infrared region within the so-called 'THz gap' as depicted in fig. 1.2. So called because of the limited choice of light sources that emit with high power in this range.

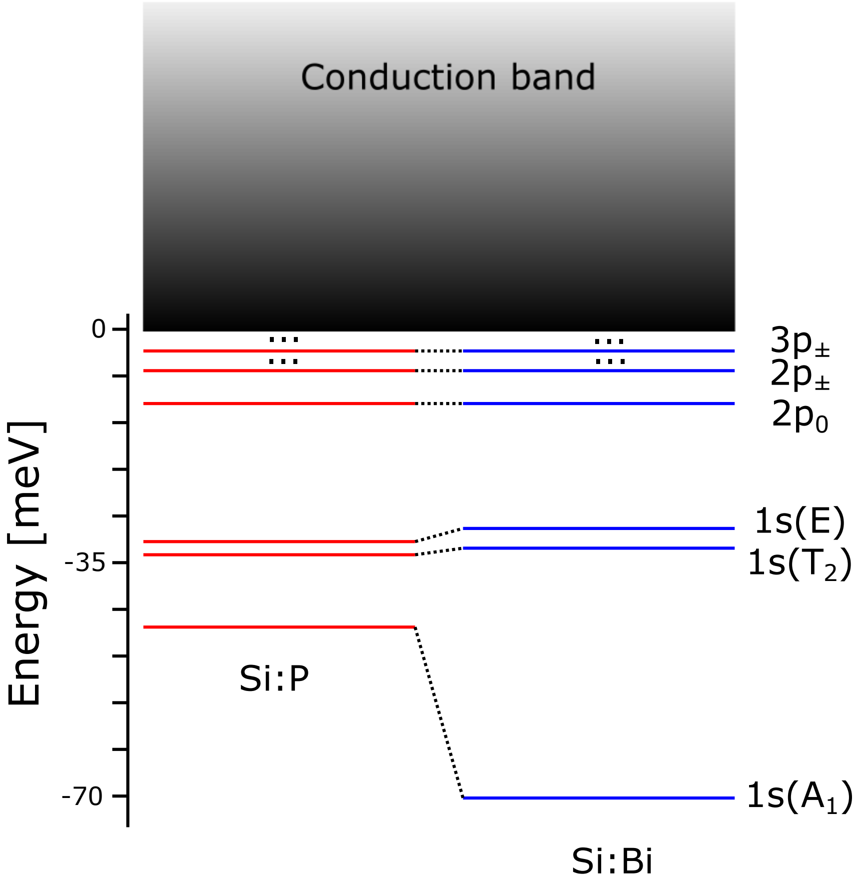

Figure 1.2: Orbital binding energies of phosphorus and bismuth donors in silicon. Ellipses denote where some states have been omitted from this illustration.

To detect the excitation from ground to excited orbital state for hydrogenic donors in silicon the transmission of light through the sample can be observed, simply whether or not photons of a particular wavelength are absorbed by the material is sufficient to determine whether or not an allowed optical transition exists. Measuring the amount of light able to transmit through the sample requires the use of a photodetector sensitive in this energy range down-stream of the absorbing sample. For samples containing a low number of absorbers relative to the number of photons in the beam, low signal to noise becomes an issue and the difference between the amount of transmitted light on and off-resonance is exceedingly small.

To achieve a higher signal to noise measurement of few absorbers one can fabricate a detector out of the sample containing the absorbers in a known location and measure a change in electrical properties of that region under illumination. In this measurement photons that don't interact with absorbers are not detected in the electrical signal making it background free. For the orbital states of donors in silicon the present most sensitive method, capable of detecting transitions from the lowest density of donors, is photo-thermal ionisation spectroscopy (PTIS) for which a full description is found in chapter 2. This technique relies on the preferential ionisation of excited orbital state electrons after photo-excitation causing an increase in the density of free carriers thus changing the electrical resistance of a sample. Due to their potential use in silicon quantum technologies, measurement and characterisation of orbital transitions of single donors in a device is desired but has yet to be demonstrated. Characterisation of donor orbital transitions in bulk doped samples containing a low density of dopants have however been extensively studied.

The dynamics of donor orbital excitation are also critical to their use in gating an interaction between neighbouring spin qubits. Precisely how long an excited electron stays in this state is clearly important. For full control of the superpostition of a donor orbital ground and excited state one requires a pulsed, high intensity, coherent light source. Currently the only viable option to do this is with a pulsed THz free electron laser (FEL). Other available sources of THz are either the wrong wavelength, too low intensity or too spectrally broad. With pulses of coherent light, an arbitrary superposition state of a two level system with a well defined phase can be achieved. Using pulsed spectroscopy methods e.g. Ramsey spectroscopy the relaxation and dephasing times of a two level system can be measured. Again, this has been studied predominantly in samples containing a low bulk concentration of donors. By moving towards samples containing fewer donors though, dephasing effects that arise due to an ensemble of oscillators (i.e. inhomogeneous broadening effects) are removed. Inhomogeneous broadening has been shown to be the dominant decoherence mechanism for donor orbital transitions. [42] By removing the distribution of resonant frequencies for a particular transition which causes this line broadening by having only one oscillator in the system would be ideal. This also has not been demonstrated in a doped silicon sample.

1.4 Thesis summary and outline

In this chapter, the field of solid state quantum computing has been introduced with particular emphasis on systems of donors in silicon whereby donor spin entanglement is gated by orbital excitation. Some methods of doping silicon with increasing control of donor placement are introduced as it is this control that determines the probability of finding suitable multi-species clusters in a doped sample. The need to characterise the orbital state time dynamics of systems of fewer donors is introduced as ultimately these systems of few donors are those required to build a trapped atom quantum computer in the solid state. The time dynamics of orbital transitions in an ensemble of donors can be very different due to inhomogeneous broadening effects.

Chapter 2 contains a detailed description of the experimental techniques used in this thesis (in chapters 4 and 5) to assess the incorporation of donors in a doped device and the methods by which donor orbital transitions have been measured and characterised here.

Chapter 3 is a non-experimental chapter containing the theory of Poisson point process statistics used to describe the distribution of nearest neighbour separations between donors in randomly doped samples. This is explored here to assess the potential of finding multi-species donor clusters occurring by chance in randomly doped samples. If this is possible, such samples may provide a useful, easy to fabricate test-bed sample for characterising gated spin interactions using orbital excitations such as in the system proposed in the SFG scheme. Although the analytical results for the distribution of neighbour separations in a system of randomly doped n-dimensional space is well reported in the literature, the result shown here for a inhomogeneous concentration profile along one of the three dimensions is not. The analytical solution found when the inhomogeneous concentration profile is Gaussian is also novel. The theory is then extended to describe the probability of finding clusters of two species that meet a more complex set of separation conditions pertaining to those useful in a SFG cluster. Improvement of this probability over the optimum for bulk doping in both two or three dimensions is observed for a system of two species each with doping concentrations that are Gaussian in depth.

Chapter 4 begins by deriving the optical Bloch equations used to model the time dynamics of coherent orbital excitation of a two-level atom including leakage into the continuum out of the excited state. This model is then used to extract dynamics information from experimental Ramsey spectroscopy results of a dilute, bulk doped Si:P sample. These measurements were made using pulsed FEL radiation and contactless PTIS as the detection mechanism. Dynamics measurements for particular transitions were taken over a large magnetic field range. The consequential detuning of these transition due to the magnetic field is useful to avoid potential water vapour IR absorption resonances and also phonon resonances present as a bulk property of the lattice. The coherence times of this system under such high field conditions were previously unreported. Potential pitfalls that arise when using PTIS signal as an indirect measure of the excited state probability are identified along with critical considerations that must be made of the laser pulse intensity.

Chapter 5 reports electrically contacted ionisation spectroscopy of a silicon-on-insulator (SOI) device implanted with bismuth to assess the viability of on-chip characterisation of donor orbital states demonstrating the detection of orbital transition from the fewest implanted donors in a device. The activation of the annealed bismuth implant is measured using spreading resistance profiling. Electrical measurements of the device in the dark revealed that the high electric fields accessible under low voltage bias can cause impact ionisation of the donor ground state. It is shown that this could provide a viable alternative mechanism for preferential ionisation of the excited state as opposed to use of a phonon in PTIS which require the sample to be at a high enough temperature. Opening the possibility of orbital state characterisation at much lower temperatures that one would typically require for donor electron spin polarisation.

Finally, chapter 6 provides a summary of the conclusions found in chapters 3 to 5 and suggests continuations and improvements for future work.

Chapter 2

Experimental techniques

Throughout chapters 4 and 5, a number of techniques have been used for the fabrication and characterisation of doped silicon devices. In this chapter these experimental methods are described.

The external company, Solecon Laboratories provided spreading resistance analysis (SRA) measurements of the implanted and annealed silicon-on-insulator (SOI) material used in chapter 5. Photoconductive measurements made using a THz free electron laser (FEL) were carried out at the FELIX and HFML Laboratory based at Radboud University in the Netherlands with the assistance of Dr Nils Dessmann, Dr Vikroria Eless and Dr Hans Engelkamp.

2.1 Spreading resistance analysis

After implanting a sample with dopants it is important to measure the fraction of those that are successfully incorporated as substitutional defects and to identify the amount of diffusion that has taken place. SRA (also called spreading resistance profiling) is a technique used to determine the active concentration of dopants in semiconductors. This is in contrast to techniques like secondry ion mass spectroscopy (SIMS) in which the concentration of elements sputtered from the sample and detected includes all dopants regardless of whether they were sputtered from electrically active lattice sites.

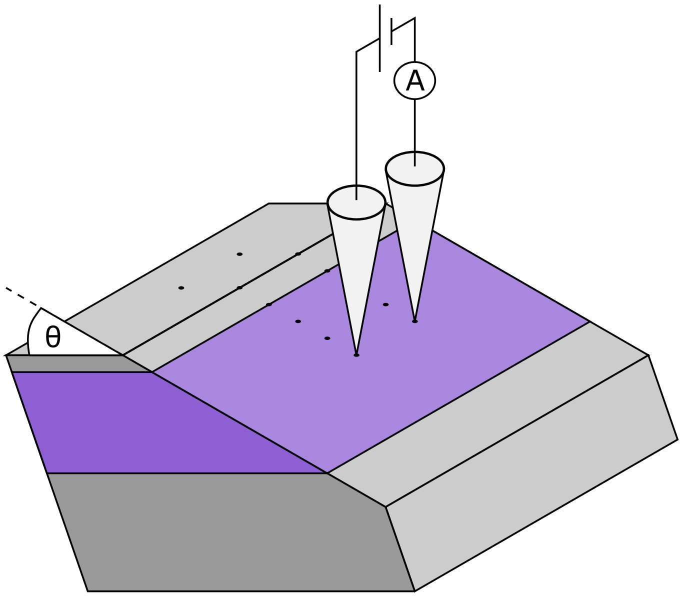

Figure 2.1: Illustration of spreading resistance analysis technique. A bevel angle, Θ is polished into the wafer and two probe resistivity measurements are taken along the bevelled surface and converted to an active carrier concentration.

Like SIMS, SRA is however a destructive method, to measure concentration as a function of depth a bevel is polished into the surface of a piece of wafer with a well known angle. Along this bevelled surface, electrical probes are placed a small fixed distance apart. The high mechanical pressure of probes on the surface cause a phase change in the silicon that results in an ohmic contact between the probe tips and the silicon. As depicted in fig. 2.1, two terminal resistivity measurements are taken along the bevelled surface and are converted to a majority carrier concentration, N using:

$$\rho = \frac{1}{Ne\mu} \tag{2.1}$$

where e is the electron charge and μ the electron mobility. Prior knowledge of the mobility may be avoided by comparing the measured resistivity of an unknown sample to the measured resistivities of calibration standards with known n and p-type carrier concentration measured by other means e.g. Hall effect.

These resistance measurements are taken at room temperature whereby shallow extrinsic donors and acceptors are assumed to be completely thermally ionised. The density of electrons in the conduction band is therefore equivalent to the density of extrinsic donors since, in this thesis the density of extrinsic donors in any sample far outweighs the density of background acceptors one need not worry about compensation effects masking the true density of donors. The SRA results presented in this thesis used an ultra-shallow bevel (0.002 74 rad angle and a 3 μm step size to achieve the 10 nm depth resolution shown.

2.2 Coherent THz excitation using a free electron laser

The Lyman series for hydrogenic donor centres in silicon exist in the THz frequency range and intense sources of coherent light in this part of the spectrum are uncommon. [43] High intensity, coherent light is required to have full control over the orbital state of a neutral donor in silicon. A FEL is one of few monochromatic, coherent emitters of high intensity light in the 1 THz to 20 THz range (4 meV to 80 meV or 33 cm^{-1} to 670 cm^{-1}). Other sources include quantum cascade lasers [44], exotic non-linear optics sources [45] and even stimulated emission from donors in silicon themselves [46]. These alternatives are either not as powerful or as widely tunable. The specific frequency range required spans the donor with the largest binding energy and that with the smallest Lyman series transition. Bismuth is the most tightly bound donor with a binding energy close to 17 THz. The smallest orbital transition from a donor ground state is the $1s(A_1) \rightarrow 2p_0$ for Si:Sb at 7.5 THz. In this work the FEL facility free electron laser for infrared experiments (FELIX) is used which is capable of provide pulsed, coherent THz pulses over this entire frequency range and more to accommodate the detuning of transitions in chapters 4 and 5.

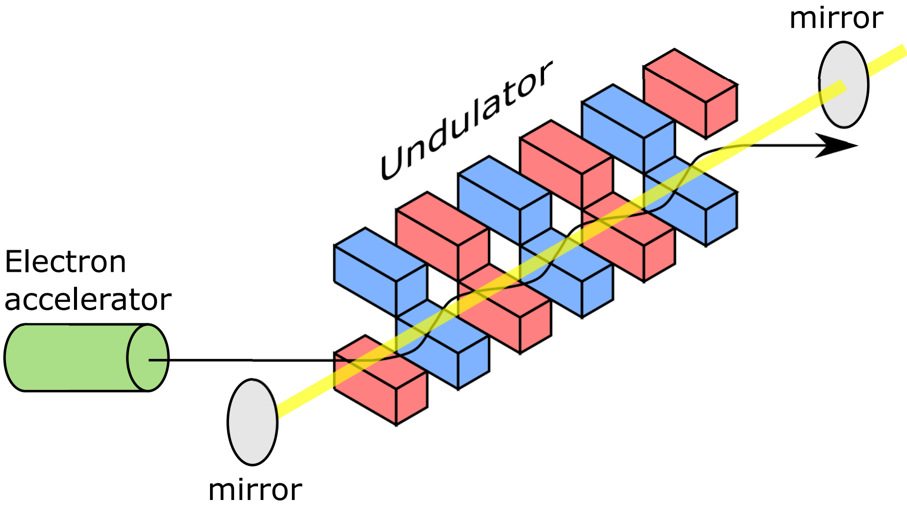

Figure 2.2: Illustration depicting FEL operating principle. Electrons travelling close to the speed of light are guided into an array of alternating magnetic fields to produce light. Light produced in phase with light in the cavity is amplified and guided to the user station at the facility.

FELs are sources of laser light whereby electrons are not bound to atoms as they are in the more ubiquitous atomic, molecular and solid state lasers. Instead, a beam of electrons is accelerated to relativistic speeds and directed into a periodic series of magnets with alternating pole arrangement called an undulator. The poles of the magnets in the undulator are arranged perpendicular to the electron beam direction causing the electrons to be deflected in a sinusoidal path while moving through it. This acceleration of charge generates synchrotron radiation at the wavelength dictated by the spacing of the magnets. This radiation is significantly up-shifted due to the Doppler effect and due to a length contraction of the undulator into the electron rest frame. The relativistic speed of the electron beam means that a 65 mm undulator period results in emitted infra-red (IR) light. The emitted radiation has an electric field component parallel to the deflection direction of the electrons in the undulator giving rise to the so called 'pondermotive force'. This allows energy to be exchanged between the electrons and radiation field which amplifies the intensity of the radiation and causes a modulation in the longitudinal velocity of electrons causing them to bunch together. As the electrons bunch together more the radiation that is emitted becomes coherent and there is an exponential growth in the radiation power. The resulting pulses of light emitted from the undulator mimics the microbunched nature of the electrons within the cavity. At the FELIX facility, light is directed from the source to the user station along with a trigger signal to synchronise measurements to the low duty-cycle macropulse waveform containing this bust of light pulses.

A FELIX macropulse comprises 10 ps long micropulses of light at a rate of 25 MHz lasting 10 μs. Macropulses arrive at a rate of 10 Hz. This low duty cycle of 1×10^{-4} % makes lock-in methods for photo-detection unfeasible so instead, a boxcar averaging is done of the detected signal immediately prior to the arrival of a macropulse which is subtracted from that during a macropulse. In this work both 'one pulse' and 'two-pulse' measurements were carried out. For a one pulse measurement, FELIX macropulses are simply guided and focussed from the beam port and onto the sample with mirrors and focused onto the sample inside a cryostat with a parabolic mirror. For the two pulse, Ramsey spectroscopy study, each individual micropulse needed to be separated into two exact phase copies. One copy was delayed in time requiring the use of delay stage optics.

2.2.1 Ramsey spectroscopy setup

In the two-pulse, Ramsey study presented here, a sample of high resistivity bulk doped Si(P) was mounted into a sample holder sandwiched between two copper plates with 2 mm holes such that THz light could pass through the stack. The stack was held in place mechanically with a wad of PTFE tape gently wedged in place between the top capacitor plate and the brass sample tray holder as depicted in fig. 2.3. A capacitive readout of the sample conductivity is advantageous for a large, uniformly doped sample as one need not contend with the difficulties of fabricating ohmic contacts. The sample holder is inserted into the cryostat insert and enclosed in an evacuated jacket back filled with a low pressure of helium gas. This is submerged into the liquid helium bath cryostat in the bore of a 33 T Bitter magnet. The helium gas in the jacket acts to exchange heat from the sample to the liquid helium bath surrounding the jacket.

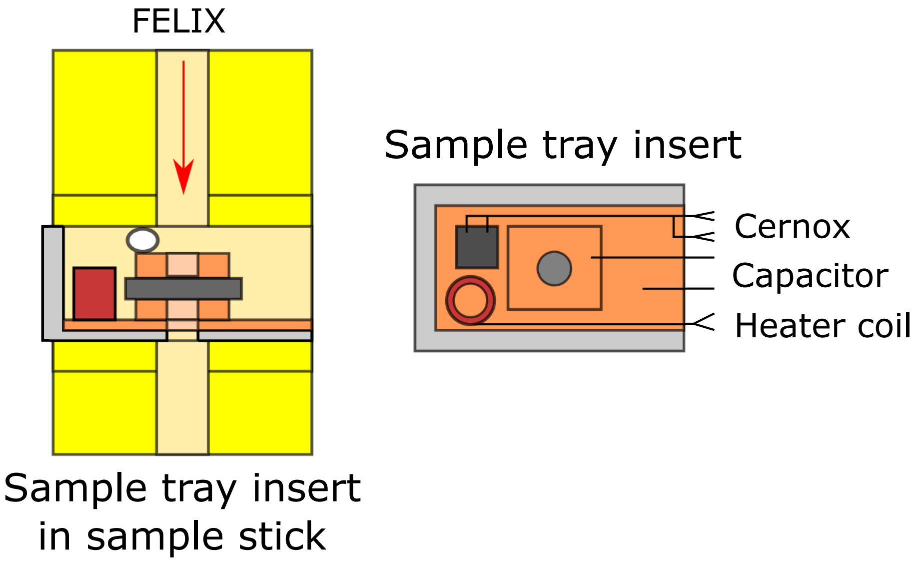

Figure 2.3: Sample geometry inside the high field magnet laboratory (HFML) bitter magnet cryostat. The sample-capacitor stack is held in a plastic tray to electrically insulate it from the stick. Heater and temperature sensor are mounted to the bottom capacitor plate for good thermal contact with the sample. The sample tray insert is placed in a universal brass insert that fits the cryostat stick.

A Cernox thin film temperature sensor and heater were placed next to the sample on the copper tray giving full control of the sample temperature down to 4.2 K. This was achieved by using a Lakesure temperature controller capable of calibrated four terminal resistivity measurement of the temperature sensor alongside supplying variable power to the heater allowing for dynamic, closed loop temperature control. The leads electrically connected to the copper capacitor plates were shielded throughout the length of the sample stick as well as outside of it in order to minimise noise. One capacitor plate was connected to an arbitrary waveform generator (AWG) to provide a voltage bias across the plates. The other capacitor terminal, to an SR570 transimpedance amplifier for current to voltage conversion to be logged by a NI PXI oscilloscope.

The optical setup consisted of an optical breakout board attached to the scaffold surrounding the top of the Bitter magnet. The FELIX beam line directed the beam down coaxial with the top of the cryostat. The convergent beam exiting the beam line needed to be collimated (usually the beam is focussed to the bottom of the sample stick without including the length of open air optics) and reflected onto the breadboard where pulses were delayed by a Michaelson interferometer as shown in fig. 2.4 before being guided back down into the cryostat.

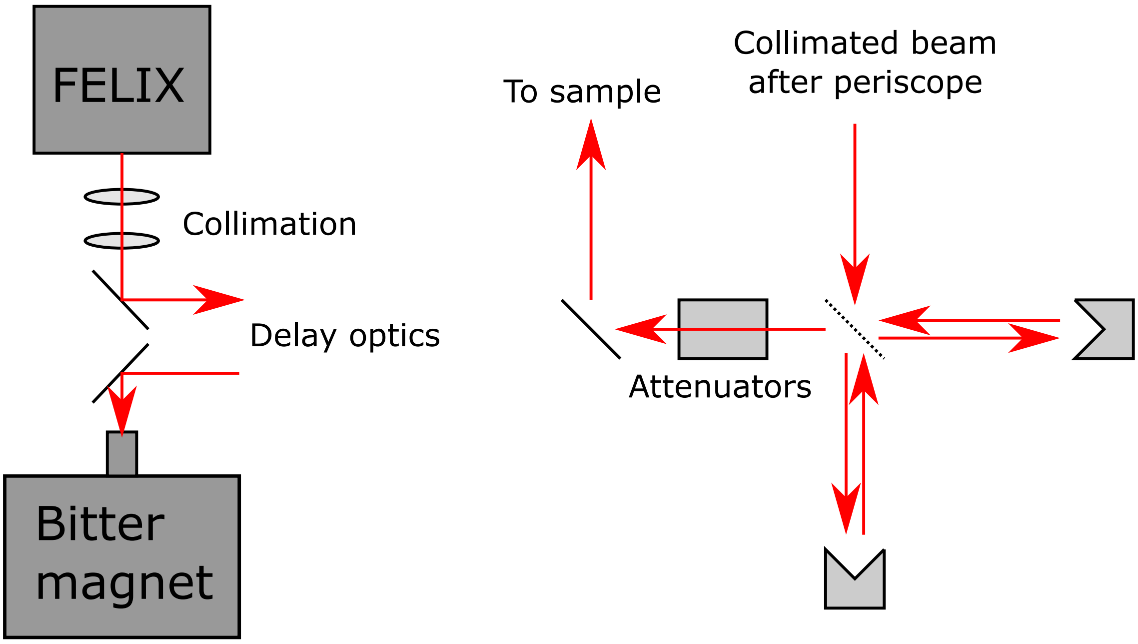

Figure 2.4: Optical path in FELIX/HFML Ramsey setup. FEL radiation is collimated and reflected with cage optics attached to the FELIX beam port. The pulse train passes through a Michaelson interferometer acting as a delay stage and attenuated by neutral density filters before being directed into the magnet cryostat insert where the sample is held.

The Michaelson interferometer divided incoming micropulses into two copies with the same carrier envelope phase i.e. the lights electric field is not simply amplitude modulated. The delay between the pulse copies was controlled by the motorised mount of one of the interferometer arms which, with a 200 mm throw, was positioned to be able to delay one pulse up to ±650 ps relative to the other. The intensity of both pulses were coarsely adjustable with the use of fixed value attenuators.

A purely DC voltage bias resulted in a circuit that was not sensitive to changes in the population of the conduction band. This problem was overcome by biasing such that the DC voltage across the capacitor plates switched polarity a short

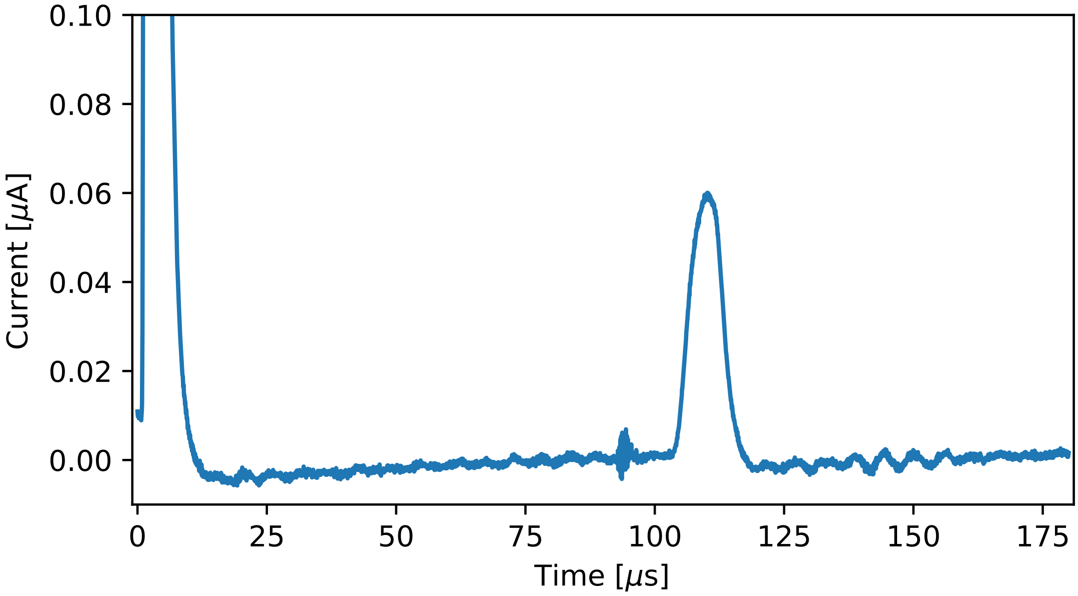

Figure 2.5: Contactless photo-thermal ionisation spectroscopy (PTIS) response in time. At $t = 0$ the polarity of the applied bias to the capacitor plates was switched from $-0.5\,\mathrm{V}$ to $0.5\,\mathrm{V}$ resulting in a transient current as the capacitor is charged. $100\,\mu$s after switching the bias polarity the FELIX macropulse arrives at the sample generating free carriers resulting in $60\,\mathrm{nA}$ of photocurrent. This particular macropulse was on resonant with the $1s(A_1) \rightarrow 2p_{\pm}$ transition at zero magnetic field using the maximum available attenuation ($38\,\mathrm{dB}$) and with one of the interferometer arms blocked (single pulse). The noise burst observed at $90\,\mu$s correlates with the trigger received at the user station used to synchronise data acquisition with the arrival of macropulses. Individual macropulses are not resolved due to the circuit bandwidth.

time, $100\,\mu$s, prior to the arrival of each macropulse resulting in an immediate transient current followed by the photocurrent generated when light arrives as shown in fig. 2.5. The polarity is then switched back at $t = 1\,$ms. This scheme allows any accumulated charge traps in the sample to be neutralised immediately before illumination.

2.2.2 Single pulse FEL spectroscopy setup

The setup used in chapter 5 for FEL spectroscopy of a SOI device implanted with bismuth donors is very similar in principle as that used for Ramsey spectroscopy but without the delay stage optics and not having the sample in a magnetic field. The sample is mounted in this instance to a PCB attached to a cold finger cryostat. Instead of being surrounded by helium exchange gas, the sample is cooled by being in indirect thermal contact with the copper end of the insert which has a constant flow of liquid helium through it.

For this device, aluminium leads were wire bonded to deposited aluminium pads on the sample surface. Conductivity in the region of the implanted bismuth centres was measured resistively. In this case a purely DC voltage was applied to two adjacent terminals of the 4-terminal Van der Pauw (VdP) device structure. The current was amplified outside the cryostat at room temperature by a SR570 transimpedance amplifier and monitored with an NI PXI oscilloscope. Also monitored in this setup was the potential at the two remaining leads of the device (at the corners along the opposite edge). The potential drop sensed between these leads is due only to the resistance of the sample material between them (with a geometrical factor due to the VdP structure) and does not include contact resistances since no current flows through them. Upon scanning the FELIX wavelength both the current through the device and sensed voltage were logged by the oscilloscope.

2.3 Electrically detected photon-assisted ionisation spectroscopy

In both donor orbital spectroscopy measurements presented in this thesis, electrical readout of the transition was done in favour of a transmissive detection. This was due to low density of donors in chapter 4 and the low absolute number of donors in chapter 5. To electrically detect whether a donor is in its excited state or not, an electrical property of the material must change in relation to this. It may not be immediately clear how this is possible since both the ground and excited states are both bound so the electron is not available to conduct. However, due to the difference in binding energy of the ground and excited states possible detection mechanisms could involve imparting energy into the donor that is enough to ionise it when in the less tightly bound excited state while leaving it bound when in the ground states. There are some options for the source of this additional energy and these are illustrated in fig. 2.6

Figure 2.6 presents three mechanisms by which a resonantly excited donor is ionised and populates the conduction band. After initial optical excitation (1), an acoustic phonon can scatter with the electron and thermally ionise it. The presence of phonons in the appropriate energy range to ionise the excited state but not the ground state is clearly then temperature dependant and this technique for detection is therefore called PTIS. The mechanism labelled (2) appears similar to that of (1) however instead of scattering with a phonon, this mechanism relies on the presence of high velocity, free electrons in the conduction band. To promote the bound electron into the conduction band and leave the donor site ionised the incident electron must have an excess kinetic energy greater than the binding energy of bound electron. This process is therefore called impact ionisation (II). A third mechanism is also possible, in the excited atom can absorb another photon to be directly ionised by

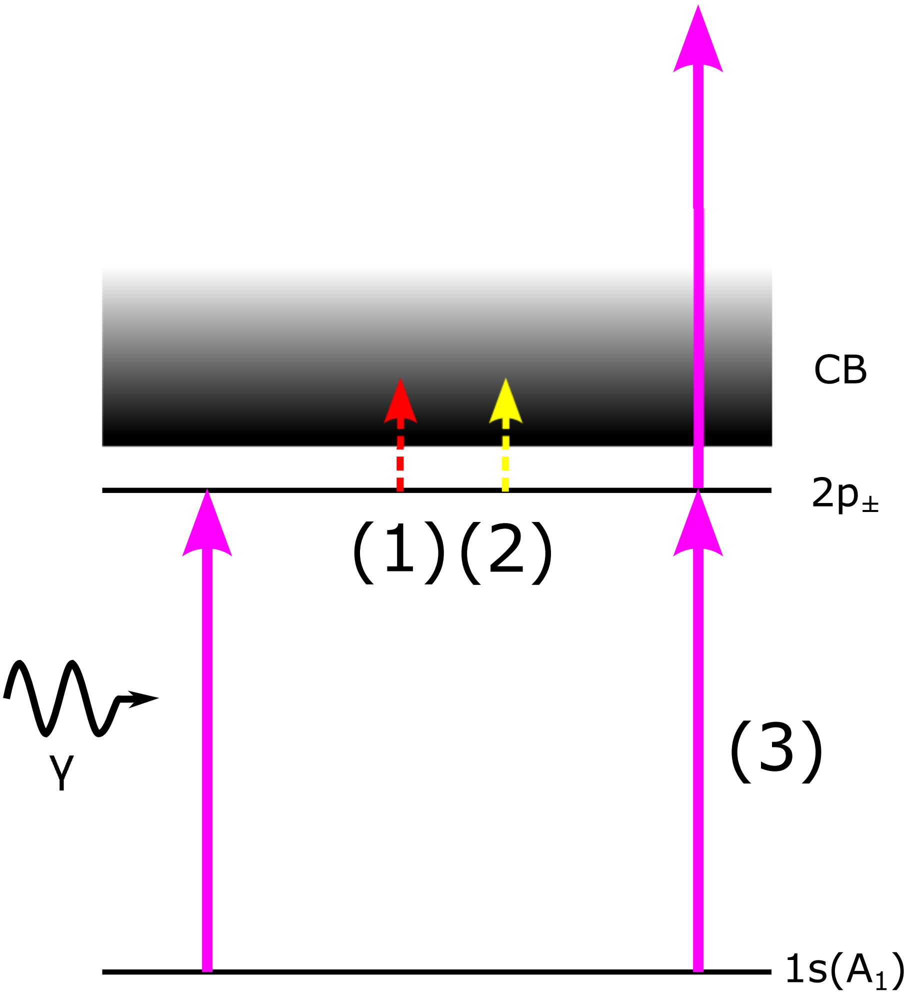

Figure 2.6: Mechanisms that populate the conduction band mediated by a resonant orbital transition. (1) Thermal ionisation of the excited state, (2) Impact ionisation of the excited state, and (3) multiphoton absorption.

a multiphoton absorption. Such mechanisms have been demonstrated to have an effect for donors in silicon [47]. No inclusion of this third mechanism is attempted in this work as much lower FEL intensities were use here where the cross sections for multiphoton absorption is low.

The cross-section for the two step, photo-thermal ionisation process for a particular transition can be expressed as

$$\sigma_I(\omega_n) = \sigma(\omega_n)I(n) \tag{2.2}$$

where $\sigma_I(\omega_n)$ is the cross-section for absorption for the transition between the ground and n-th excited state with resonant frequency, ω_n. $I(n)$ is then the probability that the excited state is thermally ionised. $I(n)$ has the form,

$$I(n) \propto exp(-\frac{E_n}{k_B T}) \tag{2.3}$$

where E_n is the binding energy of the excited state. [48] It is clear that this probability increases exponentially with temperature and decreasing binding energy.

In an electrically contacted device such as that presented in chapter 5. A dilute region of doped silicon can be defined between metallic leads using conventional UV-photolithography processing. In this work, the contacted sample in chapter 5 uses a SOI substrate, reactive ion etching (RIE) etching and broad area ion implantation to define a small region of optically active bismuth donors. High density n-type doping away from this region defines metallic leads that meet the dilutely doped channel to form n^+nn^+ structures. At low temperatures the donors in the dilutely doped channel freeze out making the device insulating.

The heavily doped nature of the leads means they remain metallic at temperatures where a dilute concentration would freeze out. This is because at such high densities the orbital states of the individual donors overlap forming a band of states. In the leads, the Fermi level, E_F lies within this band which could even be at an

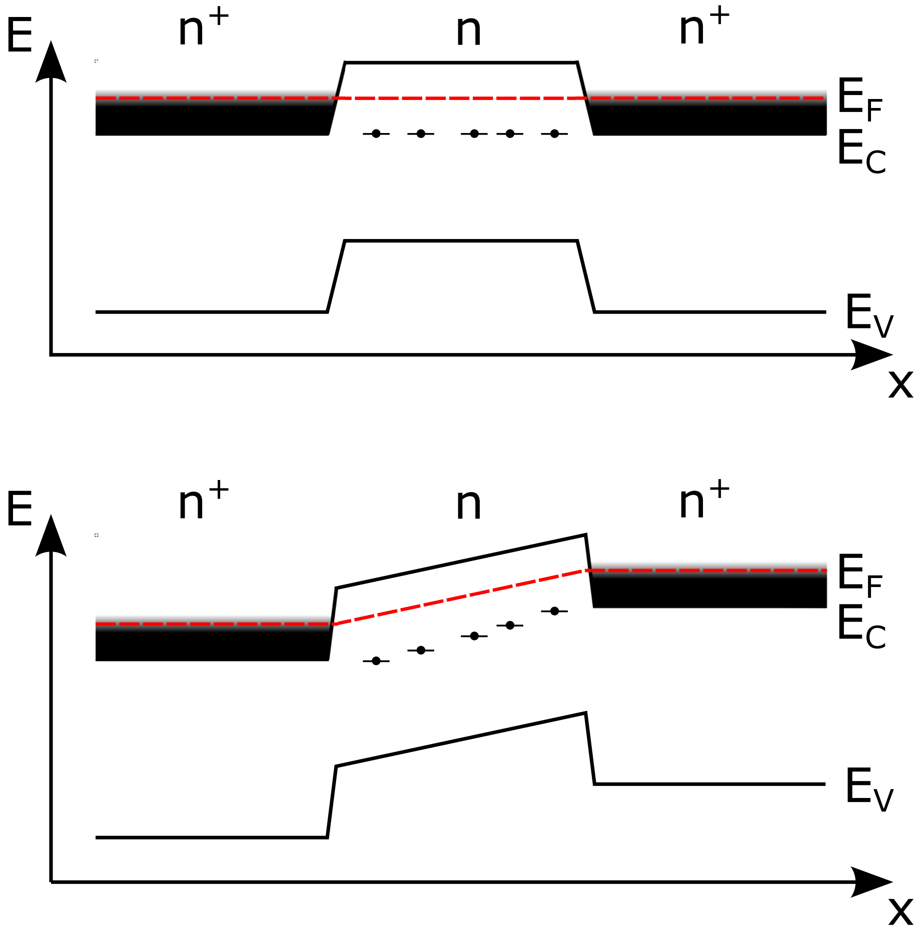

Figure 2.7: Band structure through n^+nn^+ resistor. At equilibrium the Fermi energy in the dilute region aligns with that of the leads forming a potential energy barrier into the channel. Under bias electrons may tunnel into the channel.

energy above the conduction band edge. In the dilutely doped region where the carriers remain frozen out E_F lies between the conduction band edge and the binding energy of the donors. At equilibrium, the Fermi level must be constant everywhere throughout the device else the device is not at equilibrium and charge will continue to move until a electrochemical potential minimum is achieved. This situation is depicted in the upper panel in fig. 2.7.

A voltage bias applied between the two n^+ regions will cause a current to flow through the device provided electrons are able to populate the conduction band in the dilutely doped channel. This condition is not necessarily met at low temperature. An electron, free to move within the impurity band at the heavily doped lead must overcome a barrier potential to pass into the conduction band in the frozen-out dilute region by thermionic emission analogous to a diode under reverse bias. This situation is depicted in the lower panel in fig. 2.7. If even this isn't possible due to the low temperature, an electron has a finite probability of tunnelling through the barrier into the channel region at high enough bias. At increasingly high bias the approximated triangular shape of the potential barrier becomes shorter and the probability of tunnelling increases.

Impact ionisation spectroscopy (IIS) however does not rely on thermal ionisation of the excited state and instead takes advantage of hot carriers in the conduction band to impact ionise the excited state donors with a higher probability than those in the ground state. Higher state electron orbitals have lower binding energy and a spatially larger orbital therefore a larger II cross-section given the energy distribution of conduction band electrons. At temperatures too low for electrons to thermionically pass the barrier potential at the lead they must tunnel through it. Following the analysis of Dierickx et al. [49], the electric field required to activate shallow level impact ionisation is again dependent on the binding energy, E_n of the bound electron state being ionised. The details of impact ionisation will be presented in further detail in chapter 5.

For large samples of bulk material it is unnecessary to fabricate ohmic electrical contacts to detect a change in current to determine a change in conductivity. In chapter 4, the sample was placed between two metal plates to form a parallel plate capacitor. The wafer was thick enough that the electric field across the plates was too small to cause impact ionisation so PTIS is considered the only ionisation mechanism present. A small, 2 mm diameter hole in the plates allows for optical access to the sample such that when free carriers are generated photo-thermally a transient current flowed in the electric field generated by the charged capacitor.

Chapter 3

Multi-species donor cluster configuration statistics

Systems of multiple species of donor impurity atoms in semiconductors have been proposed to realise qubit gates in silicon [31]. In the system proposed in [31], donor spin qubits are entangled by exciting a spatially intermediary donor into a higher energy and therefore larger orbital state such that its wave function overlaps with those of the two qubits. Although methods exist to place atoms with high precision into semiconductor lattices, namely scanning tunnelling microscope (STM) hydrogen lithography and single ion implantation, these methods are direct write techniques and it is challenging to scale from fabricating single device to a wafers containing billions of devices.

In this chapter the feasibility of non-deterministic methods of dopant incorporation is explored. To begin with, the statistics relevant for finding the probabilities of dopant-dopant separations is outlined. This is then generalised to non-homogeneous systems of dopants, specifically those whose densities are described by Gaussian functions of depth which is a good approximation for the dopant distribution after broad area ion implantation. From there the nearest neighbour cluster definition is extended to allow for more complicated clusters necessary for optically gated qubit operations. The exact integral required to calculate the probability of finding such complex clusters is presented. Finally, the doping density profiles are optimised numerically to maximise this probability using a useful approximation/heuristic to accelerate the computation.

The optimised useful cluster probabilities found for multispecies Gaussian doping profiles are found to be higher then those for optimised homogeneous doping. Despite this, the probability of finding a useful cluster remains low and this result provides important impetus for the development of deterministic doping techniques such as single ion implantation (SII).

3.1 Nearest neighbours in a point process

If a distribution of events is non-homogeneous in space the density $n(\mathbf{x})$ and the expected number of events $\delta N = n(\mathbf{x})\delta\mathbf{x}$ in an infinitesimal volume $\delta\mathbf{x}$ varies with location, $\mathbf{x}$. If δN is so small that the probability of more than one event is negligible the probability of an event in $\delta\mathbf{x}$ is equal to δN. The probability that there are no events within a larger volume V may be found by dividing it up into elemental volumes. The expected number of events in V is then simply

$$N(V) = \sum_{\mathbf{x}_i \,\in\, V} \delta N_i = \int_{\mathbf{x} \,\in\, V} n(\mathbf{x})\,\mathrm{d}\mathbf{x}\,. \tag{3.1}$$

Assuming $n(\mathbf{x})$ is well-behaved, one may choose the size of the i^{th}element ($\delta\mathbf{x}_i$) so that the product $n(\mathbf{x}_i)\delta\mathbf{x}_i$ is a constant. The probability of an event within $\delta\mathbf{x}_i$ is then the same for every element, and it follows that the probability of m events enclosed in the larger volume V is given by the probability mass function for a Poisson distribution

$$P(m, N(V)) = \frac{[N(V)]^m \exp(-N(V))}{m!}. \tag{3.2}$$

Previously, clusters of impurities with homogeneous density have been discussed in terms of the distribution of neighbour-neighbour distance [50]. In order to put this discussion into this context the non-homogeneous case is presented, which follows immediately from equation eq. (3.2). The notation, $p_{\mathbf{x}\to A_i}(r)\delta r$ is the probability that a point in 3D Euclidean space, $\mathbf{x} = (x, y, z)$ has its i^{th}nearest event of species A at a radial distance between $r \to r + \delta r$ from it. $p_{\mathbf{x}\to A_i}(r)$ will be referred to as the nearest neighbour probability density function (NNPDF). In previous literature the NNPDF is the precursor to the "void nearest neighbour distribution function" [51] which is simply the cumulative distribution of the NNPDF defined here. The term "void" is used since there is no event specified at the point $\mathbf{x}$ whose neighbour is being found.

To calculate the NNPDF, consider the sphere $V_{\text{sphere}}(r; \mathbf{x})$ centred on $\mathbf{x}$ of radius r, and the infinitesimal shell of thickness δr around it. The probability of finding the first nearest A event within the shell is then

$$p_{\mathbf{x}\to A_1}(r)\delta r = P(0, N_A(V_{\text{sphere}}(r; \mathbf{x}))) \cdot \delta N_A \tag{3.3}$$

and may be understood as the product of the independent probabilities of having no A events within the sphere and one within the shell. The probability of an event occurring in the shell is $\delta N_A = \delta r \frac{d}{dr} N_A(V_{\text{sphere}}(r; \mathbf{x}))$. Generalising for the i^{th}nearest neighbour gives

$$p_{\mathbf{x}\to A_i}(r) = P(i-1, N_A(V_{\text{sphere}}(r; \mathbf{x}))) \cdot \frac{\mathrm{d}}{\mathrm{d}r} N_A(V_{\text{sphere}}(r; \mathbf{x})) \tag{3.4}$$

The distribution around a void can be made specific to the distribution of neighbours around an event by considering the density of events in the infinitesimal volume $\delta\mathbf{x}$ at $\mathbf{x}$. From here on only spherical finite volumes will be discussed unless specified otherwise. It therefore makes sense to simplify the notation, $N(V_{\text{sphere}}(r; \mathbf{x})) \to N(r, \mathbf{x})$.

3.1.1 Homogeneous point process

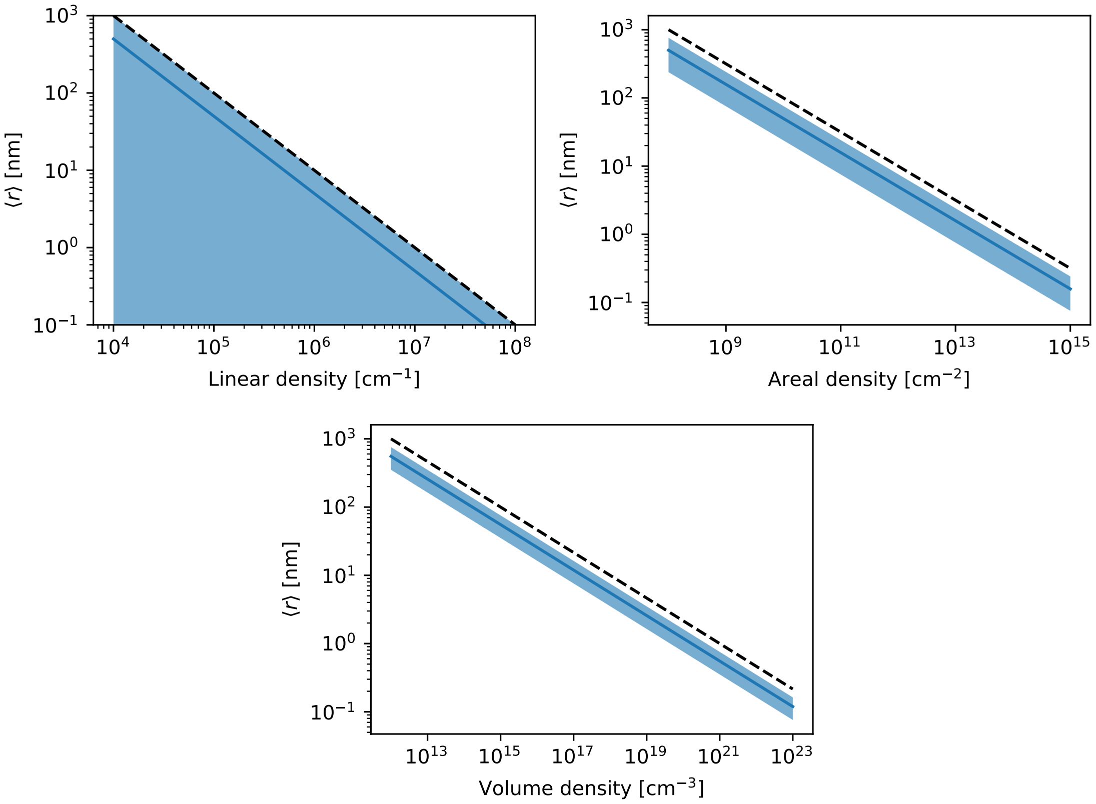

Figure 3.1: Solid blue lines show the expected nearest neighbour separation for homogeneously random systems of events in 1D, 2D and 3D as functions of their respective density units. The standard deviation in the nearest neighbour separation is also outlined by the shaded region. The black, dashed line shows the separation between events in a perfectly uniform distribution $(1/\sqrt[m]{n})$is also shown as a dashed line and always over estimates the nearest neighbour distance between randomly placed events.

The homogeneous results in the common bulk doped or delta-doped layers in semiconductors can be recovered from this generalisation. For example, in uniformly doped 3D $n_A(\mathbf{x}) \rightarrow n_A^{3D}$ and so $N_A(r) \rightarrow \frac{4}{3}\pi r^3 n_A^{3D}$, and $\frac{\mathrm{d}N_A(r)}{\mathrm{d}r} \rightarrow 4\pi r^2 n_A^{3D}$. Hence all terms in equations eq. (3.2) and eq. (3.4) are independent of $\mathbf{x}$ and the well established [52] homogeneous neighbour-neighbour distributions are obtained.

$$p^{\mathrm{1D}}_{\mathbf{x}\to A_1}(r) = 2n_A^{\mathrm{1D}} \exp\left(-2rn_A^{\mathrm{1D}}\right) \tag{3.5a}$$

$$p^{\mathrm{2D}}_{\mathbf{x}\to A_1}(r) = 2\pi r n_A^{\mathrm{2D}} \exp\left(-\pi r^2 n_A^{\mathrm{2D}}\right) \tag{3.5b}$$

$$p^{\mathrm{3D}}_{\mathbf{x}\to A_1}(r) = 4\pi r^2 n_A^{\mathrm{3D}} \exp\left(-\frac{4}{3}\pi r^3 n_A^{\mathrm{3D}}\right) \tag{3.5c}$$

The first two moments (expected radius and standard deviation) of the probability distributions stated in eq. (3.5) are analytically solvable and are plotted in fig. 3.1 as functions of event density. The units used are typical for densities of impurities and their separation in semiconductors. It is also useful to point out that the approximation $\langle r\rangle \approx n_A^{-1/d}$, where d is the dimensionality of the event space, is always an overestimate as also shown in fig. 3.1 as a dashed line. Random displacement of events on a square grid decreases the mean nearest neighbour separation.

3.1.2 Non-homogeneous variation in 1D

The particular class of event distributions of interest are those whose density is homogeneous in two dimensions but varies in depth only e.g. broad area ion implantation (BAII). The expected number of events per unit area in the infinitesimal slice through $z \to z + \delta z$ is $n_A(z)\delta z$ and the total areal density (equivalent to implant dose in BAII) is $n_A^{\mathrm{2D}} = \int_{-\infty}^{\infty} n_A(x)\,\mathrm{d}z$. The expected number of events in a sphere $V_{\mathrm{sphere}}(r; z)$ of radius r now has a dependence only on the depth at which it is centred $\mathbf{x} = (0, 0, z)$ such that

$$N(r,z) = \int\limits_{z' \,\in\, V_{\mathrm{sphere}}(r;z)} n_A(z')\pi\left[r^2 - (z'-z)^2\right]\mathrm{d}z' \tag{3.6}$$

and,

$$\frac{\mathrm{d}N(r,z)}{\mathrm{d}r} = 2\pi r \int\limits_{z' \in V_{\text{sphere}}(r;z)} n_A(z')\,\mathrm{d}z' \tag{3.7}$$

3.1.3 Gaussian variation in 1D

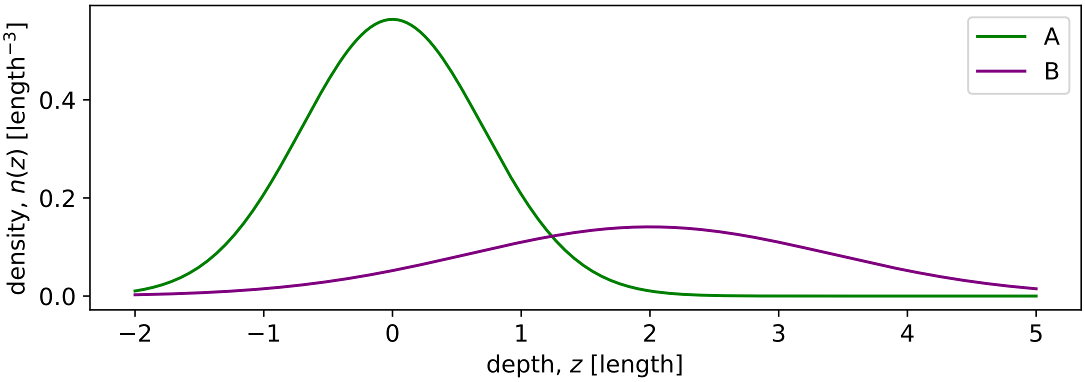

Figure 3.2: Example of a system of two event species whose densities are distributed as Gaussian functions of depth separated by two units of length. Species A has unit integrated density and unit width while species B has an integrated density half that of A and is spread out in depth with a width twice that of A.

A reasonable approximation for the distribution of dopants introduced by typical mono-energetic implants is one whose density varies as a Gaussian function of depth i.e. $n_A(z) = \frac{n_A^{2\text{D}}}{d_A\sqrt{\pi}} \exp\left(-\frac{(z-\mu_A)^2}{d_A^2}\right)$ where, $d_A/\sqrt{2}$ is the standard deviation of the density profile centred at μ_A. d_A will be referred to as the width of the Gaussian event distribution. When the density of events is described by a Gaussian, both $N_A(r,z)$ and its derivative in r have analytical solutions and therefore so does the resulting NNPDF.

$$N_A(r,z) = \frac{n_A^{2\text{D}}\sqrt{\pi}}{4}\left(-2d_A^2 E + S\sqrt{\pi}\left(d_A^2 - 2r^2 + 2(z-\mu_A)^2\right)\right) \tag{3.8a}$$

$$\frac{\mathrm{d}N_A(r,z)}{\mathrm{d}r} = n_A^{2\text{D}}\pi S r \tag{3.8b}$$

$$p_{z\to A_i}(r) = \frac{N_A(r,z)^i \exp(N_A(r,z))}{i!}\frac{\mathrm{d}N_A}{\mathrm{d}r} \tag{3.8c}$$

where,

$$S = \operatorname{erf}(\zeta_+) + \operatorname{erf}(\zeta_-) \tag{3.9a}$$

$$E = \zeta_+ e^{-\zeta_-} + \zeta_- e^{-\zeta_+} \tag{3.9b}$$

$$\zeta_\pm = \frac{r \pm (z - \mu_A)}{d_A} \tag{3.9c}$$

are defined for convenience.

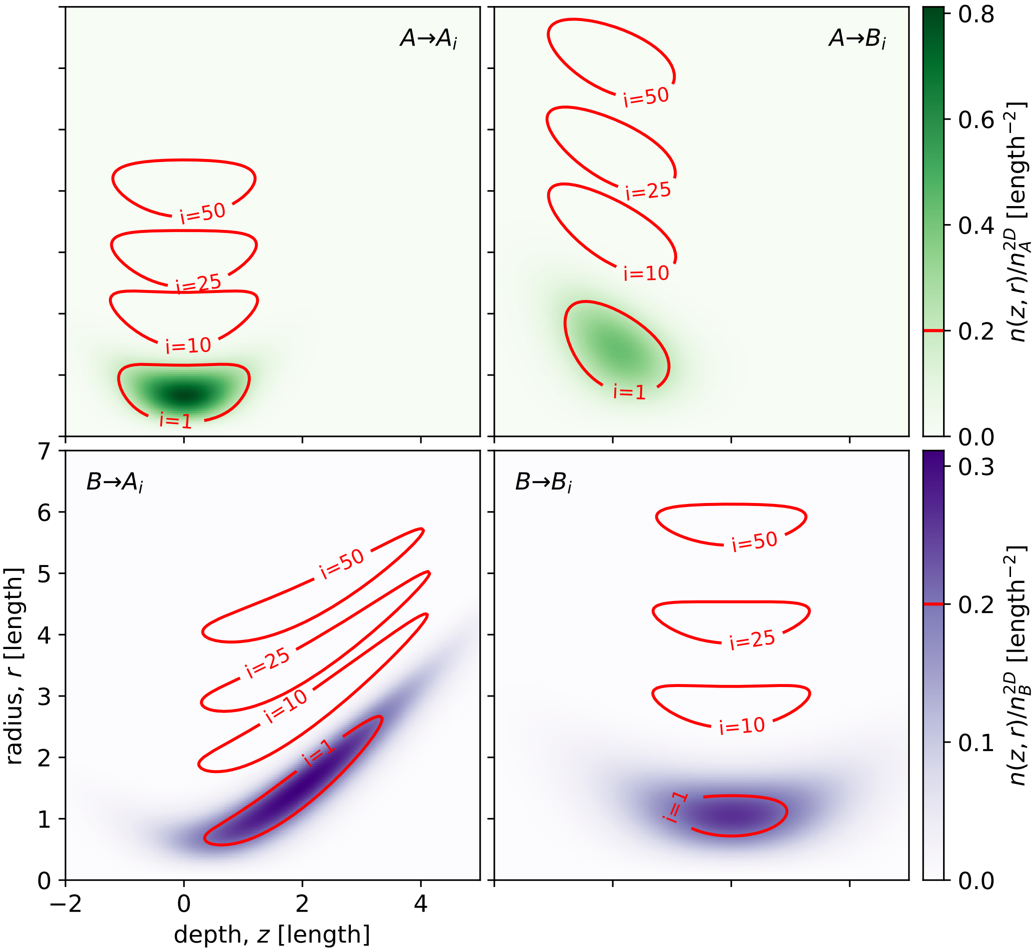

Figure 3.3: Normalised i^{th}nearest neighbour density surface (NNDS) for the system of two event species as shown in fig. 3.2. The heat maps show the full distribution for the particular case when $i = 1$. The red contours are drawn at a value of $n_{X\to Y_i}(z, r)/n_X^{2\text{D}} = 0.2$ to show how distribution changes for larger i^{th}neighbours.

Consider the system of two species of events depicted in fig. 3.2 the mutual separation between all combinations of events of different species using eq. (3.8c) can be investigated. The density of X events at a particular depth that have an i^{th}nearest Y neighbour at a particular separation distance follows immediately as

$$n_{X\to Y_i}(r,z)\delta r\delta z = p_{z\to Y_i}(r)\delta r \times n_X(z)\delta z. \tag{3.10}$$

Both sides of eq. (3.10) have units of density in one fewer spatial dimensions than $n_X(z)$. In this case $n_X(z)$ is a volume density and therefore $n_{X\to Y_i}(r,z)\delta r\delta z$ has units of areal density. $n_{X\to Y_i}(r,z)$ will be referred to as the NNDS and is normalised easily since

$$\int\limits_{z=-\infty}^{\infty}\int\limits_{r=0}^{\infty} p_{z\to Y_i}(r) n_X(z)\,\mathrm{d}r\,\mathrm{d}z = \int\limits_{z\,=\,-\infty}^{\infty} n_X(z)\,\mathrm{d}z = n_X^{\text{2D}}. \tag{3.11}$$

This allows for discussion of the fractional number of events of an entire distribution at a particular depth range with an i^{th}nearest neighbour existing within a particular radial range. This fractional quantity will be a useful figure of merit when it comes to optimising density distributions in favour of specific configurations.

The expected nearest neighbour distance may be calculated and plotted for Gaussian non-homogeneous point process in much the same way as done for homogeneous processes in fig. 3.1. The difference in this case is that $\langle r\rangle$ is now a function of two variables as plotted in fig. 3.4 for typical values encountered in BAII. The doping configuration whose NNDS is shown in fig. 3.4 has a Gaussian profile whose width (10 nm) is larger than its expected nearest neighbour separation given the profiles integrated density, $10^{14}\,\text{cm}^{-2}$ (1.7 nm). This condition leads to counterintuitive observations e.g. the expected nearest neighbour separation for an impurity at $z = 20\,\text{nm}$ is much smaller than 20 nm (the distance from that event to the depth of peak impurity concentration).

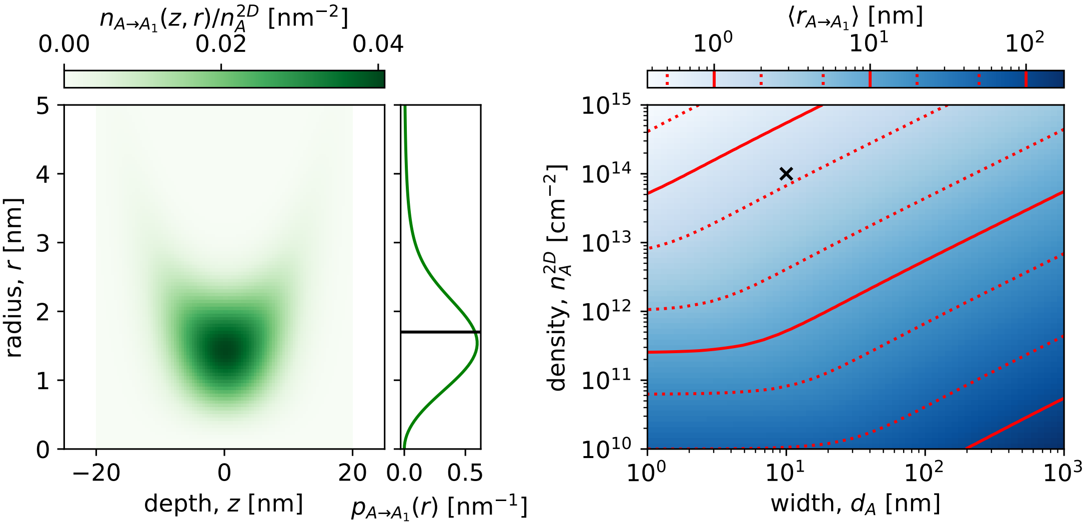

Figure 3.4: The expected nearest (same-species) neighbour of an impurity from a typical 1D Gaussian non-homogeneous distribution with $n_A^{\mathrm{2D}} = 10^{14}\,\mathrm{cm}^{-2}$ and $d_A = 10\,\mathrm{nm}$ can be found from its NNDS (left). By integrating this function over depth a NNPDF is found whose first moment is $\langle r_{A\to A_1}\rangle$. The expected nearest neighbour distance is a function of n_A^{2D} and d_A (right). This panel demonstrates that the nearest neighbour characteristics of Gaussian non-homogeneous layers transitions to that for 2D homogeneously random layers when $d_A \leq \langle r_{A\to A_1}\rangle$ for a particular n_A^{2D}. The expected nearest neighbour separation for the NNDS in the left panel is marked by a cross.

3.2 Density of specific cluster configurations

So far only clusters of events in their most basic sense have been investigated i.e. a cluster that is defined by an event about which $i-1$ events exist in close proximity up until an i^{th}event at a particular radius. In this section the same thought process will be used to quantify the number of instances of more involved definitions of a 'viable cluster'. The involved cluster definition explored here is one whose viability relies on higher order nearest neighbours i.e. the nearest neighbours of a central events nearest neighbour. It is useful to continue with the assertion that a viable cluster is always centred around an event that is part of that cluster.

The total number of viable clusters, N_{viable} is found in a similar way to eq. (3.1). The expected number of viable clusters in the elemental volume $\delta\mathbf{x}$ about $\mathbf{x}$ is the expected number of 'central events' in the elemental volume multiplied by the probability that an event in that elemental volume is part of a viable cluster. Letting the central event be of species A, the total number of viable clusters is then

$$N_{\text{viable}} = \int\limits_{\mathbf{x}} P_{A\mathbf{x}}\{\text{viable}\} n_A(\mathbf{x})\,\mathrm{d}\mathbf{x}\,. \tag{3.12}$$

$P_{A\mathbf{x}}\{\text{viable}\}$ has been used as a shorthand here for the conditional probability that a viable cluster exists about $\mathbf{x}$ given that an A event exists at point $\mathbf{x}$. When a viable cluster consists of events of multiple species it should not matter which species is used as the central event about which the cluster is described. In the case of A and B events in 3D with 1D non-homogeneous density variation along z and a viable cluster contains the same number of A's as B's, the number of useful clusters (per unit area) is

$$N^{\text{2D}}_{\text{viable}} = \int\limits_{z} P_{Az}\{\text{viable}\} n_A(z)\,\mathrm{d}z = \int\limits_{z} P_{Bz}\{\text{viable}\} n_B(z)\,\mathrm{d}z\,. \tag{3.13}$$

3.2.1 A qubit gate cluster probability

In the interest of multi-species clusters that have specifications on the separations, consider a pair of substitutional donor qubits that carry quantum information in their electron spin. The gate operation is performed by controlling the entanglement between the two impurity electrons. By performing an orbital excitation of one of the species with a resonant π-pulse the radial extent of the electrons wave function is greater. This change in size of a control qubit, A increases the probability of entanglement with a nearby target qubit, B.

To facilitate a controlled interaction between the two qubits that make up this cluster definition they must be separated by an appropriate radial distance. This distance must be large enough to prevent uncontrolled entanglement but small enough that entanglement does occur when the control qubit is in the excited orbital state. If these were the only two conditions that defined the cluster, eq. (3.10) can be integrated over all depth and between the relevant radius range to find the density of viable clusters. Here an assumption is made that the shapes of both orbital states of the donors are spherical.

There are two considerations not accounted for here. If a control qubit is too close to another A donor then when in their excited orbital state their mutual interaction will interfere with the intended interaction between the control and its nearest B. Also, if there is a B close enough to the control qubits nearest B interference will be introduced for the same reason. The cluster optimised for will maximise the wanted wave function overlap but minimise the overlapping that would introduce decoherence processes.

The requirements for this viable donor cluster can be listed in terms of the nearest neighbour distance limitations for a central control (A) atom:

1. its nearest A neighbour exists outside a radius $r_{A_1} > r^{\text{min}}_{A \to A_1}$, i.e. in the region labelled '1' on fig. 3.5. This minimum ensures that when all A's are in their

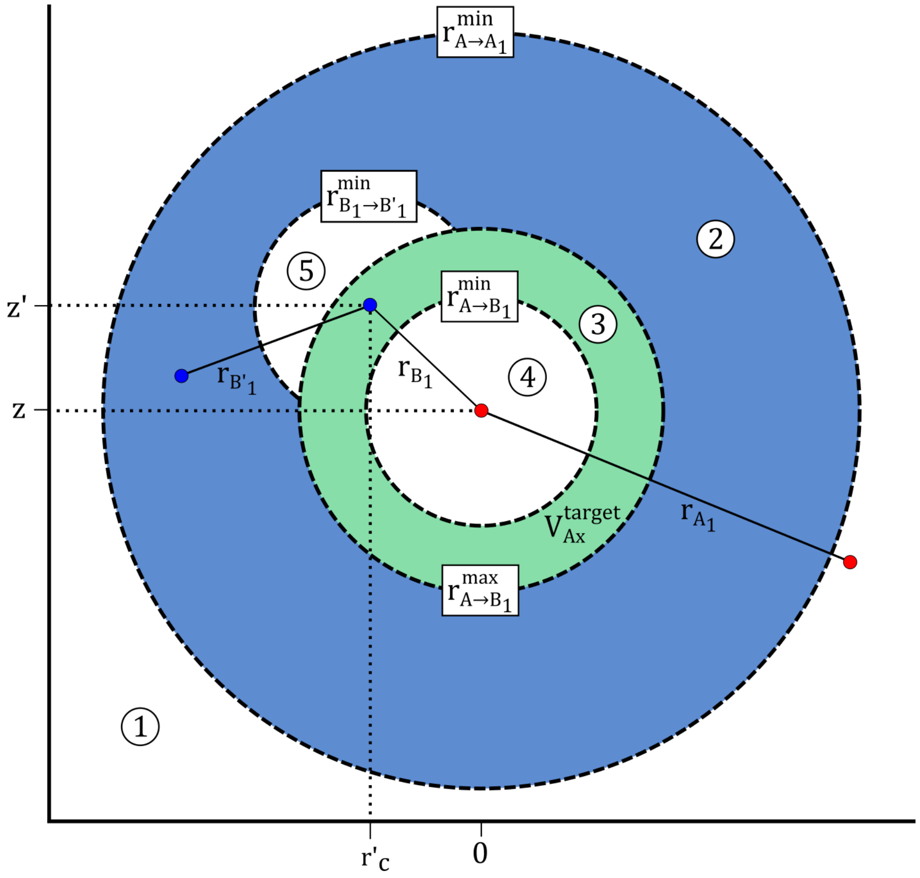

Figure 3.5: Viable two species cluster for orbital transition gated interaction

larger, excited orbitals, they do not interact with each other.

2. its nearest B neighbour exists within the range $r^{\mathrm{min}}_{A\to B_1} < r_{B_1} < r^{\mathrm{max}}_{A\to B_1}$, i.e. in the region labelled ‘3’ on fig. 3.5. This ensures that there is a target atom within range of the control atom when, and only when, the control atom is in its excited state.

3. its second nearest B exists outside the range $r_{B_2} > r^{\mathrm{max}}_{A\to B_1} + r^{\mathrm{min}}_{B\to B_1'}$, i.e. in the regions labelled ‘1’ or ‘2’ in fig. 3.5 ensuring that A and its corresponding B_1 cannot interact with any other B’s

Continuing with a cluster definition in terms of distances as listed here is problematic due to regions of space contained in multiple requirements overlapping. For the above definition, the viable locations for A’s second nearest B is dependent on where A’s nearest B exists. Instead it is easier to write out the requirements in terms of non-overlapping regions of space in which the Poisson probability of i, X events $P(i, N_X)$ can be calculated using eq. (3.2).

1. There are no A’s within the complement of region ‘1’ denoted V^{A}_{Ax} to indicate the volume around the A control atom at x from which other A’s are excluded. The number of A’s expected to exist within this region is denoted $N_A(V^{A}_{Ax})$

2. Region ‘3’, denoted V^{target}_{Ax} is the volume around the A at x in which there is exactly one B. The expected number of B’s in this volume is $N_B(V^{\mathrm{target}}_{Ax})$

3. Regions ‘4’and ‘5’contain no B’s. It is convenient to combine these regions with region ‘3’ into the volume $V^{B'}_{Ax}(x')$ that encompasses the total region of space in which there are conditions on the number of B’s. $N_B(V^{B'}_{Ax}(x'))$ is the expected number of B’s in this region.

From these criteria a viable cluster may be stated as: Given an A at x and B at x', it is required that no A’s exist in V^{A}_{Ax} and there are no B’s in $V^{B'}_{Ax}(x')$. Since a useful cluster having its B at x' is mutually exclusive with a useful cluster having its B at x'' (where x' and x'' are locations in V_{Ax}^{target}) their probabilities may be summed i.e. integrate over the allowed range of x'.

In the case of the 1D non-homogeneous problem, the probability of a B in an elemental ring at the cylindrical coordinates z' and r'_c (from the vertical axis containing the central A atom) is $2\pi r'_c n_B(z')\,\mathrm{d}r'_c\,\mathrm{d}z'$ and so,

$$\begin{aligned} P_{Az}\{\text{viable}\} = \exp\left(-N_A(V_{Az}^{A})\right) \times \\ \iint\limits_{z',\, r'_C \,\in\, V_{Az}^{\text{target}}} 2\pi r'_C n_B(z') \exp\left(-N_B\left(V_{Az}^{B'}(z', r'_C)\right)\right) \mathrm{d}r'_C\,\mathrm{d}z' \end{aligned} \tag{3.14}$$

where the expected number of B's within the region $V_{Az}^{B'}(z', r'_c)$ around an A at z and a B at z', r'_c is,

$$N_B\left(V_{Az}^{B'}(z', r'_C)\right) = \int\limits_{z'' \,\in\, V_{Az}^{B'}(z', r'_C)} S\left(V_{Az}^{B'}(z', r'_C), z''\right) n_B(z'')\,\mathrm{d}z'' \tag{3.15}$$

and $S(V, z)$ is the area of a horizontal slice at height z through V.

The area $S\left(V_{Az}^{B'}(z', r'_C), z''\right)$ is a slice through the intersection of two spheres, which can be written analytically as

$$\begin{aligned} S =& 2\pi r^2 + 2\pi R^2 - \left[r^2 \operatorname{acos}\left(\frac{{r'_C}^2 + r^2 - R^2}{2r'_C r}\right) + R^2 \operatorname{acos}\left(\frac{{r'_C}^2 + r^2 - R^2}{2r'_C R}\right) - \right. \\ & \left. \frac{1}{2}\sqrt{(-r'_C + r + R)(r'_C + r - R)(r'_C - r + R)(r'_C + r + R)} \right] \end{aligned} \tag{3.16}$$

where r and R are the radii of the intersecting circles dependant on the height through the volume of intersecting spheres. Despite this convenience eq. (3.14) is still a nested triple integral with complicated bounds. In cases where many calculations of P_z(Good cluster) are required, such as in this problem of optimising the species density profiles, it is helpful to produce a heuristic method that accelerates the numerical calculation of this probability.

3.2.2 Heuristic method to approximate cluster probability

So long as it is given that there is only B_1 within the region V_{Az}^{target}, then the probability of finding B_1 between $z' \to z' + \delta z'$ is proportional to $n(z')S(V_{Az}^{\text{target}}, z')\delta z'$. This can be used to find the location of B_1 within V_{Az}^{target} with the most important contribution to $P_z\{\text{Good cluster}\}$. Let the coordinates of this location be labelled Z'_{Az} and R'_{Az}, and let the regions '3'-'5' in fig. 3.5 around this particular configuration be $V_{Az}^{B\text{ave}'}(R'_{Az}, Z'_{Az})$ (as usual the subscript indicates it is given that there is an A control atom at z). An approximate version of eq. (3.14) can be written:

$$P_{Az}\{\text{Good cluster}\} \approx N_B(V_{Az}^{\text{target}}) \exp\Big[-N_A(V_{Az}^{A}) - N_B(V_{Az}^{B\text{ave}'}(R'_{Az}, Z'_{Az}))\Big] \tag{3.17}$$

There are a number of reasonable but different choices for calculating the most important location of the target Z'_{Az} and R'_{Az} for use in eq. (3.17). Here the expectation radius was found using eq. (3.8c)

$$R'_{Az} = \langle r' \rangle_{Az} = \frac{\int\limits_{r' \in V_{Az}^{\text{target}}} r' p_{z \to B_1}(r') dr'}{\int\limits_{r' \in V_{Az}^{\text{target}}} p_{z \to B_1}(r') dr'} \tag{3.18}$$

and the expectation depth given this spherical radius

$$Z'_{Az} = \langle z' \rangle_{Az} = \frac{\int\limits_{z-R'_{Az}}^{z+R'_{Az}} z' \frac{n_A(z')}{n_A^{2D}} C(z') dz'}{\int\limits_{z-R'_{Az}}^{z+R'_{Az}} \frac{n_A(z')}{n_A^{2D}} C(z') dz'} \tag{3.19}$$

where $C(z')$ is the circumference of the small circle of the sphere R'_{Az} through z'.

An approximate solution to this probability which is less computationally intensive accelerates the process of numerically optimising that probability. The closer the approximate solution is to the optimum found using the vigorous method, the more efficiently one can converge to an optimum Gaussian doping profile.

3.2.3 Results of optimising cluster probability

Here a numerical example of the cluster optimization is presented in the context of a silicon donor qubit gate using separation tolerance scales comparable to those estimated in literature. Such tolerances are calculated by comparing the energy scales corresponding to that of the donor excited state lifetime and the strength of exchange interactions between neighbouring elements [53]. The necessary separations required will be dependent on the donor and host semiconductor species. In this section, the separation range for the control to target donor is from $r^{min}_{A\to B_1} = 15\,\mathrm{nm}$ to $r^{max}_{A\to B_1} = 28\,\mathrm{nm}$. The exclusion radius for control to control is $r^{min}_{A\to A_1} = 60\,\mathrm{nm}$, and for target to target is $r^{min}_{B_1\to B'_1} = 15\,\mathrm{nm}$. It must be stressed that aside from being host/donor species dependent, the donor electron orbitals are also not necessarily spherically symmetric nor smoothly decaying with radius due to inter-valley interference. This computation serves to show how little chance there is of forming a simple cluster with conventional doping techniques such as broad area ion implantation where there is no control over individual defect position.

To optimise the number of good clusters four independent parameters for the Gaussian density profiles are allowed: the two areal densities n^{2D}_A and n^{2D}_B, the width of both density profiles $d_A = d_B = d$, and the separation of the two layers μ. Here the assumption is made that both profiles can be implanted at different depths with the same width. In practise, independent control of layer depth and width is not achievable with ion implantation and the depth profile for a particular implant species and target depends principally on the implant energy. It has been presented in this thesis that Bi implanted into silicon-on-insulator (SOI) material can be annealed to a high enough quality to observe signal from isolated donor orbital transitions. It has also been shown previously that Bi implanted into bulk silicon can be sufficiently electrically activated that the donor electron spin states are measurable via donor bound exciton spectroscopy [54]. The following optimisation can be used to determine a best case implant profile if the final donor profiles can be approximated as Gaussian in depth. If the final active donor profile can be measured, it may be used directly with eqs. (3.13) and (3.14) to determine the final viable cluster yield.

First the total density of good clusters, N^{2D}_{good} was maximised for a given combination of width and separation using the heuristic as detailed in the previous section. This is shown in fig. 3.6a, in which the values of $n^{2D}_{A,B}$ were varied (the resulting optimum values of $n^{2D}_{A,B}$ are not shown in this figure) for various combination of μ and d to find the optimum good cluster density N^{2D}_{good}.

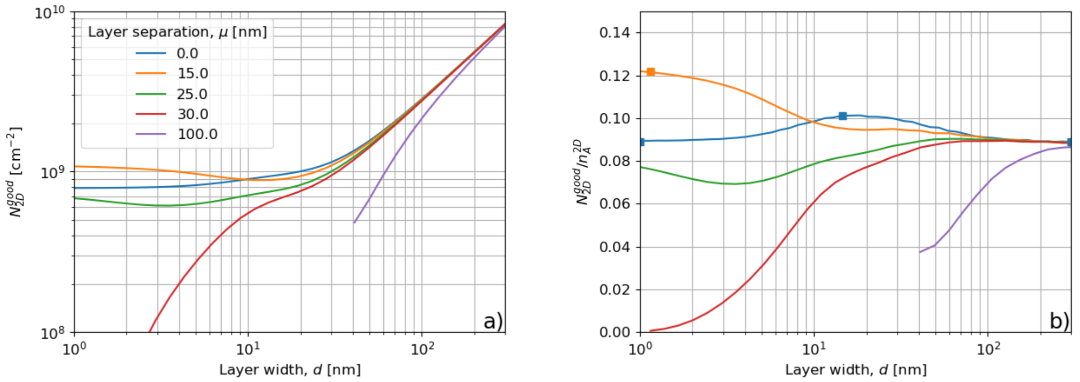

Figure 3.6: a) The optimal areal density of good clusters for two different species A, B implanted at different average depths, i.e. the layers were separated by μ shown in the legend. The density profiles of each was a Gaussian of the same width $d_A = d_B = d$, but differing total integrated areal density, $n^{2D}_{A,B}$, which were optimized using the heuristic procedure described in the text (finding R'_{Az} first). The values of $n^{2D}_{A,B}$ that produce the optimum (not shown) vary as a function of both d and μ. b) The proportion of A donors involved in a good cluster i.e. $N^{2D}_{\text{good}}/n^{2D}_A$ after optimizing for N^{2D}_{good} as graphed in fig. 3.6a

For sufficiently large layer widths layer separation clearly has no effect on either N^{2D}_{good} or $N^{2D}_{\text{good}}/n^{2D}_A$. In this limit the optimum values of $n^{2D}_A d_A = n^{2D}_B d_B$ tend to the optimum homogeneous bulk densities [53]. Here it is seen that for layers spaced far apart the density of viable clusters tends to zero as the layer width is reduced, as expected as it becomes increasingly difficult to obtain an $A \rightarrow B$ distance within the allowed range. For very narrow layers, there is an obvious optimum layer separation of 15 nm. This distance is the same as the minimum separation of control from target. For intermediate layer widths of around 10 nm the lines cross, and the optimum is now obtained for layers of zero separation, i.e. the target and control layers should be at the same depths to maximise the density of viable clusters.

The areal density N^{2D}_{good} is not necessarily the most useful optimization objective function. Even with a small density, the total number of good clusters may be increased simply by increasing the sample size. The ratio of signal to background in an experiment might be improved if instead the fraction of donors that are involved in a good cluster is maximised. For example, an experiment is imagined where the effects of the interaction are detected by measuring the effect on the spin of the A's after orbitally exciting the A's (which produces an effect only for those A's that are part of a good cluster). In the cluster of interest depicted in fig. 3.5 there is only one A per cluster, so the number of A's involved in a good cluster is equal to the number of good clusters, and the signal-to-background will be optimized by maximising the fraction $N^{2D}_{\text{good}}/n^{2D}_{A}$. By simply maximising this fraction, the optimum occurs when n^{2D}_{A} is as small as possible. In this limit the condition on the control's nearest A ($r_{A \to A_1} > 60$nm) becomes guaranteed, and the only conditions that needs to be satisfied are the ones on the nearest and next-nearest B's. Alternatively, a different experiment where the effect of the interaction in detected by measuring the effect on the spin of the B's after exciting the A's, and therefore optimising the fraction $N^{2D}_{\text{good}}/n^{2D}_{B}$ is desired, which occurs when n^{2D}_{B} is as small as possible for a similar argument. To avoid these cases where the optimum density of a species tends to zero, the absolute number of good clusters which optimises the total signal (fig. 3.6a) was found, and subsequently the corresponding fraction $N^{2D}_{\text{good}}/n^{2D}_{A}$ describing the ratio of signal to background shown in fig. 3.6b was found.

fig. 3.6b shows that if one were able to fabricate atomically flat layers separated in depth then this fraction is optimised when such layers are separated by 15nm. An interesting situation arises if there is a lower limit on the possible width of the density profiles. This is the case when ion implanting species into a lattice. Depending on the implantation specifics, it is difficult to make very thin layers due to ion straggle and diffusion. fig. 3.6 shows that if the layers cannot be fabricated with widths less than 10nm, the optimum configuration is to have the two species co-planar ($\mu = 0$) with widths of $\approx$ 15nm (not to be as thin as possible) achieving a reasonable 10%. The fractions in both of these cases are an improvement over the optimised, bulk dope case achieving a good cluster fraction of 9%. The results of three doping configurations were simulated using a brute force (Monte Carlo) approach (filled squares with error) confirming the densities as calculated by eq. (3.13).

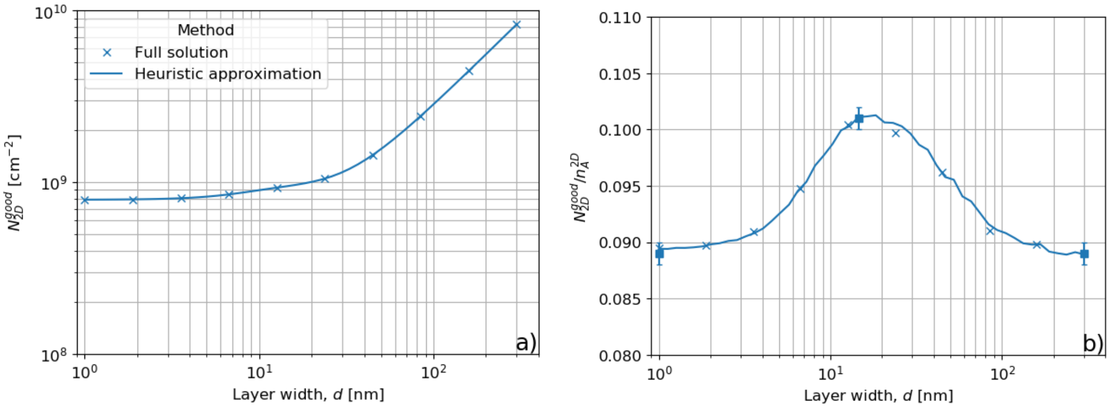

Figure 3.7: In the co-planar ($\mu = 0$) configuration the heuristic method agrees very well with the optimum found using the full integral result for the density of viable clusters. Both methods are shown to be in agreement with a brute force approach (filled squares with error). The error in the brute force result was minimised through repeated simulation. Like the full solution, optimising using the brute force approach is considerably more impractical than the solution found using a suitable heuristic.

The quality of the optimization is shown in fig. 3.7, in which the solutions are compared with optimization using the full solution of eqs. (3.14) and (3.15), and also using a brute force (Monte Carlo) method. Agreement is excellent for cases examined here where the two species profiles overlap in depth. The heuristic method becomes less reliable when the layers are thinner than the separation between layers as shown in fig. 3.8. Under these circumstances the optimum B density can differ by as much as two orders of magnitude.

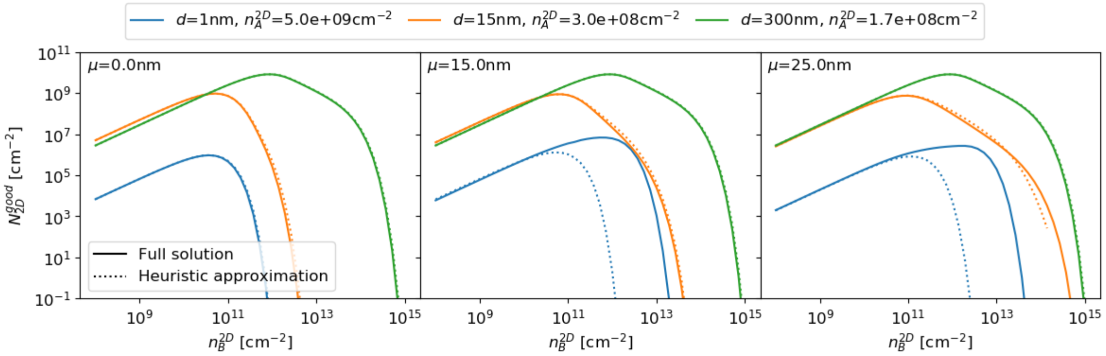

Figure 3.8: The density of viable clusters plotted as a function of the areal density of B donors. The same optimum B is found using either the heuristic (dashed lines) of full solution (solid lines). These methods where compared for different layer widths (coloured lines) and different layer separations (separate subplots). The discrepancy between methods is only apparent for layers whose profile width is smaller than their separation.

3.3 Conclusion

In this chapter, Poisson process statistics has been introduced to describe the distribution of dopant-dopant separations in extrinsic semiconductors. When the dopant density is homogeneous, solutions to the nearest neighbour separation distribution are textbook results. This is however, not the case for the analytical solution found here (eq. (3.8c)) for a non-homogeneous process where the density has been allowed to vary as a Gaussian function in one dimension. This situation of non-homogeneous doping is a good approximation for the dopant density distribution in depth after broad area ion implantation.

It is easy to extend this formalism to systems of more than one dopant species, both described by 1D density variation whose interspecies separation is of interest. The nearest neighbour cluster definition (size of sphere around a dopant which contains no other dopants of a particular species) was extended to a more complicated cluster definition where there are limits on 'A's nearest A and B' and also 'A's nearest B's nearest B'. Although the integral to compute the probability of an A being at the centre of such a cluster can be written down it is time consuming to compute especially when repeated calculation is required i.e. optimisation. To accelerate calculation of the most optimum Gaussian density profile parameters in favour of the complicated cluster definition studied here a heuristic can be used to make assumptions on the most likely location of 'A's nearest B'. The limitations of such a heuristic is found through comparison with the full solution which may also be verified via brute force i.e. populating a space and finding cluster by computing the distances in a Monte Carlo fashion.

It is observed that there is little improvement in the optimum density of clusters (those studied here) when separating the two species into two Gaussian layers above simply homogeneously doping in the bulk or plane. Interestingly, separated layers becomes better than co-planar layers when the width of the layer approaches that of the ideal interspecies distance.

Chapter 4

Contactless detection of Si:P orbital dynamics in magnetic field

In this chapter, the magnetic field dependence of orbital state coherence times are investigated. Coherence times are extracted from an electrically detected Ramsey measurement using a coherent pulsed free electron laser (FEL). This chapter begins with an introduction to the theory of coherent light-matter interaction. This background is critical to understand the experimental spectra taken later. The ordinary differential equations (ODEs) required to model the time dynamics of qubit state probabilities, namely the optical Bloch equations [55], are derived and used to simulate photo-thermal ionisation spectroscopy (PTIS) of a qubit system interacting with pulsed coherent light. By fitting experimental data with this model, the relaxation and dephasing coherence times of the Si:P $1s(A_1) \rightarrow 2p_+$ and $1s(A_1) \rightarrow 3p_+$ transitions were found. The coherent dynamics of these transitions were evaluated at different magnetic field strengths. This was possible as the FEL could be tuned to be in resonance with the atoms. Evaluating the coherent dynamics of donor orbital transitions under field is useful since a variable external field gives control on both the orbital and spin state energy spectrum. A magnetic field is required in the Stoneham Fisher Greenland (SFG) scheme to lift the degeneracy of the qubit donor spin states. There therefore may be an optimum field to choose which aids in the qubit gate operation mediated by the orbital transition of the intermediary donor in the SFG scheme. This freedom to choose a resonant frequency of an orbital transition also allows one to avoid resonant absorbers external to the sample such as water vapour and also phonon resonances in the sample that may enhance relaxation.

4.1 Coherent light-qubit interaction

An electron bound to a group-V donor in silicon in its ground state can be optically excited into a mixed state such that there is a finite probability of it being in both the ground and higher energy eigenstate. These probabilities are not necessarily constant in time. To model the time evolution of a hydrogenic system with coherent light pulses it is helpful to begin by writing the time-dependent Schrödinger equation

$$\hat{H}\Psi(t,\mathbf{r}) = i\hbar\frac{\mathrm{d}\Psi(t,\mathbf{r})}{\mathrm{d}t} \tag{4.1}$$

The time-independent Hamiltonian, H_0, associated with the potential and kinetic energies of an isolated atom can be shown to give solutions of $\Psi(t,\mathbf{r})$ in the form

$$\Psi_n(t,\mathbf{r}) = \exp(-iE_n t/\hbar)\psi_n(\mathbf{r}) \tag{4.2}$$

where the real parts of the eigenstates are stationary (only dependent on position) but which have a complex phase that oscillates in time. One may consider only two atomic eigenstates, Ψ_1 and Ψ_2, between which a transition is made, as a good approximation for the whole system when the light is close to resonance with that particular transition. The total wave function of the donor-bound electron is then written as a mixed state of only two wave functions.

$$\Psi(t,r) = c_1(t)\Psi_1(t,r) + c_2(t)\Psi_2(t,r) \tag{4.3}$$

where c_1 and c_2 are complex numbers that can change with time and describe the mixed state composition while preserving the certainty of measuring the electron in either of the two states. The absolute squared values of these coefficients are the probabilities of measuring the system in each state and the sum of these probabilities must be 1 for all moments in time.

4.1.1 Interaction with light

It is standard to write the Hamiltonian of a two level system interacting with light as the sum of the unperturbed Hamiltonian with an interaction Hamiltonian

$$H(t) = H_0 + H'(t) \tag{4.4}$$

The interaction Hamiltonian of the atom with light depends on both time and space due to nature of propagating light. However, the spacial variation can be neglected when the wavelength of light is much greater than the size of the electron wave function. This is true for donor orbital states (10 nm) and infrared light in the THz region (10 μm).

Substituting the total system wave function and perturbed Hamiltonian into the time dependent Schrödinger equation leads to

$$H'(c_1\Psi_1 + c_2\Psi_2) = i\hbar(\Psi_1\frac{\mathrm{d}c_1}{\mathrm{d}t} + \Psi_2\frac{\mathrm{d}c_2}{\mathrm{d}t}) \tag{4.5}$$

This equation, when pre-multiplied by Ψ_1^* or Ψ_2^* and integrated over all space, obtains a set of two coupled differential equations for c_1 and c_2, namely

$$c_1 \int \psi_1^* H' \psi_1 \mathrm{d}V + c_2 \exp(-i\omega_0 t) \int \psi_1^* H' \psi_2 \mathrm{d}V = i\hbar \frac{\mathrm{d}c_1}{\mathrm{d}t} \tag{4.6a}$$

$$c_2 \int \psi_2^* H' \psi_2 \mathrm{d}V + c_1 \exp(i\omega_0 t) \int \psi_2^* H' \psi_1 \mathrm{d}V = i\hbar \frac{\mathrm{d}c_2}{\mathrm{d}t} \tag{4.6b}$$

Where ω_0 is the resonant frequency $(E_2 - E_1)/\hbar$. It is convenient to introduce the shorthand

$$\hbar I_{ij} = \int \psi_i^* H' \psi_j \mathrm{d}V \tag{4.7}$$

such that

$$c_1 I_{11} + c_2 \exp(-i\omega_0 t) I_{12} = i \frac{\mathrm{d}c_1}{\mathrm{d}t} \tag{4.8a}$$

$$c_2 I_{22} + c_1 \exp(i\omega_0 t) I_{21} = i \frac{\mathrm{d}c_2}{\mathrm{d}t} \tag{4.8b}$$

The interaction Hamiltonian can include many terms however the most important for the case of orbital excitation of atoms is the electric dipole interaction.

$$H' = eD \cdot E_0 \cos(\omega t) \tag{4.9}$$

where $-eD$ is the total electric dipole moment of the atom and D is the vector sum of the Z electron positions relative to the atomic nucleus.

$$D = \sum_{j=1}^{Z} \mathbf{r}_j \tag{4.10}$$

Since the interaction Hamiltonian is both real and has odd parity under inversion about the nucleus $(H'(-\mathbf{r}) = -H'(\mathbf{r}))$ the diagonal terms of I must be 0.

If the incident light is linearly polarised, only the dipole moment induced along the polarisation axis e.g. $D = D_x$ is required. The matrix element I_{ij} becomes,

$$I_{ij} = (eE_0 X_{ij}/\hbar) \frac{\exp(i\omega t) + \exp(-i\omega t)}{2} \tag{4.11}$$

where

$$X_{ij} = \int \psi_i^* D_x \psi_j dV \tag{4.12}$$

These numerical pre-factors can be grouped together such that

$$I_{ij} = I_{ji}^* = \Omega \frac{\exp(i\omega t) + \exp(-i\omega t)}{2} \tag{4.13}$$

Substituting these interaction terms into eq. (4.8) ad after some rearrangement leads to,

$$\frac{\mathrm{d}c_1}{\mathrm{d}t} = -\frac{i}{2} c_2 \Omega (\exp(i\Delta t) + \exp(-i(\omega + \omega_0)t)) \tag{4.14a}$$

$$\frac{\mathrm{d}c_2}{\mathrm{d}t} = -\frac{i}{2} c_1 \Omega^* (\exp(-i\Delta t) + \exp(i(\omega + \omega_0)t)) \tag{4.14b}$$

Where $\Delta = \omega - \omega_0$ is the detuning of the laser relative to the transition. The rapidly oscillating terms $(\exp(\pm i(\omega + \omega_0)t)$ may be omitted as when integrating over time scales of interest they average to 0 when the light is close to resonance and the intensity is low. At low intensity the Rabi frequency, Ω is much lower than the transition frequency. Removing the rapidly oscillating terms from the optical Bloch equations like this is known as the rotating wave approximation.

4.1.2 Density matrix master equation

It is convenient to write the equations of motion for this system in density matrix form for systems containing an ensemble of individual two level atoms. These systems contain many individual two-level qubits whose mean state probabilities are the experimentally measurable observables.

$$\rho = \begin{pmatrix} c_1 \\ c_2 \end{pmatrix} \begin{pmatrix} c_1^* & c_2^* \end{pmatrix} = \begin{pmatrix} c_1 c_1^* & c_1 c_2^* \\ c_2 c_1^* & c_2 c_2^* \end{pmatrix} = \begin{pmatrix} \rho_{11} & \rho_{12} \\ \rho_{21} & \rho_{22} \end{pmatrix} \tag{4.15}$$

The rate equations for these probabilities are then calculated using the product rule of differentiation from eq. (4.14). Within this master equation, time derivative have been denoted with dots rather than $\frac{\mathrm{d}}{\mathrm{d}t}$'s to save space.

$$\dot{\rho} = \begin{pmatrix} \dot{c_1}c_1^* + c_1\dot{c_1^*} & \dot{c_1}c_2^* + c_1\dot{c_2^*} \\ \dot{c_2}c_1^* + c_2\dot{c_1^*} & \dot{c_2}c_2^* + c_2\dot{c_2^*} \end{pmatrix} = \begin{pmatrix} \dot{\rho_{11}} & \dot{\rho_{12}} \\ \dot{\rho_{21}} & \dot{\rho_{22}} \end{pmatrix} = \begin{pmatrix} -\dot{\rho_{22}} & \dot{\rho_{12}} \\ \dot{\rho_{12}}^* & \dot{\rho_{22}} \end{pmatrix} \tag{4.16}$$

$$\begin{pmatrix} \dot{\rho_{11}} \\ \dot{\rho_{12}} \\ \dot{\rho_{21}} \\ \dot{\rho_{22}} \end{pmatrix} = \begin{pmatrix} 0 & \frac{i\Omega^*(t)}{2}\exp(-i\Delta t) & -\frac{i\Omega(t)}{2}\exp(i\Delta t) & 0 \\ \frac{i\Omega(t)}{2}\exp(i\Delta t) & 0 & 0 & -\frac{i\Omega(t)}{2}\exp(i\Delta t) \\ -\frac{i\Omega^*(t)}{2}\exp(-i\Delta t) & 0 & 0 & \frac{i\Omega^*(t)}{2}\exp(-i\Delta t) \\ 0 & -\frac{i\Omega^*(t)}{2}\exp(-i\Delta t) & \frac{i\Omega(t)}{2}\exp(i\Delta t) & 0 \end{pmatrix} \begin{pmatrix} \rho_{11} \\ \rho_{12} \\ \rho_{21} \\ \rho_{22} \end{pmatrix} \tag{4.17}$$

Note that in eq. (4.17), Ω has been written as a function of time, this is to say that E_0 in eq. (4.11) is a function of time and allows pulses of light to be modelled.

Equation (4.14) states that the coefficients c_1 and c_2 do not change when there is no light interacting with the system i.e. when $\Omega = 0$. In reality, spontaneous emission occurs during the dark to relax the system back to the ground state. A relaxation rate, γ_{21} is introduced such that in the dark, the probability of finding an electron in the excited state decays as $\rho_{22}(t) = \rho_{22}(0)\exp(-\gamma_{21}t)$. To achieve this, eq. (4.14b) is amended such that

$$\frac{\mathrm{d}c_2}{\mathrm{d}t} = -\frac{i}{2}c_1\Omega^*\exp(-i\Delta t) - \frac{\gamma_{21}}{2}c_2 \tag{4.18}$$

and eq. (4.17) becomes

$$\begin{pmatrix} \dot{\rho}_{11} \\ \dot{\rho}_{12} \\ \dot{\rho}_{21} \\ \dot{\rho}_{22} \end{pmatrix} = \begin{pmatrix} 0 & \frac{i\Omega^*(t)}{2}\exp(-i\Delta t) & -\frac{i\Omega(t)}{2}\exp(i\Delta t) & \gamma_{21} \\ \frac{i\Omega(t)}{2}\exp(i\Delta t) & -\frac{\gamma_{21}}{2} & 0 & -\frac{i\Omega(t)}{2}\exp(i\Delta t) \\ -\frac{i\Omega^*(t)}{2}\exp(-i\Delta t) & 0 & -\frac{\gamma_{21}}{2} & \frac{i\Omega^*(t)}{2}\exp(-i\Delta t) \\ 0 & -\frac{i\Omega^*(t)}{2}\exp(-i\Delta t) & \frac{i\Omega(t)}{2}\exp(i\Delta t) & -\gamma_{21} \end{pmatrix} \begin{pmatrix} \rho_{11} \\ \rho_{12} \\ \rho_{21} \\ \rho_{22} \end{pmatrix} \tag{4.19}$$

The oscillating terms can also be removed by changing to a rotating reference frame where $\tilde{\rho}_{12} = \rho_{12}\exp(-i\Delta t)$ and $\tilde{\rho}_{21} = \rho_{21}\exp(i\Delta t)$

$$\begin{pmatrix} \dot{\rho}_{11} \\ \dot{\tilde{\rho}}_{12} \\ \dot{\tilde{\rho}}_{21} \\ \dot{\rho}_{22} \end{pmatrix} = \begin{pmatrix} 0 & \frac{i\Omega^*(t)}{2} & -\frac{i\Omega(t)}{2} & \gamma_{21} \\ \frac{i\Omega(t)}{2} & -\frac{\gamma_{21}}{2} - i\Delta & 0 & -\frac{i\Omega(t)}{2} \\ -\frac{i\Omega^*(t)}{2} & 0 & -\frac{\gamma_{21}}{2} - i\Delta & \frac{i\Omega^*(t)}{2} \\ 0 & -\frac{i\Omega^*(t)}{2} & \frac{i\Omega(t)}{2} & -\gamma_{21} \end{pmatrix} \begin{pmatrix} \rho_{11} \\ \tilde{\rho}_{12} \\ \tilde{\rho}_{21} \\ \rho_{22} \end{pmatrix} \tag{4.20}$$

Spontaneous emission is not the only mechanism by which phase is lost. Elastic scattering events can cause the phase of a superposition state to be randomised while preserving probability. This pure dephasing rate is denoted Γ and must be added to eq. (4.20) alongside the dephasing caused by relaxation.

In the system of interest the qubit states are two, bound donor electron orbitals. By experimental design, there is enough thermal energy in the system capable of ionising excited state electrons into the conduction band with rate G. This effect is included in an ad hoc manner as previously reported [42] to the master equation to behave similarly to γ_{21}. In the case of thermal ionisation however. The probability is transferred from the excited state out of the two level system instead of down to

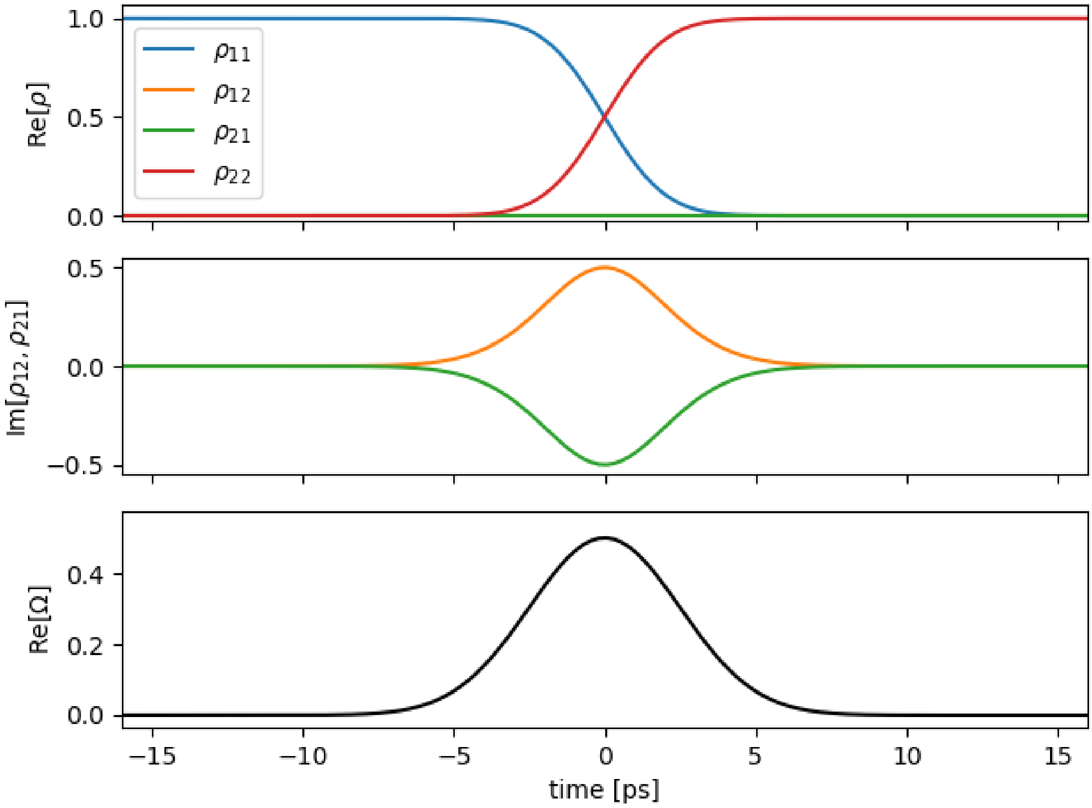

Figure 4.1: Solution to the density matrix differential equations for an on resonant, Gaussian pulse of light with $\int \Omega(t)\,\mathrm{d}t = \pi$. No decoherence terms are included so the resulting excited state probability persists in the dark after the pulse of light. The diagonal components of ρ are purely real as expected but the off-diagonal ones are complex.

the ground state so no $+G\rho_{11}$ appears in the equation for $\dot{\rho_{11}}$.

$$\begin{pmatrix}\dot{\rho_{11}}\\ \dot{\rho_{12}}\\ \dot{\rho_{21}}\\ \dot{\rho_{22}}\end{pmatrix} = \begin{pmatrix} 0 & \frac{i\Omega^*(t)}{2} & -\frac{i\Omega(t)}{2} & \gamma_{21} \\ \frac{i\Omega(t)}{2} & -\frac{\gamma_{21}}{2} - \Gamma + i\Delta - \frac{G}{2} & 0 & -\frac{i\Omega(t)}{2} \\ -\frac{i\Omega^*(t)}{2} & 0 & -\frac{\gamma_{21}}{2} - \Gamma - i\Delta - \frac{G}{2} & \frac{i\Omega^*(t)}{2} \\ 0 & -\frac{i\Omega^*(t)}{2} & \frac{i\Omega(t)}{2} & -\gamma_{21} - G \end{pmatrix} \begin{pmatrix}\rho_{11}\\ \rho_{12}\\ \rho_{21}\\ \rho_{22}\end{pmatrix} \tag{4.21}$$

Throughout this chapter eq. (4.21) is solved numerically for various $\Omega(t)$, Γ, γ_{21}, G and Δ as exemlified in fig. 4.1 for Gaussian $\Omega(t)$ and $\Gamma = \gamma_{21} = G = 0$. If multiple pulse envelopes are present in $\Omega(t)$ they are modelled to be exact phase copies of eachother i.e. they have the same phase relative to their respective Gaussian envelope. This phase relation between pulses mimics how the pulse sequences are produced in the particular experimental setup used here. The ordinary differential equation solver was written using the Python module SciPy which contains a wrapper function to the Fortran ODEPACK routine ‘zvode’ which solves complex-valued variable-coefficient ordinary differential equations such as eq. (4.21). The agreement of the numerical solution with textbook results verifies the simulators reliability. In fig. 4.1 probabilities are inverted for an on-resonant π-pulse as expected. In fig. 4.3 Ramsey fringes are observed at the expected frequency and decay envelope for the chosen decay constants.

4.1.3 The Bloch sphere

A useful representation of the density matrix vector ρ is the Bloch sphere. A 3D vector is defined with coordinates,

$$\begin{aligned} x &= 2\,\mathrm{Re}[\rho_{12}] \\ y &= 2\,\mathrm{Im}[\rho_{21}] \\ z &= \rho_{22} - \rho_{11} \end{aligned} \tag{4.22}$$

such that the poles, $z = -1$ and $z = 1$ represent the system with 100% certainty of being in either the ground or excited state respectively. The cylindrically radial component of the Bloch vector represents the coherence of the system with pure states existing at the surface of the unit sphere. A Bloch vector with a length less < 1 describes a mixed state due to the statistical ensemble of qubits. Rotations of the Bloch vector about this space are achieved with coherent pulses of light. The angle is determined by the time integral of $\Omega(t)$ such that a 90° rotation of the Bloch vector about a vector that is in the equatorial plane is achieved with an on-resonance pulse area of $\pi/2$. Such a pulse is therefore called a $\pi/2$-pulse. If the light is off resonance, a pulse with the same area does a different rotation angle about an axis out of the x-y plane.

In the Bloch sphere representation, the effect of dephasing mechanisms can be abstractly described as a shortening of the cylindrical component of the Bloch vector about the z axis. Relaxation mechanisms on the other hand, cause the z component of the Bloch vector to decrease in time indicating the reduced probability of finding the donor in its excited state. There are different labelling conventions used in different scientific disciplines when discussing the time scales associated with decoherence mechanisms of two level systems. So to be explicit here: $T_1 = 1/\gamma_{21}$ is the relaxation time, and $T_2' = 1/\Gamma$ is the pure dephasing time. As seen in eq. (4.21), the rate of dephasing caused by relaxation happens at half the rate at which the probability changes so that the total homogeneous dephasing rate is given by

$$\frac{1}{T_2} = \frac{\gamma_{21}}{2} + \Gamma \tag{4.23}$$

Figure 4.2 shows a simulation of a two level atom interacting with two sequential Gaussian $\pi/2$-pulses of, the second of which is a carrier envelope phase copy of the first delayed in time. Although the input pulse areas are both $\pi/2$, decoherence occurring during the pulses causes the full 90° rotation not to be achieved and an

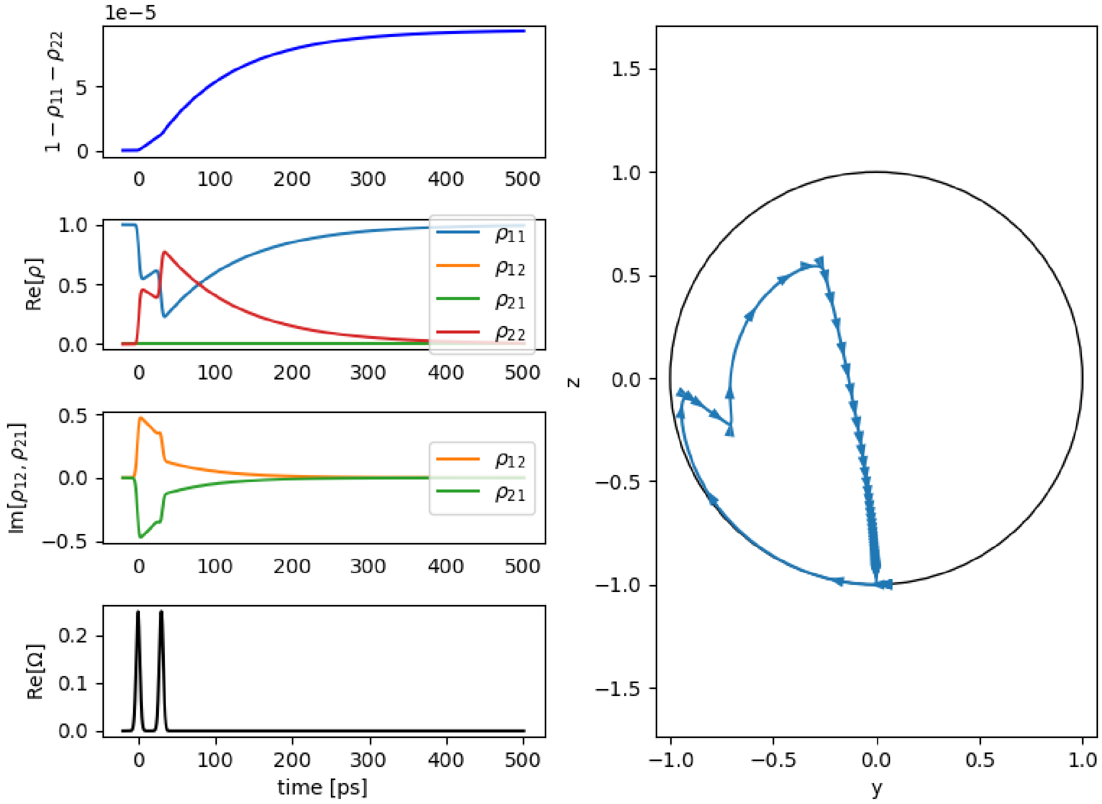

Figure 4.2: The effect of two, finite width Gaussian, $\frac{\pi}{2}$-pulses separated in time by 30 ps on the Bloch vector describing an ensemble of two level atoms. In this example the oscillators are effected by relaxation and pure dephasing broadening with rates $\gamma_{21} = \Gamma = 0.01\,\mathrm{ps}^{-1}$. A much slower leakage into the continuum is also included $G = 10^{-6}\,\mathrm{ps}^{-1}$. The south and north poles of the Bloch sphere represent the ground and excited states respectively. The path marked out within the y-z plane of the Bloch sphere shows how the Bloch vector moves in time. For this pulse delay and detuning (on-resonance) the second pulse interferes constructively with the evolving transition; the probability of being in the excited state is enhanced and therefore so is the rate of leakage in the conduction band immediately after the sequence.

equal superposition state is not achieved after the first pulse. In the time after the first pulse the conduction band starts to populate alongside relaxation (decrease in ρ_{22}) and dephasing (change in the coherence ρ terms). In this reference frame there is no precession of the vector about the z axis since there is no detuning $\Delta = 0$. The second pulse, in this example, has a phase such that it interferes constructively with the evolving superposition and enhances the probability of finding atoms in the excited state. The increase in excited state probability causes a faster rate of thermal ionisation and further increases the conduction band population. The rate of increase of the conduction band population eventually slows down as the excited state is depleted and the system relaxes leaving a final density of electrons in the conduction band.

The two decoherence mechanisms described so far are both homogeneous mechanisms i.e. the same for all oscillators in the system. Inhomogeneous broadening is a general term which describes the effect of decoherence mechanisms arising due to a statistical distribution of resonant frequencies which causes an additional dephasing to the system. The total dephasing rate width of a transition including inhomogeneous dephasing is then

$$\frac{1}{T_2^*} = \frac{1}{T_2} + W \tag{4.24}$$

where W is the full width at half maximum (FWHM) of the resonant frequency distribution. eq. (4.24) describes the decay of ρ_{21} (and ρ_{12}) and works phenomenologically in the limit that $1/T_2 \gg W$ or $W \gg 1/T_2$. When W is large, the decay is not exponential but Gaussian instead. In the context of the Bloch sphere representation, inhomogeneous broadening can be pictured as the smooth fanning out of a collection of individual qubit Bloch vectors (on the sphere surface at a constant z) in time. This is different to pure dephasing, whereby individual qubit Bloch vectors change phase (azimuthal angle) randomly. Both effects cause a shortening of the

Bloch vector. To include inhomogeneous broadening in the model, a convolution of the homogeneous line shape is done with the inhomogeneous line shape. In this case the spectral line shape of the conduction band population at the end of the sequence, $n(\Delta)$ is t therefore,

$$n(\Delta) = \int_{-\infty}^{\infty} [1 - \rho_{11}(\Delta', t_f) - \rho_{22}(\Delta', t_f)] g(\Delta - \Delta', W) \, \mathrm{d}\Delta' \tag{4.25}$$

4.2 Ramsey spectroscopy

To observe how the superposition state created by a pulse of coherent light evolves in time one can wait some time after exciting with a first pulse and observe how the state probabilities redistribute after a second pulse. Whether or not the second pulse is in phase with the superposition state upon arrival, a different final state is expected if the superposition state has retained a coherent phase. As the phase difference between the state and the light is swept, the oscillations in signal strength due to the oscillation in final state probabilities are called Ramsey fringes. This effect is named after Norman Ramsey who used this technique of separated oscillatory fields to measure the atomic transitions of particles in molecular beams with improved accuracy [56].

To cause the change in phase between light pulses and the superposition state, the simplest thing to do (when you have envelope phase pulse copies) can be to change the time delay between the two light pulses as demonstrated in fig. 4.3.

The ratio between the final exited state probability after two, in phase, pulses relative to that after one pulse, R clearly depends on the pulse area, A. Geometrically this ratio R can be written as:

$$R = \frac{1 - \cos 2A}{1 - \cos A} \tag{4.26}$$

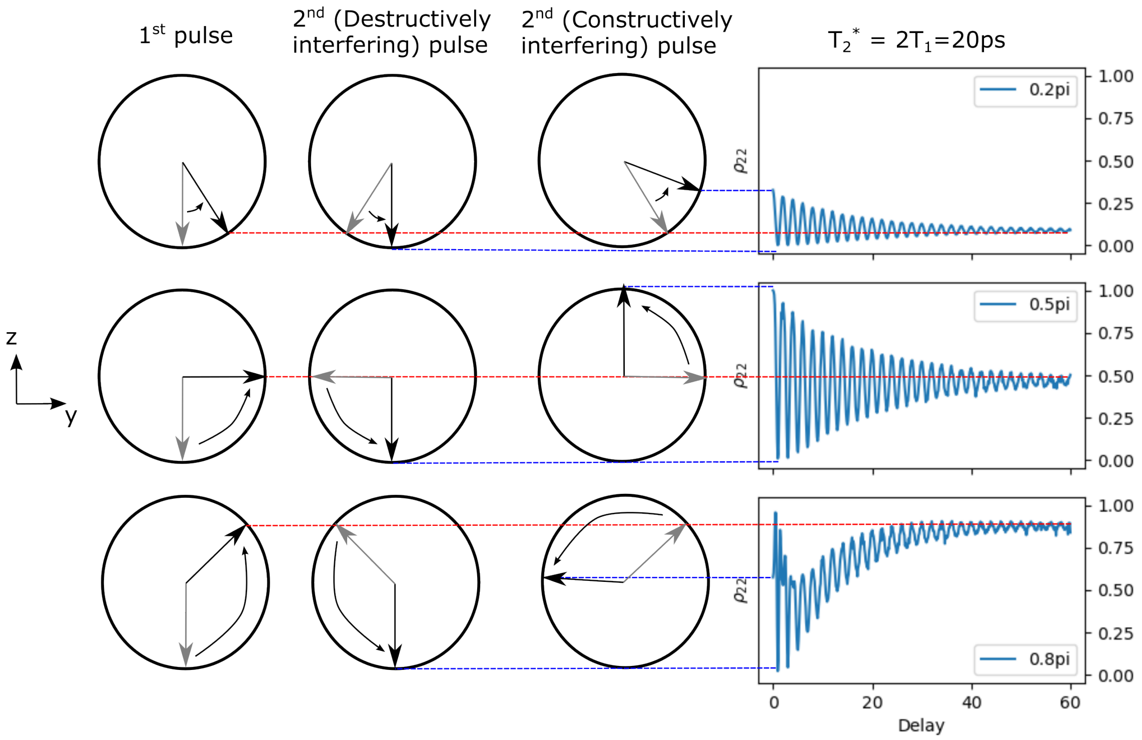

Figure 4.3: The effect of the second pulse in a Ramsey sequence on the resulting excited state probability a short time after the second pulse depending on pulse area of both pulses and delay of the second pulse. A clear dependence of the fringe envelope with pulse area is seen.

when decoherence can be ignored. This ratio is maximised for exceedingly small pulse areas such that,

$$\lim_{A\to 0} \frac{1-\cos 2A}{1-\cos A} = \lim_{A\to 0} 2(1+\cos A) = 4 \tag{4.27}$$

and R is minimised to 0 when A is an odd integer multiple of π i.e. the second pulse results in 0% probability of finding the atom in its excited state. Although R is maximised for small pulse areas, the biggest difference in signal between the second pulse arriving in phase versus out of phase (largest fringe contrast) is found when the pulse areas are odd integer multiples of $\pi/2$; the first pulse puts the atom in equal probability of being found in the ground or excited state and the second changes the excited state probability to either 0 or 100% depending on its phase. As phase information is lost due to the system decohering over time, the amplitude of the Ramsey fringes decreases due to the shortening of the Bloch vector.

The fringes within the delay scan fringe envelope have a period equal to that of the two level resonance. The time constant of the exponential decay of the fringe amplitude is the total dephasing time, T_2^* as defined previously.

4.2.1 Extracting decoherence terms from PTIS data

The optical Bloch equations as defined here with the modifications to account for leakage from the two-level system into the conduction band assume that there is negligible recombination of ionised electrons during the two pulse sequence. In reality free electrons are able to recombine with ionised donors and repopulate the ground state at any time. Here it is assumed that complete recombination happens in the 40 ns time between successive two-pulse sequences in the free electron laser for infrared experiments (FELIX) macropulse. This is a convenient assumption because it means that the average conduction band population throughout the macropulse is effectively modelled by only a single two-pulse sequence thus limiting the time span over which the ODEs must be solved numerically.

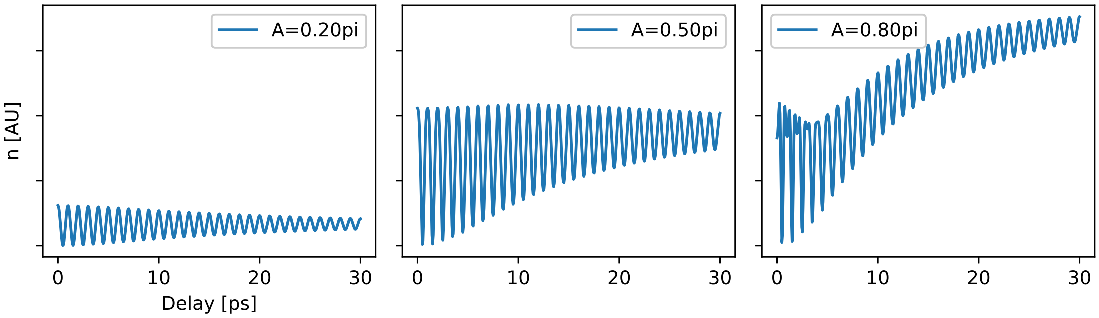

Figure 4.4: Modelled Ramsey fringes in the time domain whereby measured signal is the resulting conduction band density after the two pulse sequence. Three different pulse areas are modelled demonstrating the differences in the fringe envelope shape to that is the excited state probability were directly measured (as in fig. 4.3).

Using eqs. (4.20) and (4.25) the resulting conduction band population after a single two pulse sequence can be computed as a function of the pulse delay. In fig. 4.4 delay scans are again modelled for the same system shown in fig. 4.3 only this time with final conduction band population shown on the y-axis. Clearly there is stark contrast in the shape of equivalent pulse area fringe envelopes when detecting conduction band density rather than the excited state population directly. The most symmetric fringe envelope is achieved at low pulse area for PTIS but at $A = \pi/2$ if the probability is directly measured. In both methods maximum fringe contrast is achieved with $\pi/2$-pulses.

To acquire unaliased Ramsey oscillations in the time domain to be able to measure their amplitude reliably, the pulse delay must be sampled with a step size of at most, half the transition period. With the donor orbital transition frequencies of interest here being of the order 10 THz, the required delay step size is on the order of 0.05 ps. To cause such a small delay the Michelson interferometer arm must move in steps of $<10\,\mu$m. Although such resolution is possible and has been demonstrated [42,57], the number of data points from such fine scans over broad delay ranges ($T_2^* \approx 30$ ps) required to see decoherence are excessive for fitting a simple exponential decay. To efficiently measure coherence times over a wide range of experimental conditions in limited beam and magnet time, it is convenient in this instance to instead scan in the frequency domain for a small selection of pulse delays.

In time domain Ramsey spectroscopy, signal oscillates with a period equal to the transition resonance. In this setup, the moving interferometer arm would have to move in increments smaller than 1/2 the wavelength ($6\,\mu\mathrm{m}$) to avoid aliasing and over a large distance ($1\,\mathrm{cm}$) to fully capture the decay. There are adjustments that could be made to improve the data collection speed of time domain measurements such as collecting high time resolution scans not over the whole decay envelope but a few sections.

In the frequency domain it is possible to generate Ramsey fringes by sweeping the transition energy of the two level system through the laser frequency for a fixed subset of delays between the two pulses. In this domain, the oscillation period depends on the time delay between the pulses and the sweep rate of the variable magnet allowed efficient capture of Ramsey fringes for a selection of time delays. Ramsey fringes do not appear if the laser frequency is swept through a fixed transition frequency, only when the transition is swept through a fixed laser frequency. The origin of this asymmetry is that there is not only a phase difference between the second pulse and the evolving atom but also between the second pulse and the initial laser pulse when the pulses are exact phase copies. These two phase differences act such that the second pulse always arrives in phase. In the situation when the atom frequency is varied there is only the phase difference between the evolving atom and the second laser pulse to consider. As the transition frequency deviates from resonance with the laser, the Bloch vector begins to precesses at the difference in frequencies either advancing it clockwise or anticlockwise about the equator. This phase evolution gives rise to Ramsey fringes due to the effect of the second pulse, this time in the frequency domain. Measuring in the frequency domain has the added benefit that one need not worry about the possibility that the laser is not perfectly tuned to the transition since the transition is swept through resonance. In these spectra, a line shape is observed peaking when on resonance with the laser. The width of that peak is limited by the Fourier transform of the micropulse time profile when the pulses are shorter than T_2^*. Within this line shape are oscillations due to the Ramsey interference. The periodicity of these oscillations is now related to the pulse delay instead of a property of the two-level atom. By using this method, multiple spectra can be taken for a few different steps in delay to assess the rate at which the Ramsey fringes decay in time.

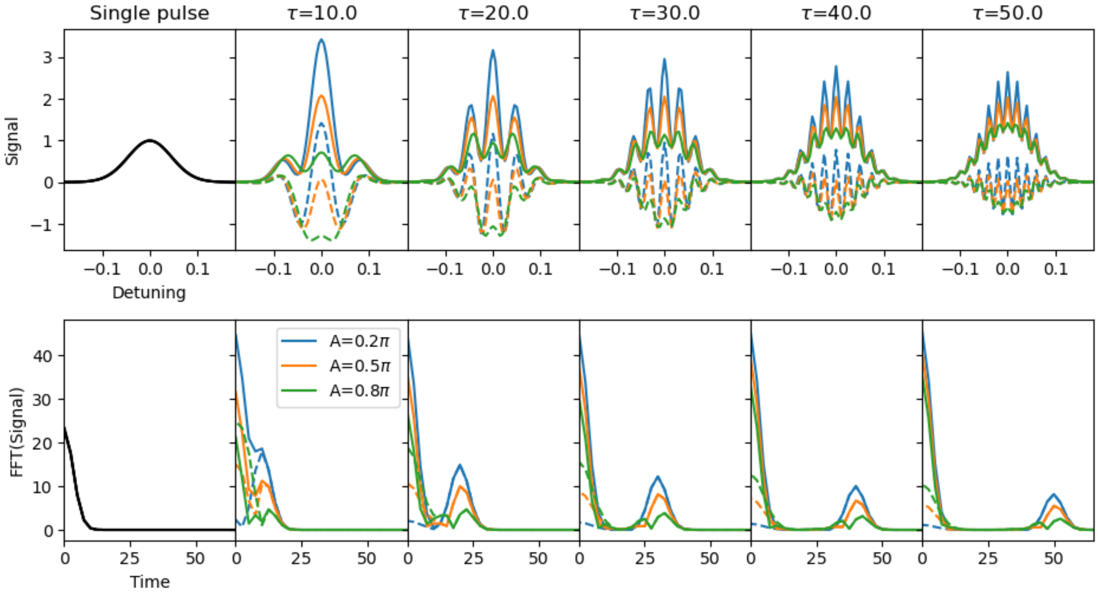

Figure 4.5: Modelled Ramsey spectroscopy detected by PTIS for different pulse areas and delay configurations. All two pulse spectra are normalised to the hight of the single pulse spectrum. Spectra drawn with dashed lines indicate that twice the single pulse spectrum has also been subtracted from the two pulse spectrum. With small pulse areas (blue lines), the high frequency peaks in the Fourier transforms are stronger at small delay than the same peak at large pulse area making it easy to observe decay with delay. There is comparatively smaller absolute change in the DC signal with delay when the pulse areas are small. At larger pulse areas this is different, the peak at DC changes height with delay relatively more than the peak at high frequency making the decay of the DC peak more apparent. The pulse area does not change the decay rate but will affect the ability to observe the two decay rates in the Fourier transforms.

Examples of modelled detuning scans are shown in fig. 4.5. In these modelled spectra, the two level system has a T_2^* time of 50 ps which is made with equal parts pure dephasing and dephasing due to relaxation ($\Gamma = \gamma_{21}/2 = 0.01\,\mathrm{ps}^{-1}$). In this case no inhomogeneous broadening was included ($W = 0$). The detuning spectrum for only a single light pulse is smooth with a maximum when the transition is resonant with the light as expected. With the inclusion of a second pulse of light, Ramsey fringes appear which decay with increasing delay. When the delay is so long that the atomic state has fully relaxed in the time between the pulses, the second pulse promotes the same number of electrons into the conduction band (provided the pulse areas are small and few electrons leak out). This means the final conduction band density is simply double that after the first and the two pulse spectrum approaches twice that of the one pulse spectrum for long delays. It is therefore useful to subtract double the single pulse spectrum from each two pulse spectra such that any remaining signal is due only to non-linear effects caused by retained phase or ionisation of the atom. The magnitude of the Fourier transforms of the modelled spectra in fig. 4.5 show that the amplitude of high frequency Ramsey fringes is not lost in this subtraction. There is only an amplitude offset in DC components causing a decay from a finite amplitude to zero as opposed to a finite value towards twice the DC component of the single pulse spectra.

The amplitude of both principle components of the Fourier transformed, subtracted signals when viewed as a function of delay show exponential decay. The time constant of these two decays (gradients in fig. 4.6) match with the input relaxation and pure dephasing terms: $T_1 = 50\,\mathrm{ps}$ and $T_2 = 100\,\mathrm{ps}$. These time constants are not dependent on pulse area, as they shouldn't be since these are properties of the two-level system. The initial amplitude of these components at zero delay however does depend on pulse area. From fig. 4.6 it is clear that with different pulse areas the initial amplitude of DC and high frequency components change. With small pulse areas decay in the high frequency component will be easier to observe than for that in the DC one. The error in a measured T_2^* relative to that for T_1 for small pulse areas is expected to be smaller. This statement is then swapped around

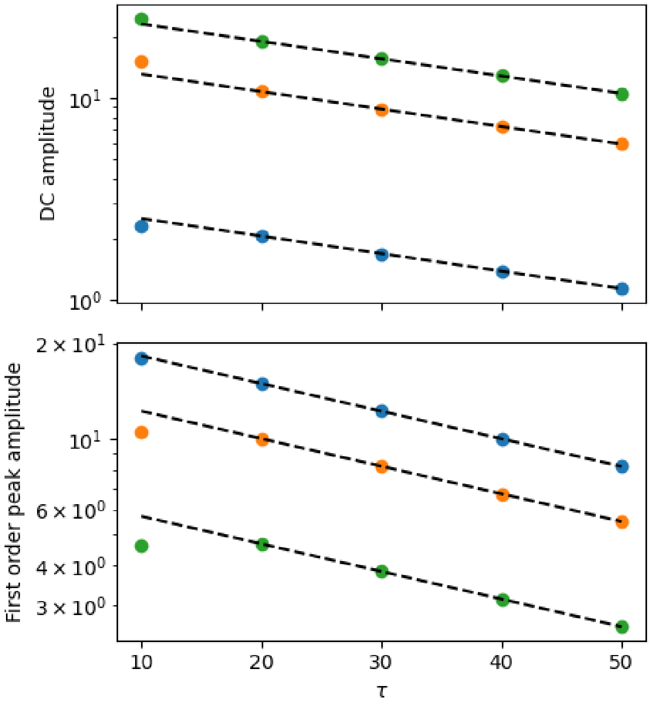

Figure 4.6: Modelled intensity decrease of the principle components of frequencies present in PTIS detected Ramsey spectroscopy. Dashed lines are guides to the eye with simple exponential decays demonstrating constant $1/T_1$ in the case of the DC peak and $1/T_2^*$ decay rate in the case of the finite frequency peak, independent of pulse area.

for large pulse areas where the error in fit T_1 is expected to be smaller.

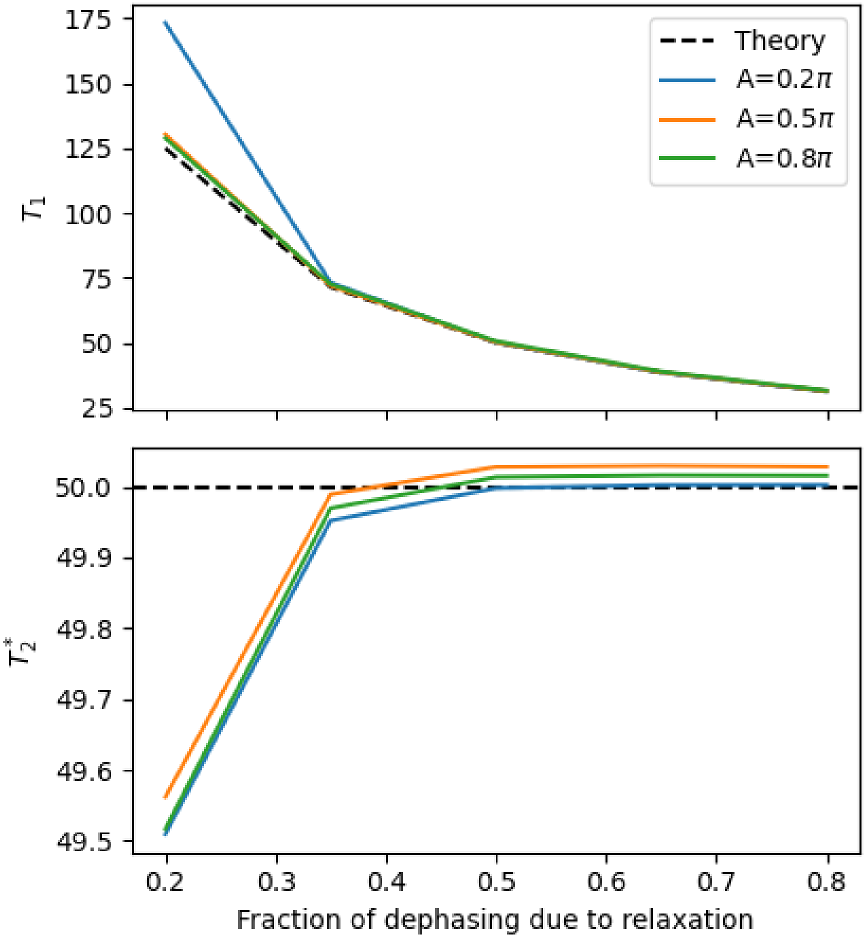

Figure 4.7: Deviation of the fitted decoherence times from known input. Accurate fit to T_2^* when relaxation is a lot less important than dephasing is difficult regardless of pulse area. Fitting to T_1 seems only difficult in the similar situation when the pulse area is low. When γ_{21} is small numerical error in T_2^2 for reasons postulated in the text.

The systematic error in the extracted T_1 and T_2^* is determined by fitting an exponential to the Fourier transform peak amplitudes in fig. 4.6 and comparing the decay constant to the input decoherence times. These times are plotted for each of the three pulse areas in fig. 4.7 as a function of the fraction of total dephasing due to relaxation. This figure shows that for small pulse areas and low rate of relaxation relative to pure dephasing, T_1 is overestimated using this method. Under these circumstances, the number of electrons promoted into the conduction band by the second pulse regardless of delay is always very close to double that after the first so the DC component of the FT starts close to zero and stays close to zero with increasing delay. The time constant of the exponential decay that describes this trend could then be a wide range of values and still achieve a good fit. In contrast all of the fit T_2^* times in this example where within 1 % of the actual value. A small deviation exists regardless of pulse area when γ_{21} is small. This deviation is an artefact from the computation of the conduction band population at the end of the pulse sequence. It is assumed that the rate of thermal ionisation from the excited state is much slower than the rate of relaxation. When γ_{21} is small the system has not fully relaxed by the time a maximum time limit is reached in the computation and the pulse sequence is stopped before the system has reached equilibrium via via thermal ionisation or relaxation.

4.2.2 Tuning donor orbital states with a magnetic field

Two methods have been used to implement uniform detuning of the orbital states of all donors in a silicon sample. One of which is to apply a uniaxial stress to the crystal. [58,59]. The other one that is used in this experiment is with a static magnetic field via the Zeeman effect. [60]. To obtain the following experimental data in this chapter, a tunable 33 T bitter magnet at the high field magnet laboratory (HFML) facility was used in conjunction with the neighbouring FELIX facility to detune and excite the resonant frequency transitions of interest at various magnetic field values.

The Zeeman effect splits and shifts donor orbital states in a way that is analogous to the Zeeman effect in atomic hydrogen. [61] Atomic states with non-zero magnetic quantum numbers $m_l \neq 0$ have a non-zero magnetic moments causing loss of degeneracy when interacting with an external magnetic field. The external magnetic field perturbs the atomic Hamiltonian for these states shifting them with an energy proportional to the field magnitude and in a direction dictated by the sign of

m_l. The Si:P $2p_{\pm}$ state splits into the $2p_{-}$ state which becomes more tightly bound and the $2p_{+}$ which becomes less tightly bound.

Fourier transform infrared (FTIR) spectroscopy of Si:P under external magnetic field in the 0 T to 30 T range has been published previously [60] and plotted with permission in fig. 4.8. In that experiment, incoherent, broadband light illuminated along the [100] direction of the sample in the Faraday geometry (external magnetic field parallel to the light's Poynting vector). Absorption was measured by a liquid helium cooled Si-composite bolometer down-stream of the sample. Since the light source in that experiment was continuous wave, the line widths measured are limited by T_2^* and not the limited bandwidth of a pulsed source however, it is impossible to separate the total dephasing measurement into relaxation, pure dephasing and inhomogeneous dephasing times.

Instead of measuring absorption through the sample, where expected signal to noise would be low due to the dilute doping density, here orbital transitions are measured electrically using PTIS. This mechanism has some important distinctions to absorption spectroscopy that must be considered:

- A higher lattice temperature must be used such that thermal excitation out of the excited state is possible.
- The energy of the excited state shifts with magnetic field so the probability of thermal ionisation varies throughout a detuning scan.
- The position of the conduction band edge also changes with increasing magnetic field due to the cyclotron energy, $B\hbar e/m^*$.

The second two of these conditions are important to be able to define a field dependent relative thermal ionisation rate with which to normalise collected spectra of particular transitions. The theoretical positions of the orbital transitions [60] are plotted in fig. 4.8. These, along with the shift in the conduction band edge by the cyclotron energy define an amended ionisation energy of the excited state. Using

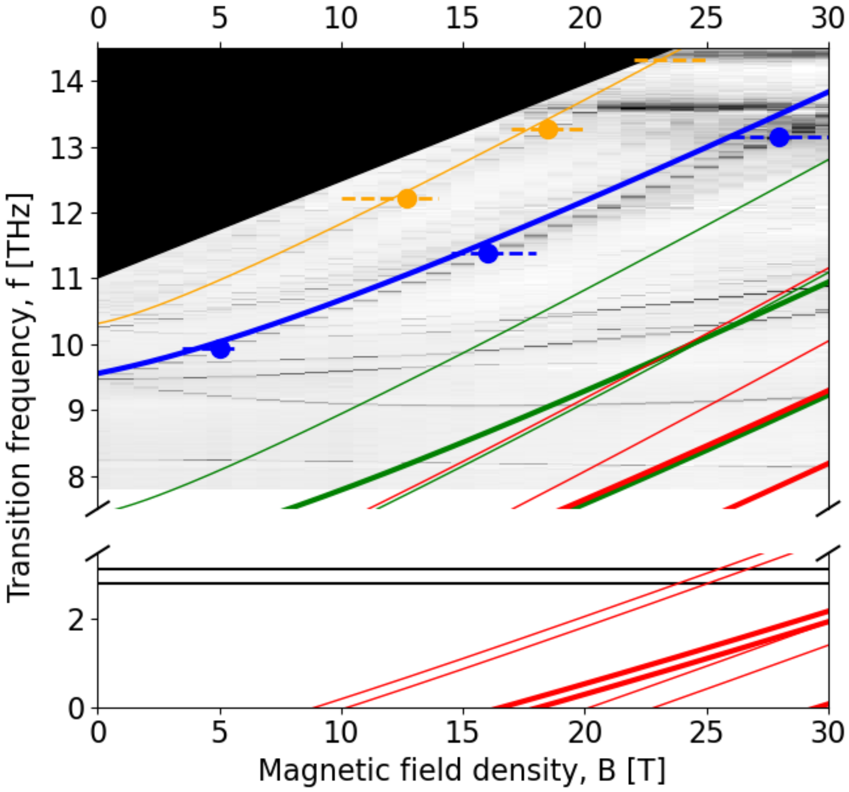

Figure 4.8: The grey-scale heat-map is of published [60] absorption FTIR data of Si:P orbital transitions over a wide field range. The green and orange curves show the theoretical spectral positions of the $1s(A_1) \rightarrow 2p_+$ and $1s(A_1) \rightarrow 3p_+$ transitions also published in the same article. The black area depicts transitions into the conduction band from the ground state. Dashed lines and dots mark the 6 field sweep locations and the position of observed peaks in this work. The green and red lines depict the $1s(A_1) \rightarrow 2p_+\&3p_+$ transitions offset by the frequency of g (green) and f (red) intravalley phonons. These phonons can relax the excited electron into other orbitals with the same valley components.

eq. (2.3) the relative change in PTIS signal intensity from that at zero field is plotted in fig. 4.8 for the $2p_+$ and $3p_+$ transitions.

The PTIS intensities of the $2p_+$ and $3p_+$ excited states are expected to vary by orders of magnitude over the entire 0 T to 30 T magnetic field range due to the changes in binding energy of those states. Over the small magnetic field ranges used to observe individual transitions around a particular laser frequencies the variation in binding energy of the excited state is expected to be small. The expected relative PTIS strength would vary by a maximum of a factor of 2 at the wavelengths and magnetic field ranges chosen. The binding energy of these excited states vary the least as they shift in energy at a similar rate as the conduction band which shifts with the cyclotron energy [62].

Since PTIS relies on thermal ionisation of the electron the sample must be at elevated (though still cryogenic) temperature. This means there will still be a density of phonons present that may assist the relaxation of excited state orbitals into lower energy states resonantly. In fig. 4.8, additional green and red lines are drawn below the $2p_+$ and $3p_+$ states spaced at the energy of the intravalley g and f-phonons in silicon. Where these lines cross lower energy states (provided similar valley composition in both states) we would expect to see a significant reduction in T_1 provided these phonons are present at this temperature. A thorough empirical investigation of this particular relaxation mechanism as a resonant effect is not explored in this body of work but is mentioned as a potential cause for the observed reduced coherence times at higher magnetic field where there are more lower energy states for the excited state to relax into at energies similar to those of g and f phonons.

4.2.3 THz spectroscopy of Si:P orbital transitions

The temperature of the sample as set up in chapter 2 was fixed at 17 K. This temperature is where the PTIS signal was found to be maximised experimentally for the Si:P $1sA_1$–$2p_\pm$ transition at zero magnetic field with a highly attenuated FEL beam to avoid additional heating with the beam. This temperature was kept constant and not re-optimised for transitions detuned at different magnetic fields ranges.

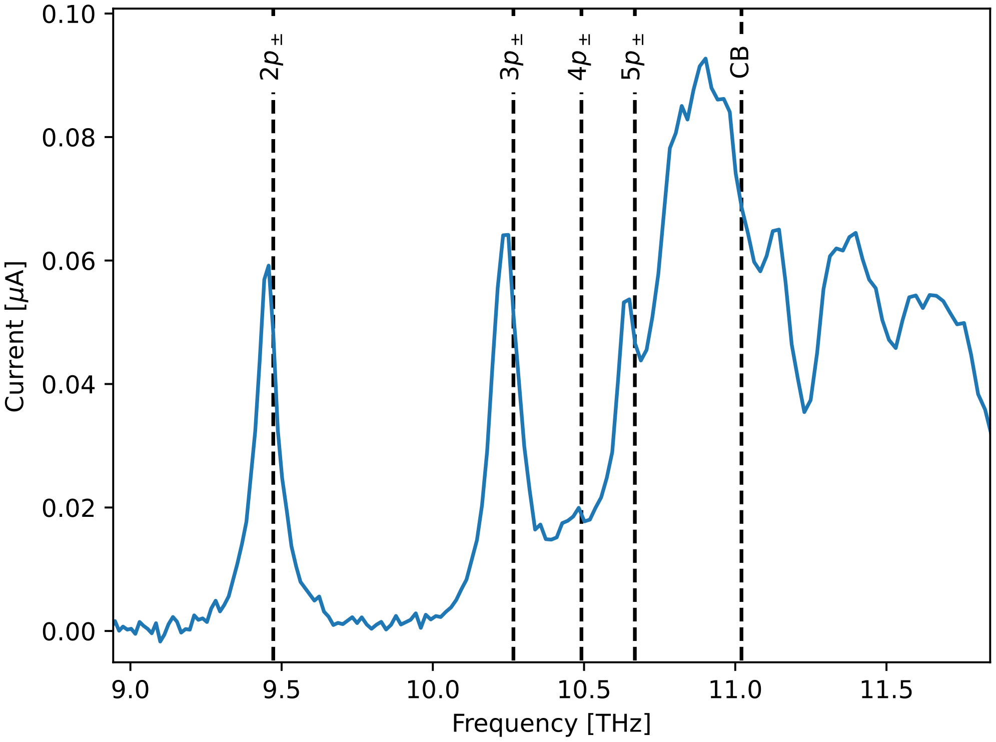

Figure 4.9: PTIS spectrum obtained by sweeping the line centre of FELIX through Si:P orbital resonances at zero magnetic field.

fig. 4.9 shows a one pulse spectrum at zero-field obtained by scanning the FEL undulator wavelength and logging the transient photocurrent that passes through the capacitor stack upon illumination. Orbital transitions up to the $5p_\pm$ are clearly resolved at their expected frequencies for isolated phosphorus donors. [63] An offset is observed between the measured peaks and their expected positions. This is likely due to a latency in the movement of the undulator magnets when their spacing is scanned. The set wavelength is swept at a constant rate and an observed offset of $0.3\,\mu$m was seen that was constant over the wavelength range scanned over. As well as resonant increases in photo-signal, resonant reductions are observed at particular wavelengths, particular present in the conduction band in fig. 4.9. These are due to resonant absorption of the light by atmospheric water vapour [64] modulating the power of FEL light reaching the sample. These are present because the space between the FELIX beam line exit and the cryostat entrance was open to ambient air. This is of little concern for this experiment as the magnetic field gave flexibility to place the transition of interest at frequencies where water vapour absorption resonances do not exist.

4.2.4 Field dependence of Si:P orbital dynamics

The $1s(A_1) \rightarrow 2p_+$ line shape was detuned to three different resonant frequencies spanning the broad magnetic field range accessible with the bitter magnet. Spectra of these line shapes are plotted in fig. 4.10 for different pulse delays and FEL frequencies. For each three resonant frequencies investigated, detuning spectra were taken for five different pulse configurations: The first, with one of the interferometer arms blocked and then four two-beam spectra with different fixed pulse delays.

Clear Ramsey oscillations appear in all two-pulse spectra whose fringe amplitudes decays with increasing pulse delay. The blue data points in fig. 4.10 show the raw photocurrent signal after being divided by the expected variation in PTIS intensity and then normalised to the peak height of the single pulse spectrum at that frequency. Red data points show the two-pulse spectra with the corresponding single pulse spectrum twice subtracted. The frequency offset of the peak locations from zero detuning arises due to the mismatch between the theoretically predicted Zeeman spectrum from the actual spectrum. This difference is also evident in the FTIR data [60] presented in fig. 4.8.

Gaussian line shapes are fit to the peaks in the Fourier transforms at $t = 0$ and at the time corresponding to the pulse delay in all of the two pulse spectra at a particular FEL frequency. The decay of the peak amplitudes with pulse delay reveals

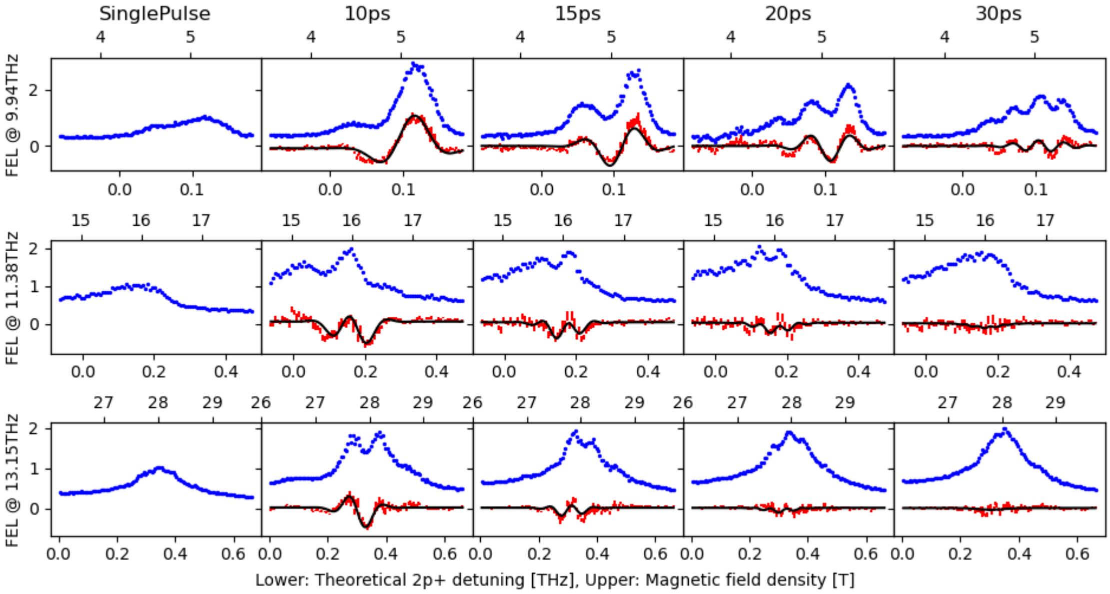

Figure 4.10: Frequency domain Ramsey spectra for the Si:P $1s(A_1) \rightarrow 2p_+$ transition over a broad range in external magnetic field. Blue points mark the photocurrent detected on arrival of the FELIX macropulse divided by the expected PTIS intensity variation due to a change in the excited state binding energy with magnetic field. Red data points are the same spectra after subtracting twice the single pulse spectrum. Black curves are the modelled spectra resulting by fitting to the Fourier transforms of the red subtracted data. In this case no inhomogeneous broadening was included and all pure dephasing mechanisms were controlled by Γ.

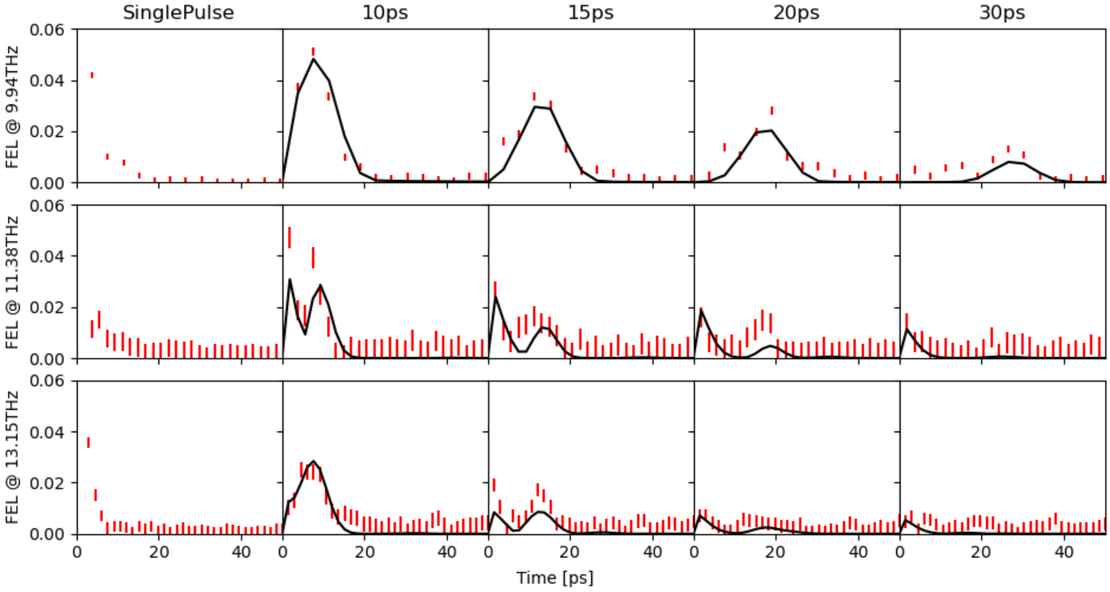

Figure 4.11: Fourier transform magnitude of the subtracted spectra in fig. 4.10 (red points) and that of the model fit (black curve).

the transition's coherent dynamics. The width of Gaussian used for each particular laser frequency was fixed to the micropulse duration as determined by the inverse of the measured FEL spectral linewidth. The location of the fitted Gaussian was also fixed to the set time delay of the two pulses in each particular configuration.

Laser freq. [THz]	9.94	11.38	11.15
Field range [T]	4.5-5.5	15-17	27-29
w [ps]	6.96	4.11	4.59
A [π]	0.002(*)	0.38	0.20
T_1 [ps]	8.7 ± 5.8	31.1 ± 28.5	9.3 ± 7.3
T_2^* [ps]	14.32 ± 0.95	9.8 ± 1.8	8.5 ± 1.1

Table 4.1: Decoherence times for the $1s(A_1) \rightarrow 2p_+$ inferred from fits to the detuning spectra's Fourier transforms. The fixed micropulse lengths, w and pulse area, A are also shown. The four delay times and deviation from zero detuning are not tabulated here but are shown to give good fit as seen in fig. 4.11. Only homogeneous decoherence mechanisms were fit in this optimisation.

The errors in the fit decoherence terms were extracted from the covariance matrix evaluated at the optimum T_1 and T_s^* values. The total dephasing time, T_2^* decreases significantly when the transition is detuned from its resonance at 5 T to that at 16 T. For each three field ranges the amount of attenuation in the beam was kept constant using 38 dB nutral density filters. Therefore, the sudden change in pulse area tuning the transition from 9.94 THz to 11.38 THz is surprising. From the spectra it is clear that the pulse area at 5 T is much lower than a π-pulse due to the greater than $2\times$ increase in signal when changing from a one pulse configuration to two (closely separated) pulses when the second pulse constructively interferes with the evolving atom. There are two strong water absorption lines near this frequency [64] one at 9.83 THz and the other at 10.05 THz. Given the laser line width of 0.1 THz to 0.2 THz it is possible that air could be absorbing in this small window. It is therefore expected that a good measurement of T_1 may not be possible at this frequency.

The relaxation time, T_1 is difficult to extract from this dataset with high precision as evidenced by the large errors in the values deemed to optimise the fits. A low DC peak signal is predicted when the pulse areas are exceedingly small as shown in fig. 4.6 and this is likely the reason for the poor signal to noise in this range of the spectra's Fourier transforms. On the other hand, at low pulse area, T_2^* is expected to be easier to measure due to large relative difference in signal between the peaks and valleys of the Ramsey fringes. T_2^* however quite clearly decreases from 14 ps to 10 ps from 5 T to 16 T and again to 9 ps at 28 T.

Results for T_2^* were checked by comparing their values found with magnetic field scans, to those found by fitting to the more conventional yet slower to acquire, delay scans at different fixed magnetic fields. The values for T_2^* measured in fig. 4.12 for the

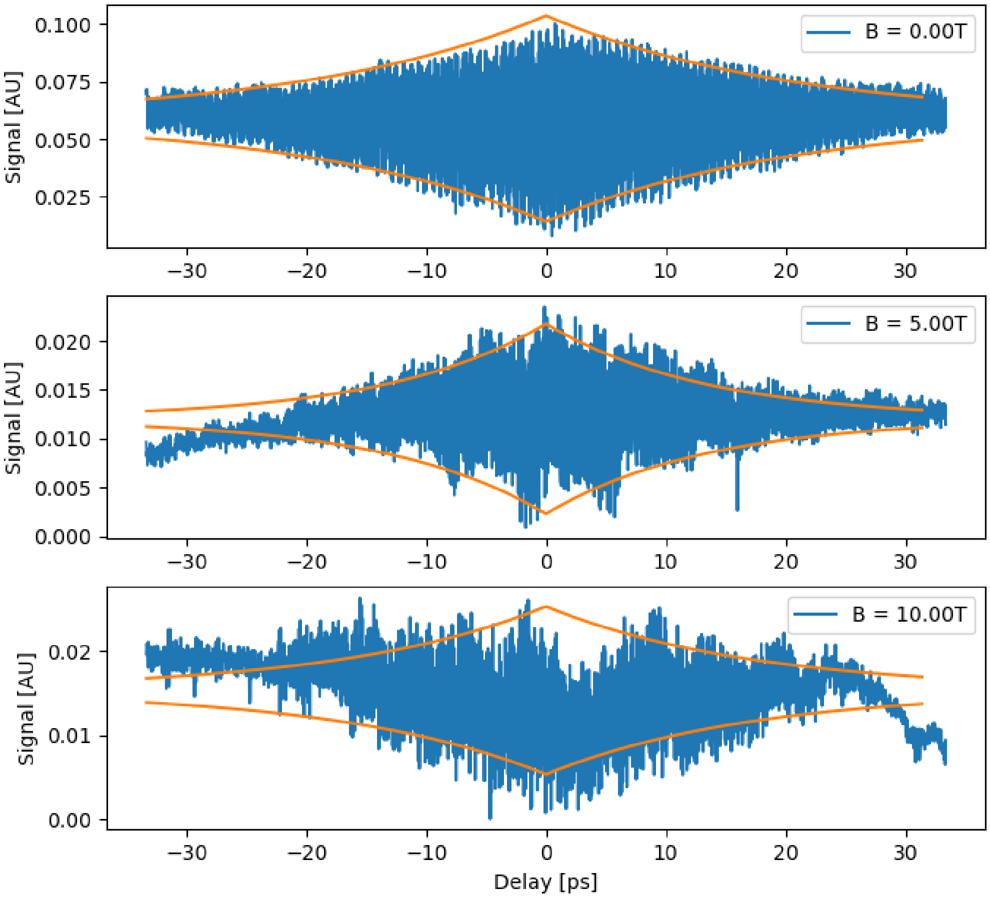

Figure 4.12: On-resonant, two pulse delay scans of the $1s(A_1) \rightarrow 2p_+$ transition at three different magnetic fields. The fit T_2^* for each in increasing magnetic field are: (20.16 ± 0.06) ps, (13.23 ± 0.06) ps and (17.2 ± 0.2) ps

$2p_+$ transition at 0, 5, and 10 T are of comparable order to those measured by fitting to the Fourier transforms of the frequency domain spectra. Slow undulations are visible in the delay scans that indicate aliasing is present. There is also asymmetry in the envelope shape that could be due to a drift in the FEL power or wavelength over time.

Similar spectra were also taken of the $1s(A_1) \rightarrow 3p_+$ transition with spectra shown in fig. 4.13. Ramsey fringes were observed in all but the highest magnetic field range. At this high a magnetic field, the $3p_+$ excited state begins to merge with the conduction band. Light at this wavelength simply photo-ionises the ground state and flat spectral response in this magnetic field range is to be expected.

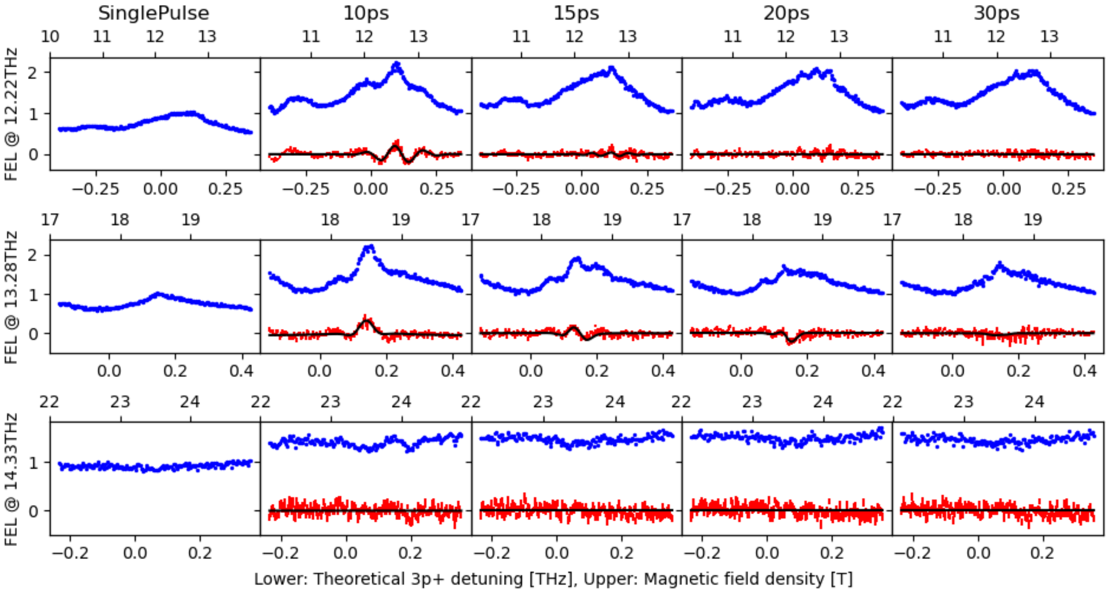

Figure 4.13: Spectra of the $1s(A_1) \rightarrow 3p_\pm$ transition tuned to three frequencies in different magnetic field ranges. No transition is seen in at the highest field here as the excited state has merged with the conduction band and the THz light simply photoionises the ground state directly.

The total decoherence times, T_2^* range between 3.68 ps to 14.3 ps. These times are comparable to the duration of individual FELIX micropulses in this wavelength range. This is undesirable in terms of signal to noise. A $\pi/2$-pulse exciting the state over a long period whereby the state loses significant coherence during the time the pulse is acting on the state means that the Bloch vector will not end up close to the

Laser freq. [THz]	12.22	13.28	14.33
Field range [T]	11.5-13.5	18-19	22-25
w [ps]	2.99	9.37	-
A [π]	0.269	0.494	-
T_1 [ps]	23.7 ± 2.7	-	-
T_2^* [ps]	14.5 ± 18	11.7 ± 1.4	-

Table 4.2: Decoherence times for the $1s(A_1) \rightarrow 3p_+$ not including dephasing due to inhomogeneous broadening. No resonance is seen in the highest field range here due to the excited state overlapping with the conduction band.

equator when the light is off.

Previous measurements of donor orbital dynamics [65] showed that the higher orbital states have longer T_1 times >150 ps for the $3p_\pm$ and $4p_\pm$ but whose T_2^* coherence times become increasingly limited by inhomogeneous broadening rather. The comparison done in that publication of pump-probe measurements to determine T_1 and FTIR to determine T_2^* showed that all of the dephasing occurring on the $2p_\pm$ state can be explained by the dephasing caused by relaxation. There is no reason to expect additional pure dephasing effects. The larger orbitals experience more of their surrounding environment so larger variation can occur in the binding energy of these states for an ensemble of donors. For a single defect it wouldn't make sense to talk about inhomogeneous broadening so the total dephasing times measured for a single donor would only be limited by T_1 effects which are shown to be longer lived.

4.3 Conclusions

In this chapter the background theory for coherent light matter interaction relevant for Ramsey spectroscopy of a two level system is introduced. An amendment is made to the optical Bloch equations to allow for photo-thermal ionisation of the donor orbital. The expected time and frequency domain Ramsey fringe signals are modelled and it is demonstrated how one may extract both relaxation and dephasing effects from frequency domain Ramsey spectra.

The Si:P $1s(A_1) \rightarrow 2p+/3p_+$ transitions are measured over a large magnetic field range in a two-pulse Ramsey PTIS set-up. The magnetic field allows the transition energy to be detuned in order to produce frequency domain Ramsey fringes. The high field range of the bitter magnet made it possible to investigate the orbital dynamics of these transitions in extreme magnetic field conditions where previously, coherent dynamics information was unknown.

The significant decrease in measured coherence times in this experiment compared to those measured previously is likely due to the higher sample temperature used to maximise signal for the PTIS ionisation mechanism to work effectively. In the next chapter another electrical readout mechanism is introduced that could make measurements of orbital coherence times at temperature much lower than those required for PTIS possible.

Chapter 5

Orbital transitions in a Bi impanted SOI device

The orbital states of donor qubits in silicon have been studied extensively, predominantly via absorption Fourier transform infrared (FTIR) spectroscopy. Samples studied are typically wafers of bulk float zone (FZ) silicon crystal with a residual, dilute concentration of the dopant species of interest in the crystal bulk. This method of doping provides a very pure, undamaged crystalline environment for the substitutional dopants resulting in sharp spectral features.

To be able to measure the absorption spectra of the frozen-out donors optically a large enough density of dopants must be illuminated to achieve a significant change in light intensity transmitted through the sample. For samples whereby sensitivity to the orbital change of single atoms is desired this presents a significant hurdle and a move towards electrical detection is required. This chapter presents results of performing ionisation spectroscopy on a broad area ion implanted Si:Bi device containing fewer than 10^6 donors in the optically active region. Evidence for shallow level impact ionisation is observed and the potential for its use as an alternative to photo-thermal ionisation spectroscopy (PTIS) for excited state ionisation mechanism is explored.

5.1 Sample preparation

The sample studied in this chapter was fabricated using high resistivity silicon-on-insulator (SOI) wafer prepared by the 'Smart Cut' method [66]. The advantage SOI has over bulk silicon with regards to electrical detection of orbital transitions is that in SOI current can not pass through the substrate handle. By forcing current to pass through a particular region where few donors can exist, background currents are suppressed improving signal to noise. The SOI wafer used in this study has a 450 nm thick device layer sitting on top of a 1 µm thick SiO_2 buried oxide (BOX) insulating the device from the handle. Both the device and handle silicon in this material had a dilute background p-type (most likely boron) concentration of $10^{12}\,\mathrm{cm}^{-3}$.

The pristine wafer began by being ion implanted with bismuth to form a 100 nm thick layer of n-type dopants starting 50 nm below the surface with a peak concentration of $10^{17}\,\mathrm{cm}^{-3}$ as shown in fig. 5.2. Such a high donor density was chosen due to the limited literature presenting successful annealing of implanted bismuth in silicon. to activate implanted bismuth at this energy in a SOI substrate.

To achieve a bismuth doped layer this thick with a flat-top concentration profile so close to the surface, a series of two different implant energies was required: one at 800 keV and another at 400 keV. To incorporate the implanted bismuth as substitutional defects, an rapid thermal anneal (RTA) was performed. Previous studies of bismuth implanted into bulk silicon [54] gave an indication of the optimum annealing conditions. To confirm the effectiveness of prior annealing recipes, a small variety of annealing temperatures were tested. The one with highest electrical activation was used for the sample studied in this chapter. To determine the active concentration, spreading resistance analysis (SRA) was done by an external company (SOLECON ltd.) capable of polishing the required shallow bevel angle and perform four-point probe resistivity measurements along the resulting slope with high resolution. Details of this technique are outlined in chapter 2

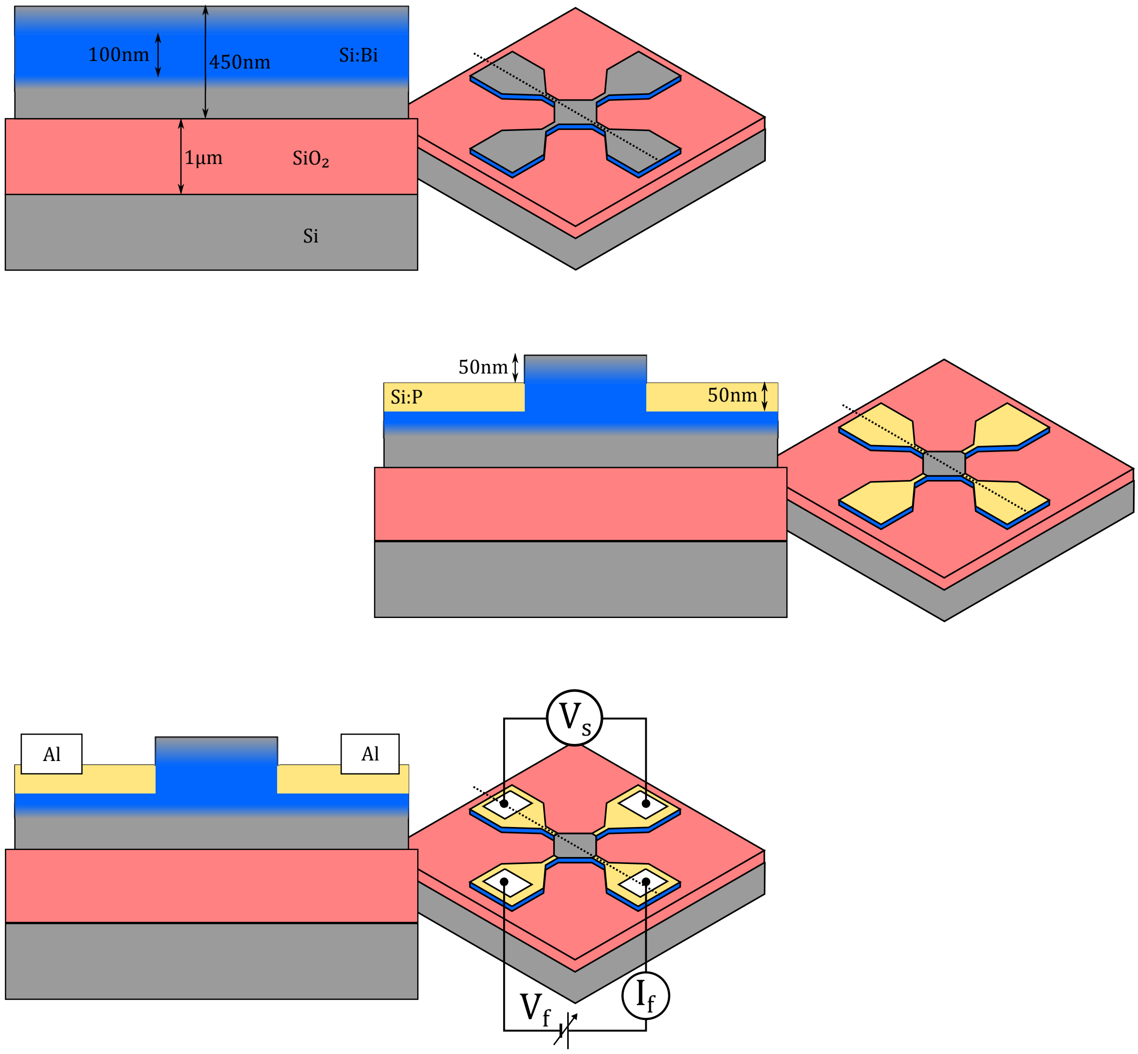

Figure 5.1: Fabrication scheme for VdP devices starting from SOI implanted with bismuth and annealed. 1) RIE to define isolated mesas. 2) RIE followed by phosphorus ion implant and anneal to define metallic leads. 3) RIE followed by aluminium evaporation and forming for ohmic contacts that remain metallic at liquid helium temperatures.

From annealed implanted wafer, standard UV-photolithography techniques were used to etch four-terminal, Van der Pauw (VdP) mesas into the SOI device layer. The leads were then selectively etched and doped with a low energy, high dose phosphorus implant. Heavily n-type leads close to the surface and within the Bi layer have the effect of reducing the width of the metal-semiconductor Schottky barrier that forms at the aluminium contacts and minimising the potential barrier between the n^+n interface. Electrical activation of the heavily doped leads was achieved by another RTA. To contact the device, aluminium pads were deposited via e-beam evaporation and subsequently heat treated in a dry nitrogen atmosphere at 300 °C for 45 min on a hotplate. This long heat treatment in an inert atmosphere causes the aluminium to 'spike' into the Si:P lead while preventing oxidation. For a graphical outline of the fabrication process and sample geometry see fig. 5.1.

5.1.1 Spreading resistance profiling

SRA (as outlined in chapter 2) shown in fig. 5.2 revealed that the electrical activation of the bismuth in this sample was 65 % after being annealed at 950 °C for 1 min. This yield was calculated by integrating the SRA concentration in depth ($1.01\times10^{12}\,\mathrm{cm}^{-2}$) and comparing that to the requested implant dose ($1.55 \times 10^{12}\,\mathrm{cm}^{-2}$). The peak concentration activation yield was also calculated to be 62 % by comparing the peak concentration in the SRA data to a Monte-Carlo simulation of the implant using the software package stopping and range of ions in matter (SRIM). SRIM was used to determine the target dose to achieve the desired peak concentration for the implant energy. The difference in these two activation yields shows that diffusion of the bismuth has occurred.

The SRA shows that a preferential diffusion of the implanted bismuth towards the surface has happened. This is to be expected as most of the lattice damage caused by the high energy implant will be located nearer to the substrate surface. During annealing, bismuth undergoes vacancy enhanced diffusion as the dominant

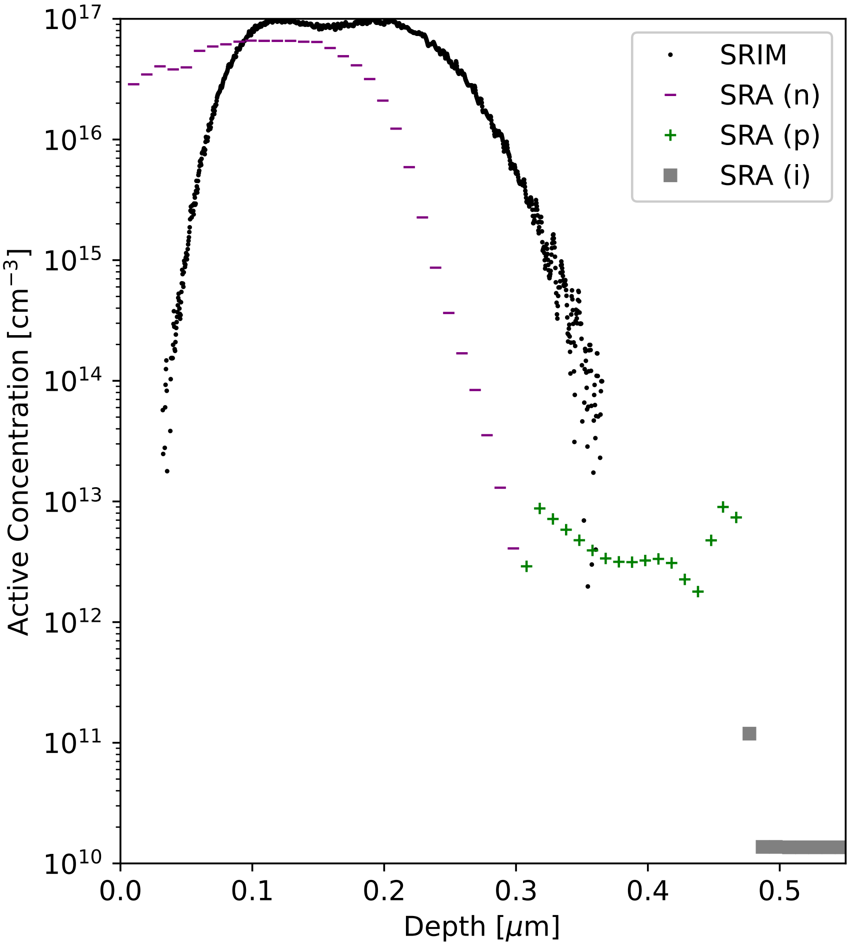

Figure 5.2: Spreading resistance analysis of the annealed bismuth implant along with the expected distribution prior to annealing modelled using SRIM. The junction between the majority n-type bismuth doped region and the p-type background is visible along with the insulating BOX of the SOI substrate.

diffusion mechanism in silicon. [67] Diffusion deeper into the bulk of the SOI device layer is not a problem for this sample as here the donors become more isolated and their orbital spectra remain sharp. Diffusion toward the surface achieves this drop in concentration too however, proximity to the silicon surface will affect its orbital binding energy introducing inhomogeneous broadening. Lattice inhomogeneities close to the surface due to residual damage post anneal will also contribute to this broadening.

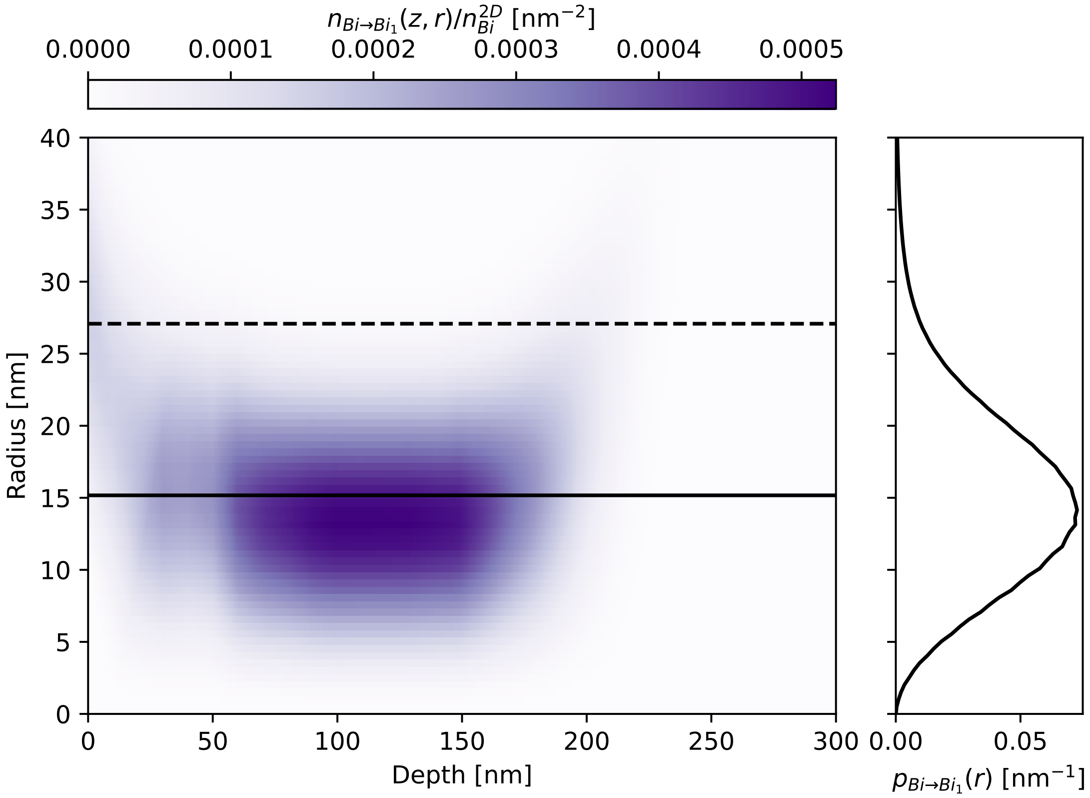

Figure 5.3: The nearest neighbour density surface (NNDS) for the implanted bismuth calculated from the active concentration profile given by SRA. The expected Bi-Bi separation for the total distribution is marked by the solid black line along with the minimum separation required for non-overlapping $2p_{\pm}$ excited orbital states shown by the dashed black line.

Using the donor concentration profile, the NNDS as defined in chapter 3 can be computed. Previously the NNDS was calculated analytically for Gaussian concentration profiles in depth. Here we have a donor concentration profile sampled at discrete depths so numerically compute the required integrals and derivatives in eq. (3.10). The NNDS for this implant is shown in fig. 5.3. To achieve the resolution in the donor separation axis, interpolation of the concentration profile was required. On this plot, the overall expected bismuth separation is shown as a solid horizontal line. Also shown is a dashed line at the separation below which $2p_{\pm}$ orbitals start overlapping. The radial extent of a donor $2p_{\pm}$ state in silicon is 13.54 nm [68] however this state is not spherically symmetric (the same reference calculates the transverse and longitudinal radii as 9.18 nm and 3.85 nm such that $r = \sqrt{2(9.18^2) + 3.85}$). The severity of wave function overlap can be expected to increase between donor separations 27.08 nm to 7.7 nm and the distribution of bismuth donor separations in this sample spans this range.

5.2 DC electrical characterisation

The sample was wire-bonded to a ceramic chip carrier and mounted in a helium gas cryostat with a base temperature of <4.2 K. Two-terminal and four-terminal current-voltage $I - V$ measurements were taken using a Keysight B1500A Semiconductor Device Parameter Analyzer. The optical access windows to the mounted sample could, in this setup, be closed to prevent ambient room light illuminating the sample and ionising the neutral bismuth donors. These shutters were however at room temperature so some black body radiation was still present.

The two terminal measurements taken of this device simply consist of a forced current I_f measured over a range of forced voltages, V_f applied over two adjacent terminals of the VdP structure. The term ‘forced’ is used here to describe a circuit that passes current through the device and to distinguish the ‘sensed’ voltage which describes a voltage drop measured across terminals through which no net current flows. $I_f(V_f)$ was observed to be non-linear indicating that regions in the circuit were not ohmic. The total resistance in this setup is the sum of the resistance of

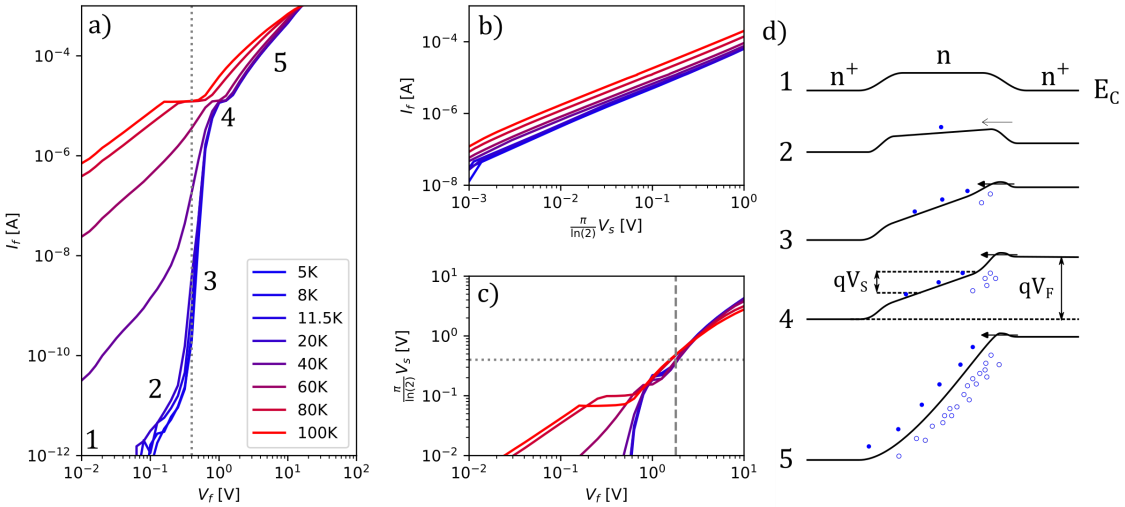

Figure 5.4: a) Two terminal I-V's of the device over a large bias range at different sample temperatures. The onset of impact ionisation of frozen-out bismuth at the injecting contact is seen at $V_f = 400\,\text{mV}$ (dotted line). b) Four terminal I-V curves measured in the VdP geometry show that the sensed voltage remains approximately linear with forced current over the majority of the current range measured. Deviation from linearity is seen at low temperatures for sensed voltages greater than 400 mV. c) At force voltages above 1.8 V (dashed line) the potential drop in the bulk of the channel becomes greater than 400 mV, enough for impact ionisation to occur away from the injecting contact. d) A series of sketches depicting the change in the conduction band edge profile between the forcing contacts for increasing force bias with numbering corresponding to labels in panel a): 1, no current flows and a potential barrier exists at the lead/channel interface; 2, a small current is limited by the number of electrons hot enough to pass over the barrier or tunnel through it; 3, critical bias for impact ionisation of shallow donors near the injecting contact. Space charge is formed and a higher current can tunnel into the channel; 4, injected current saturates due to the limited density of neutral channel donors close to the contact; 5, current into the channel is space charge limited and Mott-Gurney transport takes over.

the channel and all contact resistances between the channel and the source measure unit (SMU).

$$R = \frac{V_\mathrm{f}}{I_\mathrm{f}} = R_\mathrm{ch} + 2R_{n^+n} + 2R_{n^+\mathrm{Al}} \tag{5.1}$$

where the contact resistance between the heavily doped phosphorus leads and aluminium contact pads, $R_{n^+\mathrm{Al}}$ is minimised even at low temperature due to the highly doped leads; any potential barrier resulting from a difference between the metal work function and semiconductor electron affinity will be extremely thin. The most likely source of non-linearity is between the heavily n-type leads and the dilutely doped channel. At temperatures below 60 K a sharp decrease in current is observed at low bias due to the freeze-out of bismuth donors in the device channel. Above a critical threshold bias of 400 mV a sharp onset of current flows indicative of shallow level impact ionisation whereby donor electrons bound to bismuth nuclei can be ionised by free carriers with enough kinetic energy. For all temperatures measured in fig. 5.4 a plateau is reached in current before Mott Gurney transport takes over. This transport regime is made apparent by the $I \propto V^2$ relation followed by $I \propto V$ at very high bias.

For small devices such as this one, relatively low biases are required to achieve the threshold electric field required for impact ionising the donor in any bound state. In order to do electrically detected spectroscopy on the neutral donor, it is important that the ground state is preserved under bias. At the sharp rise in current seen in fig. 5.4 at 400 mV the rate of impact ionisation, A_{ii} of the donors near the injecting contact will have become greater than the thermal recapture rate, B_T of free electrons.

$$\frac{\mathrm{d}N_D^+}{\mathrm{d}t} = nA_{ii}N_D^0 - nB_TN_D^+ \tag{5.2}$$

In fig. 5.4 the sample is in the dark, therefore the sharp onset of current at 400 mV must correspond to ionisation of bismuth ground states and not any of the excited orbital states. The semi-empirical electric field dependence of A_{ii} as found in [49] is,

$$A_{ii}(\mathcal{E}) = \sqrt[\frac{3}{2}]{\frac{1}{x}}\sqrt{\frac{2E_i}{m^*}}\sigma_0 I(x)\sqrt{\frac{2}{\pi}} \tag{5.3}$$

where the dummy variable $x = [(\frac{1}{2} + \alpha)\mathcal{E}^2 m^* \mu^2 + k_B T]/E_i$ and,

$$I(x) = \exp\left(-\frac{1}{x}\right)(x^2 + 2x^3) - \exp\left(-\frac{2}{x}\right)(3x^2 + 2x^3) \tag{5.4}$$

are defined for convenience. $\alpha \approx 1$ is a shape factor which describes the contribution of drift kinetic energy relative to lattice temperature to define an effective 'hot' electron temperature, T_e such that $k_B T_e = k_B T + \alpha m^* v_d^2$, and σ_0 is the maximum cross section for impact ionisation of the particular shallow donor state.

To find the threshold for impact ionisation of a particular bound state, the thermal recapture rate, B_T must also be known as a function of electric field. A form for this coefficient is also presented in [49] whereby,

$$B_T = \beta\sqrt{\frac{2}{\pi}}\frac{4\pi}{3}\frac{r_c^3}{\lambda_0}\sqrt{\frac{2kT}{m^*}}y^{-0.5}[1 - \exp(-y)(y + 1)] \tag{5.5}$$

where β is another semi-empirical factor describing the probability of a free carrier trapping event, λ_0 describes a mean free path length, r_c is a critical radius for thermal recapture and,

$$y = \frac{kT}{kT + (\alpha + 0.5)m^*\mu^2\mathcal{E}^2}. \tag{5.6}$$

Here r_c is the Bohr radius of the neutral bismuth ground state and recapture into excited states is neglected.

These two rates, plotted in fig. 5.5 as a function of electric field define the threshold fields required to measure a net current due to impact ionisation of different orbital states of an isolated Si:Bi centre in a device with this particular doping density and lattice temperature.

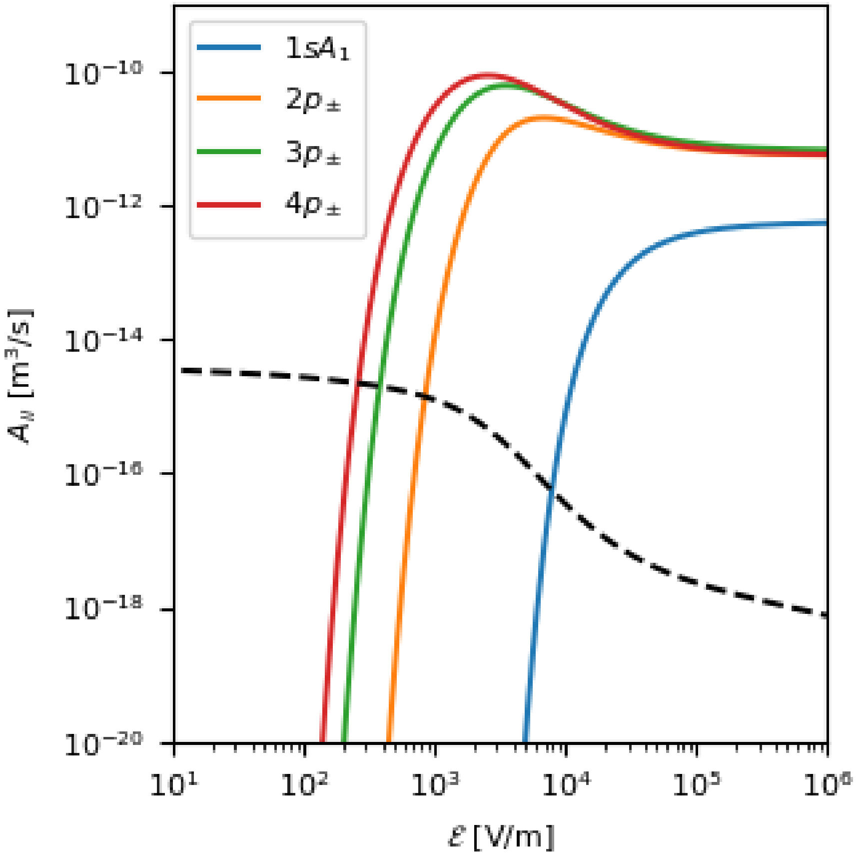

Figure 5.5: Impact ionisation rate as a function of electric field for the ground state and first few $np_{\pm}$ excited states of Si:Bi at 10 K in a device doped to $1 \times 10^{17}\,\text{cm}^{-3}$. The thermal recapture rate under the same conditions is plotted as a dashed line defining critical fields required for impact ionisation to overcome recapture.

5.3 DC characterisation under FEL illumination

The optimum bias conditions were also found empirically. By tuning free electron laser for infrared experiments (FELIX) to the Si:Bi $1sA_1 \rightarrow 2p_\pm$ transition frequency and sweeping V_f using a SRS SIM928 voltage source, the voltage bias resulting in a maximum photocurrent measured with a SR570 is found. For full description of the electrical setup see chapter 2. In fig. 5.6 a photocurrent signal is observed which rises with increasing bias until a maximum signal occurs at $V_f \approx 2\,\mathrm{V}$. Beyond this bias the photo-generated current reduces to 0 A. At such high bias neutral bismuth centres are constantly being impact ionised such that there are very few extra free carriers generated which the FELIX pulse arrives.

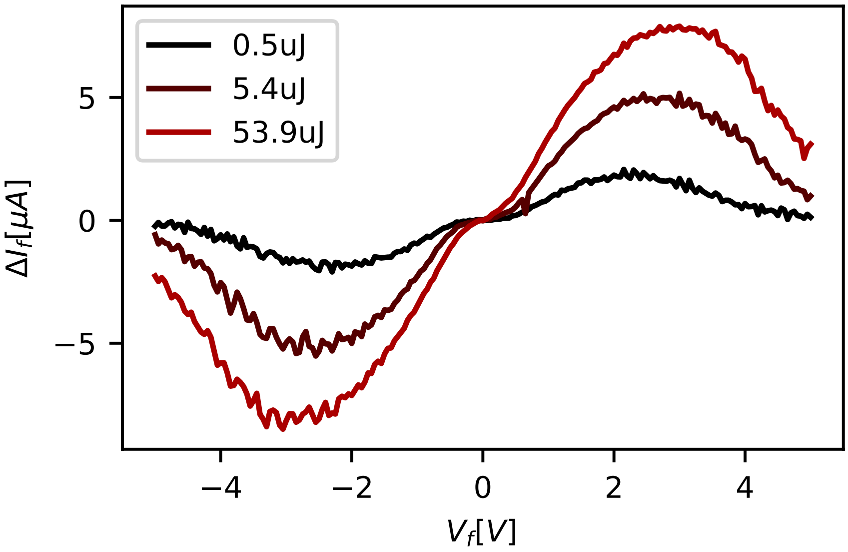

Figure 5.6: Photocurrent as a function of bias while illuminating the device with light at the $1s(A_1) \rightarrow 2p_\pm$ energy (64 meV). The optimum photocurrent occurs at slightly different bias voltage depending on the macropulse intensity.

At a force bias $V_f \approx 2\,\mathrm{V}$ the voltage dropped in the channel is of the order 400 mV as measured in fig. 5.4. For a device with a symmetric four-terminal geometry such as this, this is found by multiplying V_S by the VdP factor, $\pi/\ln(2)$. The electric field at this bias is the expected threshold for impact ionisation of the bismuth donor ground state.

At this high bias (2 V rather than 400 mV), impact ionisation of bismuth donors close to the injecting contact will have taken place and a space charge will have built up at the contact as shown in fig. 5.4. Since this space charge screens the rest of the channel from the force bias, an even large voltage is required to achieve a 400 mV potential in the channel away from the contact.

5.4 FEL spectroscopy

Spectra were taken of the device photocurrent by sweeping the wavelength of FELIX (changing the pole spacing in the undulator) for fixed voltage biases above and below the optimum bias found in fig. 5.6. In all spectra taken, there was negligible change in the measured voltage, V_s between the two other leads as shown in fig. 5.1 only a change in the current, I_{f}. The change in carrier density can then be written as

$$\Delta n = \frac{\Delta\sigma}{q\mu} = \frac{\Delta I}{V_S q\mu}\frac{\ln 2}{\pi} \tag{5.7}$$

The short pulsed structure of the free electron laser (FEL) radiation (5 ps to 10 ps) results in a laser line width of 1 meV which is broad in comparison to the expected orbital transition linewidths in dilutely bulk doped silicon samples [63]. From fig. 5.7 it is evident that at the $1s(A_1) \rightarrow 2p_{\pm}$ resonance the laser line width is narrower than the broad spectral peak. To account for the range of resonators excited at a specific FEL line centre resulting in a change in carrier density, each data point in fig. 5.7 is divided by the FEL full width at half maximum (FWHM), $\Delta(\hbar\omega)$ such that a definite integral of the spectrum gives the number of photo-generated carriers in that spectral range. The FEL line width was determined by the laser spectrum measured concurrently using a grating spectrometer and is shown as an inset in fig. 5.7 at the $1s(A_1) \rightarrow 2p_{\pm}$ energy.

A broadened peak at the $1s(A_1) \rightarrow 2p_{\pm}$ transition energy is observed at both

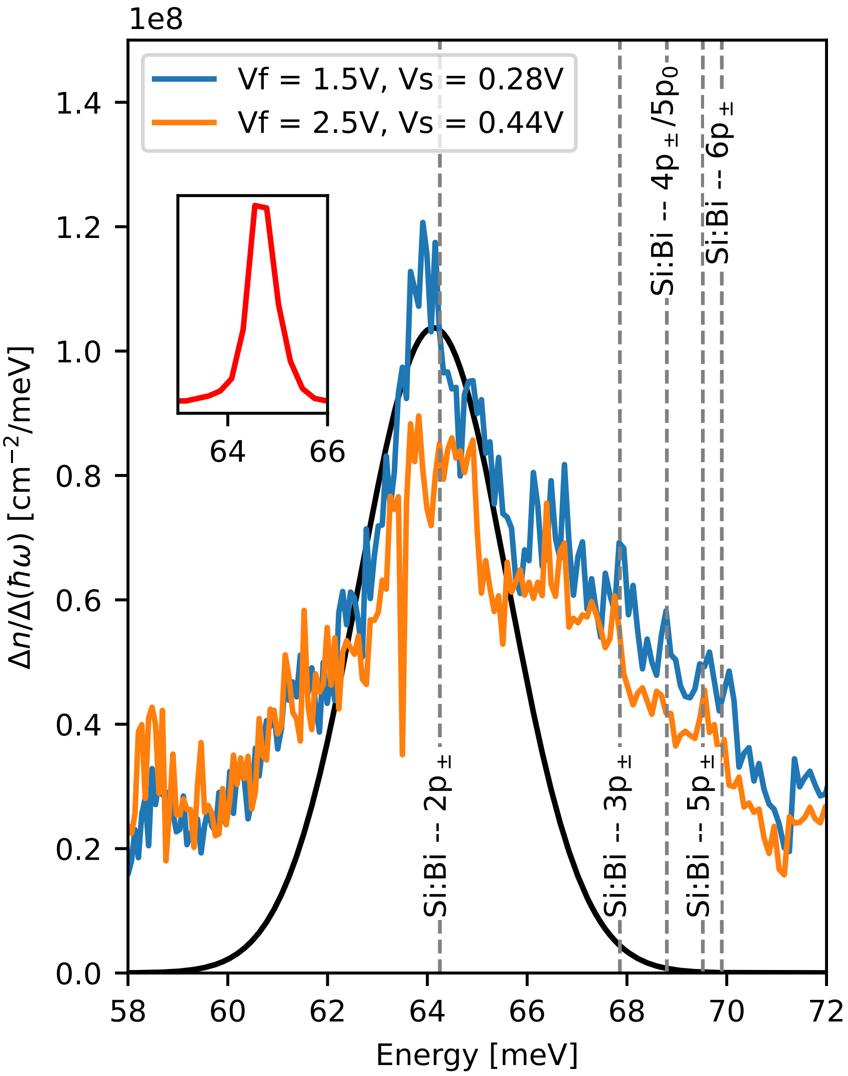

Figure 5.7: The spectral density of photo-excited carriers recorded for macropulse energies of 0.034 μJ and $T = 9.5\,$K. The measured change in carrier density (using eq. (5.7)) is divided by the FWHM of the laser line width, $\Delta(\hbar\omega)$ such that integrating the spectrum in a particular spectral range yields the carrier density contributing to the change in current measured. At bias voltages above 1.5 V the resonant density of photo-carriers is diminished due to an increased rate of impact ionisation of the ground state resulting in fewer neutral donors available to photo-excite. The laser spectrum when tuned on resonance with the $1s(A_1) \rightarrow 2p_{\pm}$ transition is shown as an inset with $\Delta(\hbar\omega) = 0.6\,$meV.

$V_F = 1.5\,\mathrm{V}$ and $V_F = 2.5\,\mathrm{V}$. In both situations the sample temperature was kept at a constant 9.5 K and the FEL macropulse energy, 0.034 mJ by inserting 38 dB of attenuation into the beam. Above the optimum bias, the spectral density of the transition is diminished due to a reduction in available neutral Bi to photo-excite. At 1.5 V bias the resulting photo-generated carrier density is higher. The area under a Gaussian fit to the peak in fig. 5.7 reveals that on average, $4.3 \times 10^8\,\mathrm{cm}^{-3}$ of neutral Bi donors are promoted into the conduction band after being excited into their $2p_\pm$ state. This density amounts to 0.04 % of the available active bismuth concentration.

There was negligible change in the transition line shape when changing the sample temperature below 12 K for this same level of beam attenuation suggesting that PTIS was not the dominant ionisation mechanism out of the excited state in this device. Were it the dominant mechanism an exponential decrease in signal with reducing temperature is to be expected.

With increasing laser power while at low bias, a bleaching of the detected orbital transition was observed as shown in fig. 5.8. These spectra were taken with $V_f = 1\,\mathrm{V}$ where donor ground state impact ionisation is negligible for donors away from the injecting contact. The observed loss of peak contrast indicates that the bismuth donor ground states are being ionised during the laser macropulse. This could be due to heating of the SOI substrate generating phonons capable of thermally ionising the donors directly. It is likely that heat generated by absorption would occur in the heavily doped Si:P leads or in the silicon below the BOX where a larger number of phosphorus or background boron centres are available to absorb.

Though the $1s(A_1) \rightarrow 2p_\pm$ peak is clearly visible in figs. 5.7 and 5.8 it is heavily broadened. The narrowest FWHM measured in this device was 2 meV at low FEL power (suppressing direct ionisation during the laser pulse) and at low bias (below the threshold for ground state impact ionisation). The broadening observed is expected for a high density of implanted bismuth. From the donor separation probability density function in fig. 5.3 an expected Bi-Bi separation of 15.2 nm is

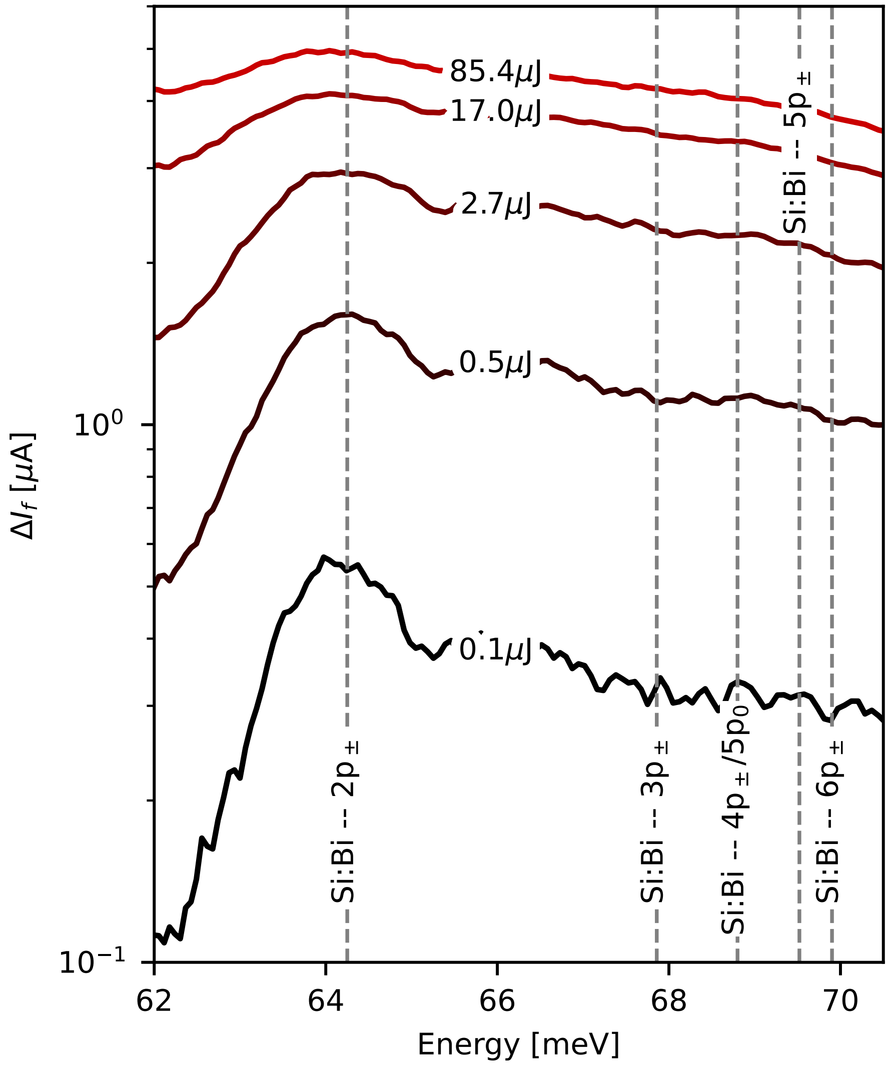

Figure 5.8: Spectra taken at $T = 8\,\mathrm{K}$ and $V_f = 1\,\mathrm{V}$ for increasing macropulse energy. Under these conditions PTIS and ground state impact ionisation are both suppressed. A direct ground state ionisation process occurs in the sample at high power FEL illumination. This could be attributed to a warming of the substrate.

found. The average diameter of the $2p_\pm$ orbital state is reported to be 27.08 nm [68]. There is therefore a 4 % probability that a randomly selected bismuth donor is isolated from its nearest neighbour such that their excited states do not overlap and hybridise. If the resonant peak fitted to in fig. 5.7 can be attributed only isolated bismuth centres, the fraction of those centres that are resonantly ionised at any time during the macropulse is 1 %.

5.5 Conclusions

The electrical detection of isolated bismuth orbital transitions has been demonstrated in an ion-implanted SOI device for the first time. The observed spectral linewidth of the $1s(A_1) \rightarrow 2p_\pm$ transition in the impact ionisation spectroscopy (IIS) suggests severe broadening has occurred. This is likely due to the high concentration of active bismuth centres in the device. Of the 6×10^5 active bismuth centres in the device channel, only 2.4×10^4 have sufficiently non-overlapping $2p_\pm$ states. A lower density of implanted bismuth into a comparable SOI substrate would likely produce transitions that are less inhomogeneously broadened by removing the band of states formed by the high density doping.

The optimum resonant photocurrent signal was found at a forced voltage bias where significant space charge is expected to have been built up at the injecting contact. At this bias the remaining voltage drop in the bulk of the channel agrees with the theoretically predicted threshold for ground state impact ionisation. Previously, electrically detected orbital transitions had only been reported as being achieved via PTIS. The results here suggest that orbital state readout can be achieved at temperatures below those required for PTIS via preferential impact ionisation of the donor excited states, termed here has IIS. This detection mechanism could prove to be a viable means of measuring the orbital dynamics of far fewer hydrogenic donors in silicon at low temperatures where the quantum coherence time is expected to be longer.

Chapter 6

Conclusions and Future work

6.1 Conclusions

Systems of few donors placed with high spatial accuracy in silicon devices have been introduced as a platform with great potential for quantum applications. Throughout this thesis steps toward the detection and control of the orbital states of fewer donors in such systems are taken.

In chapter 3, the statistics to compute the probability of suitable multi-species qubit clusters is derived for systems of hydrogenic dopants introduced by broad area ion implantation. It is found that, even a simple system whereby the orbital excitation of a dopant of one species modulates an exchange interaction with electron spins bound to donors of another species, the probability of such clusters occurring with suitable neighbouring distances is low. There is however an optimum implant configuration to be found which improves over bulk doping at the ideal concentration and the method outlined to compute this may be found to be useful in other inhomogeneous multi-species point process problems whereby inhomogeneity is along only one axis.

In chapter 4, electrically detected free electron laser (FEL) spectroscopy is performed on a high purity, high resistivity silicon sample whereby the only donors present are a background concentration of phosphorus. A transient current is detected through capacitor plates either side of the sample upon exposure to coherent pulses of THz radiation of a wavelength resonant with orbital transitions of the phosphorus bound electrons. The coherent dynamics of two transitions, $1s(A_1) \rightarrow 2p_{\pm}$ and the $1s(A_1) \rightarrow 3p_{\pm}$ are measured over a broad high magnetic field range where such dynamics has not been previously measured. The times measured are smaller than expected, even at low field. This is likely due to the raised sample temperature required for photo-thermal ionisation spectroscopy (PTIS) to ionise excited state donors. At higher magnetic field a further reduction in coherence time is measured. This could be attributed to enhanced relaxation mechanisms mediated by intra-valley f and g phonons which have energies resonant between the excited state and different lower energy states when at high magnetic field.

In the final chapter, a nanoscale, silicon on insulator device is fabricated to contain less than 1 million electrically active ion implanted bismuth donors in the optically active region of the device. This, scaled down architecture approaches a structure that would be possible to dope with single ion implanted donors in the future. Orbital transitions indicative of isolated bismuth donors were measured using a similar technique used in chapter 4, only this time with wire-bonded contacts to heavily phosphorus doped silicon leads that meet the micron scale Si:Bi channel. The chosen bismuth concentration implanted into the device resulted in an electrically active bismuth concentration after post implant activation anneal that was not conducive to observing the orbital state transitions of single bismuth donors as the bismuth donors were too close (13.54 nm) on average to other active bismuth donors. The concentration was deemed too high due to the broadened spectral linewidths observed. Using the statistics derived in chapter chapter 3, it is estimated that the resonant signal observed was due to only 2.4×10^4 of the 6×10^5 bismuth donors in the device channel. The fact that a spectral response was observed in this study at the expected isolated $2p_{\pm}$ frequency at all, motivates the fabrication of further scaled down nanoscale devices of a similar architecture whereby coherent dynamics measurements can be made of a single donor orbital state transitions. Knowledge of such dynamics is key for any qubit gating system relying on the orbital excitation of donor electrons.

Overall, it can be concluded that implanted donors in electrically contacted silicon devices can be incorporated with enough such that the orbital state transitions are measurable with on-chip detection. There is clear room for improvement with regards to the orbital transition spectrum quality due to a choice implant density too great for annealing quality achieved. This work could be followed by an annealing study that need not rely on repeated trips to beam line facilities for characterisation but could use incoherent spectroscopy such as Fourier transform infrared (FTIR) (can also be electrically detected also) to determine the presence of isolated donors. The coherent dynamics of a single donor (free of inhomogeneous broadening) orbital could be studied at temperatures lower than those required for PTIS using impact ionisation spectroscopy (IIS) thus demonstrating the longest time it could mediate a spin exchange in Stoneham Fisher Greenland (SFG)-like spin qubit scheme. There may even be magnetic fields in which the excited orbital is further shielded from phonon decay such as the intra-valley phonons investigated in chapter 4. During the course of this PhD, development of single ion implantation tools has increased with multiple groups [34,37,69] working to develop tools to controllably implant a broad range of impurity species with highly deterministic placement and number. This will undoubtedly accelerate the rate at which single to few impurity solid state quantum devices can be produced, characterised and optimised.

6.2 Rapid prototyping of single implanted nanoscale silicon devices

Aside from studying the coherent dynamics of single donor electron atomic transitions, there are other nanoscale devices whose function relies on the presence of deterministically positioned single defects. Single atom transistors much like single electron transistors have applications as highly sensitive charge and temperature sensors as well as applications in quantum information storage, processing and transmission. [20] Arrays of single atoms positioned with high precision are also of great interest because this is the configuration of donors qubits required for controlled spin exchange interaction in a solid state quantum computer. Arrays of donors are also relevant in the field of Hubbard band physics where the metal-insulator transition is studied. [69] Single ion implantation presents a technique that is highly flexible in terms of possible ion sources available and in doping geometry due to it being a direct write technique. No lithographic masking is required. Combining the use of a low current focused ion beam (FIB) with the ability to detect single ion impacts, one achieves a relatively high spatial accuracy of donor placement ($<$20 nm [34]) suitable for test-bed spin qubit devices (where appropriate spacing may be achieved stochastically) or for solid state qubit schemes such as the flip-flop qubit [70] which uses longer-range dipole-dipole coupling to entangle qubits. One also reduces the uncertainty in the number of ions per implant site that would otherwise vary due to the Poisson statistics describing the number of ions in a particular unblanking pulse.

On chip detection of single ions would be an excellent way to detect single implanted ions in conjunction with external detection techniques to further improve the counting statistics and confirm that implantation has occurred in the intended region of space i.e. into a nano-scale resistor/transistor channel. This section presents the first step towards realising single donor implant detection in a nano-scale silicon-on-insulator field effect transistor (SOIFET) device.

Alongside the fabrication of the silicon-on-insulator (SOI) Van der Pauw (VdP) used in chapter 5, a set of $1\,\mu\mathrm{m}^2$ channel, back-gated SOIFET samples were also prepared to be Bi implanted by single ion implantation (SII) and characterised by FEL spectroscopy however this experiment was not carried out in the time frame of this thesis. This SOI material had a much thinner, 200 nm buried oxide (BOX) and the Si device layer was further thinned using reactive ion etching (RIE) to 30 nm. Two-terminal mesa structures were etched into the thinned device layer and the channel was masked prior to a high fluence phosphorus broad area ion implant which was then annealed. These phosphorus doped leads define the undoped (background p-type) channel and are electrically contacted with aluminium pads like in chapter 5. Electrical contact to the handle silicon used as a gate electrode was made via the conductive silver paint used to stick the sample to a PCB. The field effect transistor (FET) was loaded into the chamber of an Ionoptika Q-One single ion implanter at room temperature and connected to two DC voltage supplies to supply a source-gate and source-drain voltage and with a transimpedance amplifier monitoring the source-drain current over the course of successive ion implantations into the device channel. Operation of the single ion implanter was carried out by Dr Nathan Cassidy.

The sensitivity of the SOIFET to the implantation of 50 keV Bi ions was such that pulses containing as few as 10 ions on average resulted in measurable current transients through the device as shown in fig. 6.1. With subsequent implants the channel becomes progressively damaged due to the generation of interstitial-vacancy pairs in the silicon lattice. The resistivity of the channel increases and the device becomes less sensitive to further implant events. To achieve deterministic implantation of a single ion, the average number of ions in the pulse must be much less than 1. This way, when an impact event is detected the probability that more than one ion was in that pulse becomes negligible.

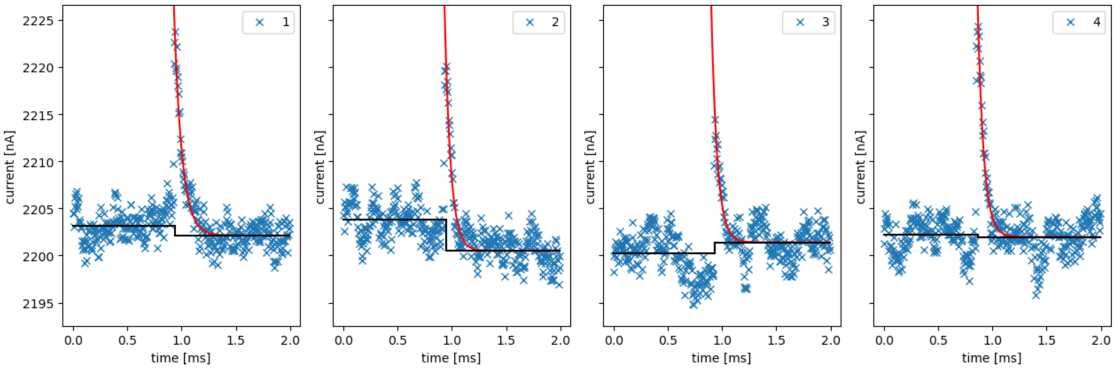

Figure 6.1: Current flowing through the SOIFET during four sequential exposures to ion pulses containing 10 ± 3 Bismuth atoms

Although sensitivity to 1 ion was not demonstrated with this device, as few as 5 ions should have been detectable assuming the transient current amplitude scales linearly with the number of ions in the pulse. There are many ways that the set-up could have been improved. If the device current transient is larger than that show in fig. 6.1 but faster than 5 us, the Stanford research SR5700 transimpedance amplifier with a 1 MHz bandwidth limits the circuit response to transient rise-times longer than 1 us. The NI cDAQ analogue input module used to digitise the source-drain current also had a sample rate limited to 200 kS/s which would make it difficult to capture device responses faster than 5 us.

This preliminary study demonstrates the viability of on-chip detection and placement of few implanted donors into a nanoscale silicon device. Following the device study presented in chapter 5 it is entirely reasonable to progress with the characterisation of devices sensitive to the orbital state of fewer/single implanted donors introduced by single ion implantation.

6.3 Electrically detected 3-pulse orbital dynamics

In chapter 4, two pulse, Ramsey spectroscopy is performed on a high purity bulk silicon sample to measure the coherent dynamics of the background, spatially isolated phosphorus bound donor electrons. The current response in the contactless electrical measurement is that due to the ionisation of an ensemble of two-level systems. The dynamics of such an ensemble is susceptible to inhomogeneous broadening effects caused by individual oscillators in the ensemble having different resonant frequencies. i.e:

$$\frac{1}{T_2 * 2} = \frac{1}{T_2} + W \tag{6.1}$$

To discern the homogeneous dephasing time (T_2) from inhomogeneous broadening (W) the experimental setup could be adapted to produce a sequence of 3 pulses whereby the middle pulse has a pulse area that undoes the loss in phase coherence caused by the oscillators in the ensemble having different resonant frequencies. As the two level systems come back into phase after the so called 'time reversal' pulse they emit radiation know as a Hahn echo. This is the so called Hahn echo pulse sequence. The third and final pulse in the sequence projects the ensemble, rephased, Bloch vector onto the z-axis as it does in the 2-pulse experiment, only this time, without the additional dephasing caused by inhomogeneous broadening.

Measurements of the dynamics of donor orbital states using a Hahn echo pulse sequences have only been performed in the time domain and optically detecting the emitted 'echo'. The use of an appropriate 3-pulse sequence to distinguish between pure dephasing effects and inhomogeneous broadening should be explored for frequency domain measurements to see if there is a similar efficiency to be gained over time domain measurement.

References

[1] A. M. Stoneham, A. J. Fisher, and P. T. Greenland, "Optically driven silicon-based quantum gates with potential for high-temperature operation," *Journal of Physics: Condensed Matter*, vol. 15, no. 27, p. L447, 2003.

[2] B. Murdin, J. Li, M. Pang, E. Bowyer, K. Litvinenko, S. Clowes, H. Engelkamp, C. Pidgeon, I. Galbraith, N. Abrosimov, H. Riemann, S. Pavlov, H.-W. Hübers, and P. Murdin, "Si:P as a laboratory analogue for hydrogen on high magnetic field white dwarf stars," *Nature Communications*, vol. 4, p. 1469, 2013.

[3] G. M. Moore, "Cramming more components onto integrated circuits With unit cost," *Electronics*, vol. 38, no. 8, p. 114, 1965.

[4] G. E. Moore, "Progress in digital integrated electronics [Technical literaiture, Copyright 1975 IEEE. Reprinted, with permission. Technical Digest. International Electron Devices Meeting, IEEE, 1975, pp. 11-13.]," *IEEE Solid-State Circuits Society Newsletter*, vol. 11, pp. 36–37, sep 2006.

[5] P. S. Peercy, "The drive to miniaturization," *Nature*, vol. 406, no. 6799, pp. 1023–1026, 2000.

[6] B. Yu, L. Chang, S. Ahmed, H. Wang, S. Bell, C. Y. Yang, C. Tabery, C. Ho, Q. Xiang, T. J. King, J. Bokor, C. Hu, M. R. Lin, and D. Kyser, "FinFET scaling to 10 nm gate length," *Technical Digest - International Electron Devices Meeting*, pp. 251–254, 2002.

[7] R. P. Feynman, “There’s plenty of room at the bottom [data storage],” *Journal of Microelectromechanical Systems*, vol. 1, pp. 60–66, mar 1992.

[8] D. P. DiVincenzo, “The Physical Implementation of Quantum Computation,” *Fortschritte der Physik*, vol. 48, pp. 771–783, sep 2000.

[9] P. Shor, “Algorithms for quantum computation: discrete logarithms and factoring,” *Proceedings 35th Annual Symposium on Foundations of Computer Science*, pp. 124–134, 1994.

[10] L. K. Grover, “A fast quantum mechanical algorithm for database search,” *Proceedings of the twenty-eighth annual ACM symposium on Theory of computing - STOC ’96*, pp. 212–219, 1996.

[11] S. Slussarenko and G. J. Pryde, “Photonic quantum information processing: A concise review,” *Applied Physics Reviews*, vol. 6, no. 4, 2019.

[12] P. Krantz, M. Kjaergaard, F. Yan, T. P. Orlando, S. Gustavsson, and W. D. Oliver, “A quantum engineer’s guide to superconducting qubits,” *Applied Physics Reviews*, vol. 6, jun 2019.

[13] M. H. Devoret and J. M. Martinis, “Implementing Qubits with Superconducting Integrated Circuits,” *Quantum Information Processing*, vol. 3, pp. 163–203, oct 2004.

[14] M. Saffman, “Quantum computing with atomic qubits and Rydberg interactions: progress and challenges,” *Journal of Physics B: Atomic, Molecular and Optical Physics*, vol. 49, p. 202001, oct 2016.

[15] J. Gorman, D. G. Hasko, and D. A. Williams, “Charge-qubit operation of an isolated double quantum dot,” *Physical Review Letters*, vol. 95, no. 9, pp. 1–4, 2005.

[16] D. Kim, D. R. Ward, C. B. Simmons, J. K. Gamble, R. Blume-Kohout, E. Nielsen, D. E. Savage, M. G. Lagally, M. Friesen, S. N. Coppersmith, and M. A. Eriksson, "Microwave-driven coherent operation of a semiconductor quantum dot charge qubit," *Nature Nanotechnology*, vol. 10, no. 3, pp. 243–247, 2015.

[17] P. Kok, W. J. Munro, K. Nemoto, T. C. Ralph, J. P. Dowling, and G. J. Milburn, "Linear optical quantum computing with photonic qubits," *Reviews of Modern Physics*, vol. 79, pp. 135–174, jan 2007.

[18] C. Nayak, S. H. Simon, A. Stern, M. Freedman, and S. Das Sarma, "Non-Abelian anyons and topological quantum computation," *Reviews of Modern Physics*, vol. 80, pp. 1083–1159, sep 2008.

[19] B. E. Kane, "A silicon-based nuclear spin quantum computer," *Nature*, vol. 393, no. 6681, pp. 133–137, 1998.

[20] M. T. Mądzik, A. Laucht, F. E. Hudson, A. M. Jakob, B. C. Johnson, D. N. Jamieson, K. M. Itoh, A. S. Dzurak, and A. Morello, "Conditional quantum operation of two exchange-coupled single-donor spin qubits in a MOS-compatible silicon device," *Nature Communications*, vol. 12, p. 181, jun 2020.

[21] L. C. Hollenberg, A. S. Dzurak, C. Wellard, A. R. Hamilton, D. J. Reilly, G. J. Milburn, and R. G. Clark, "Charge-based quantum computing using single donors in semiconductors," *Physical Review B - Condensed Matter and Materials Physics*, vol. 69, no. 11, pp. 2–5, 2004.

[22] M. Fuechsle, J. A. Miwa, S. Mahapatra, H. Ryu, S. Lee, O. Warschkow, L. C. L. Hollenberg, G. Klimeck, and M. Y. Simmons, "A single-atom transistor," *Nature Nanotechnology*, vol. 7, no. 4, pp. 242–246, 2012.

[23] D. Karaiskaj, J. A. H. Stotz, T. Meyer, M. L. W. Thewalt, and M. Cardona, “Impurity Absorption Spectroscopy in Si28: The Importance of Inhomogeneous Isotope Broadening,” *Physical Review Letters*, vol. 90, p. 186402, may 2003.

[24] K. Saeedi, S. Simmons, J. Z. Salvail, P. Dluhy, H. Riemann, N. V. Abrosimov, P. Becker, H.-J. Pohl, J. J. L. Morton, and M. L. W. Thewalt, “Room-Temperature Quantum Bit Storage Exceeding 39 Minutes Using Ionized Donors in Silicon-28,” *Science*, vol. 342, no. 6160, pp. 830–833, 2013.

[25] A. M. Tyryshkin, S. Tojo, J. J. Morton, H. Riemann, N. V. Abrosimov, P. Becker, H. J. Pohl, T. Schenkel, M. L. Thewalt, K. M. Itoh, and S. A. Lyon, “Electron spin coherence exceeding seconds in high-purity silicon,” *Nature Materials*, vol. 11, no. 2, pp. 143–147, 2012.

[26] A. Morello, J. J. Pla, F. A. Zwanenburg, K. W. Chan, K. Y. Tan, H. Huebl, M. Möttönen, C. D. Nugroho, C. Yang, J. A. Van Donkelaar, A. D. Alves, D. N. Jamieson, C. C. Escott, L. C. Hollenberg, R. G. Clark, and A. S. Dzurak, “Single-shot readout of an electron spin in silicon,” *Nature*, vol. 467, no. 7316, pp. 687–691, 2010.

[27] B. Koiller, X. Hu, S. Das Sarma, and B. Koiller, “Exchange in Silicon-Based Quantum Computer Architecture,” *Physical Review Letters*, vol. 88, no. 2, p. 4, 2002.

[28] Y. Chen, “Nanofabrication by electron beam lithography and its applications: A review,” *Microelectronic Engineering*, vol. 135, pp. 57–72, 2015.

[29] N. Ravi Kiran, M. Chauhan, S. K. Sharma, S. Ghosh, and K. E. Gonsalves, “Resists for Helium Ion Beam Lithography: Recent Advances,” *ACS Applied Electronic Materials*, vol. 2, no. 12, pp. 3805–3817, 2020.

[30] N. V. Abrosimov, D. G. Aref’Ev, P. Becker, H. Bettin, A. D. Bulanov, M. F. Churbanov, S. V. Filimonov, V. A. Gavva, O. N. Godisov, A. V. Gusev, T. V.

Kotereva, D. Nietzold, M. Peters, A. M. Potapov, H. J. Pohl, A. Pramann, H. Riemann, P. T. Scheel, R. Stosch, S. Wundrack, and S. Zakel, "A new generation of 99.999% enriched 28Si single crystals for the determination of Avogadro's constant," *Metrologia*, vol. 54, no. 4, pp. 599–609, 2017.

[31] D. Holmes, B. C. Johnson, C. Chua, B. Voisin, S. Kocsis, S. Rubanov, S. G. Robson, J. C. McCallum, D. R. McCamey, S. Rogge, and D. N. Jamieson, "Isotopic enrichment of silicon by high fluence 28Si- ion implantation," *Physical Review Materials*, vol. 5, no. 1, pp. 1–8, 2021.

[32] K. Tang, H. S. Kim, A. N. Ramanayaka, D. S. Simons, and J. M. Pomeroy, "Targeted enrichment of 28 Si thin films for quantum computing," *Journal of Physics Communications*, vol. 4, p. 035006, mar 2020.

[33] A. J. Mayur, M. D. Sciacca, A. K. Ramdas, and S. Rodriguez, "Redetermination of the valley-orbit (chemical) splitting of the 1s ground state of group-V donors in silicon," *Physical Review B*, vol. 48, no. 15, pp. 10893–10898, 1993.

[34] C. Babin, R. Stöhr, N. Morioka, T. Linkewitz, T. Steidl, R. Wörnle, D. Liu, E. Hesselmeier, V. Vorobyov, A. Denisenko, M. Hentschel, C. Gobert, P. Berwian, G. V. Astakhov, W. Knolle, S. Majety, P. Saha, M. Radulaski, N. T. Son, J. Ul-Hassan, F. Kaiser, and J. Wrachtrup, "Fabrication and nanophotonic waveguide integration of silicon carbide colour centres with preserved spin-optical coherence," *Nature Materials*, vol. 21, no. 1, pp. 67–73, 2022.

[35] N. Cassidy, P. Blenkinsopp, I. Brown, R. J. Curry, B. N. Murdin, R. Webb, and D. Cox, "Single Ion Implantation of Bismuth," *physica status solidi (a)*, vol. 218, p. 2000237, jan 2021.

[36] T. Schenkel, A. Persaud, S. J. Park, J. Meijer, J. R. Kingsley, J. W. McDonald, J. P. Holder, J. Bokor, and D. H. Schneider, "Single ion implantation

for solid state quantum computer development," *Journal of Vacuum Science and Technology B: Microelectronics and Nanometer Structures*, vol. 20, no. 6, pp. 2819–2823, 2002.

[37] W. Schnitzler, G. Jacob, R. Fickler, F. Schmidt-Kaler, and K. Singer, "Focusing a deterministic single-ion beam," *New Journal of Physics*, vol. 12, pp. 0–14, 2010.

[38] D. N. Jamieson, C. Yang, T. Hopf, S. M. Hearne, C. I. Pakes, S. Prawer, M. Mitic, E. Gauja, S. E. Andresen, F. E. Hudson, A. S. Dzurak, and R. G. Clark, "Controlled shallow single-ion implantation in silicon using an active substrate for sub- 20-keV ions," *Applied Physics Letters*, vol. 86, no. 20, pp. 1–3, 2005.

[39] T. Shinada, T. Kurosawa, H. Nakayama, Y. Zhu, M. Hori, and I. Ohdomari, "A reliable method for the counting and control of single ions for single-dopant controlled devices," *Nanotechnology*, vol. 19, p. 345202, aug 2008.

[40] J. Lyding, T.-C. Shen, J. Hubacek, J. Tucker, and G. Abeln, "Nanoscale patterning and oxidation of H-passivated Si(100)-2 x 1 surfaces with an ultra-high vacuum scanning tunneling microscope," *Applied Physics Letters*, vol. 64, no. 15, pp. 2010–2012, 1994.

[41] O. Warschkow, N. J. Curson, S. R. Schofield, N. A. Marks, H. F. Wilson, M. W. Radny, P. V. Smith, T. C. Reusch, D. R. McKenzie, and M. Y. Simmons, "Reaction paths of phosphine dissociation on silicon (001)," *Journal of Chemical Physics*, vol. 144, no. 1, 2016.

[42] T. J. Stock, O. Warschkow, P. C. Constantinou, J. Li, S. Fearn, E. Crane, E. V. Hofmann, A. Kölker, D. R. Mckenzie, S. R. Schofield, and N. J. Curson, "Atomic-Scale Patterning of Arsenic in Silicon by Scanning Tunneling Microscopy," *ACS Nano*, vol. 14, no. 3, pp. 3316–3327, 2020.

[43] P. T. Greenland, G. Matmon, B. J. Villis, E. T. Bowyer, J. Li, B. N. Murdin, A. F. Van Der Meer, B. Redlich, C. R. Pidgeon, and G. Aeppli, "Quantitative analysis of electrically detected Ramsey fringes in P-doped Si," *Physical Review B - Condensed Matter and Materials Physics*, vol. 92, no. 16, pp. 1–9, 2015.

[44] J. H. Booske, R. J. Dobbs, C. D. Joye, C. L. Kory, G. R. Neil, G. S. Park, J. Park, and R. J. Temkin, "Vacuum electronic high power terahertz sources," *IEEE Transactions on Terahertz Science and Technology*, vol. 1, no. 1, pp. 54–75, 2011.

[45] Q. Lu, D. Wu, S. Sengupta, S. Slivken, and M. Razeghi, "Room temperature continuous wave, monolithic tunable THz sources based on highly efficient mid-infrared quantum cascade lasers," *Scientific Reports*, vol. 6, no. February, pp. 1–7, 2016.

[46] K. Reimann, R. P. Smith, A. M. Weiner, T. Elsaesser, and M. Woerner, "Direct field-resolved detection of terahertz transients with amplitudes of megavolts per centimeter," *Optics Letters*, vol. 28, no. 6, p. 471, 2003.

[47] S. G. Pavlov, R. K. Zhukavin, E. E. Orlova, V. N. Shastin, A. V. Kirsanov, H. W. Hübers, K. Auen, and H. Riemann, "Stimulated emission from donor transitions in silicon," *Physical Review Letters*, vol. 84, no. 22, pp. 5220–5223, 2000.

[48] M. A. Van Loon, N. Stavrias, N. H. Le, K. L. Litvinenko, P. T. Greenland, C. R. Pidgeon, K. Saeedi, B. Redlich, G. Aeppli, and B. N. Murdin, "Giant multiphoton absorption for THz resonances in silicon hydrogenic donors," *Nature Photonics*, vol. 12, no. 3, pp. 179–184, 2018.

[49] H. W. Jongbloets, M. J. Van De Steeg, J. H. Stoelinga, and P. Wyder, "Temperature dependence of the photothermal conductivity of semiconductors at

low temperatures," *Journal of Physics C: Solid State Physics*, vol. 13, no. 11, pp. 2139–2145, 1980.

[50] B. Dierickx, E. Simoen, and G. Declerck, "Transient response of silicon devices at 4.2 K. I. Theory," *Semiconductor Science and Technology*, vol. 6, pp. 896–904, sep 1991.

[51] U. F. Edgal and J. D. Wiley, "Near-neighbor configuration and impurity-cluster size distribution in a Poisson ensemble of monovalent impurity atoms in semiconductors," *Physical Review B*, vol. 27, no. 8, 1983.

[52] S. Torquato, B. Lu, and J. Rubinstein, "Nearest-neighbor distribution functions in many-body systems," 1990.

[53] D. Moltchanov, "Distance distributions in random networks," *Ad Hoc Networks*, vol. 10, pp. 1146–1166, aug 2012.

[54] E. Crane, T. Crane, N. H. Le, A. Schuckert, A. J. Fisher, N. H. Le, K. Stockbridge, S. Chick, and A. J. Fisher, "Optically Controlled Entangling Gates in Randomly Doped Silicon," *Physical Review B*, vol. 100, pp. 1–14, feb 2019.

[55] T. Peach, K. Homewood, M. Lourenco, M. Hughes, K. Saeedi, N. Stavrias, J. Li, S. Chick, B. Murdin, and S. Clowes, "The Effect of Lattice Damage and Annealing Conditions on the Hyperfine Structure of Ion Implanted Bismuth Donors in Silicon," *Advanced Quantum Technologies*, vol. 0, p. 1800038, jun 2018.

[56] P. Loudon and R. Loudon, *The Quantum Theory of Light.* Oxford science publications, Clarendon Press, 1983.

[57] N. F. Ramsey, "A molecular beam resonance method with separated oscillating fields," *Physical Review*, vol. 78, no. 6, pp. 695–699, 1950.

[58] K. Litvinenko, E. Bowyer, P. Greenland, N. Stavrias, J. Li, R. Gwilliam, B. Villis, G. Matmon, M. Pang, B. Redlich, a.F.G. van der Meer, C. Pidgeon, G. Aeppli, and B. Murdin, "Coherent creation and destruction of orbital wavepackets in Si:P with electrical and optical read-out," *Nature Communications*, vol. 6, p. 6549, 2015.

[59] A. K. Ramdas, "Spectroscopy of shallow centers in semiconductors: Progress since 1960," *Physica B+C*, vol. 146, no. 1-2, pp. 6–18, 1987.

[60] R. K. Zhukavin, S. G. Pavlov, N. Stavrias, K. Saeedi, K. A. Kovalevsky, P. J. Phillips, V. V. Tsyplenkov, N. V. Abrosimov, H. Riemann, N. Deβmann, H. W. Hübers, and V. N. Shastin, "Influence of uniaxial stress on phonon-assisted relaxation in bismuth-doped silicon," *Journal of Applied Physics*, vol. 127, no. 3, 2020.

[61] A. Thilderkvist, M. Kleverman, G. Grossmann, and H. G. Grimmeiss, "Quadratic Zeeman effect of shallow donors in silicon," *Physical Review B*, vol. 49, no. 20, pp. 14270–14281, 1994.

[62] G. Dresselhaus, A. F. Kip, and C. Kittel, "Cyclotron Resonance of Electrons and Holes in Silicon and Germanium Crystals," *Physical Review*, vol. 98, pp. 368–384, apr 1955.

[63] B. Pajot, *Optical Absorption of Impurities and Defects in SemiconductingCrystals*, vol. 158 of *Springer Series in Solid-State Sciences.* Berlin, Heidelberg: Springer Berlin Heidelberg, 2010.

[64] L. S. Rothman, I. E. Gordon, Y. Babikov, A. Barbe, D. Chris Benner, P. F. Bernath, M. Birk, L. Bizzocchi, V. Boudon, L. R. Brown, A. Campargue, K. Chance, E. A. Cohen, L. H. Coudert, V. M. Devi, B. J. Drouin, A. Fayt, J. M. Flaud, R. R. Gamache, J. J. Harrison, J. M. Hartmann, C. Hill, J. T. Hodges, D. Jacquemart, A. Jolly, J. Lamouroux, R. J. Le Roy, G. Li, D. A. Long, O. M.

Lyulin, C. J. Mackie, S. T. Massie, S. Mikhailenko, H. S. Müller, O. V. Naumenko, A. V. Nikitin, J. Orphal, V. Perevalov, A. Perrin, E. R. Polovtseva, C. Richard, M. A. Smith, E. Starikova, K. Sung, S. Tashkun, J. Tennyson, G. C. Toon, V. G. Tyuterev, and G. Wagner, "The HITRAN2012 molecular spectroscopic database," *Journal of Quantitative Spectroscopy and Radiative Transfer*, vol. 130, pp. 4–50, 2013.

[65] N. Stavrias, K. Saeedi, B. Redlich, P. T. Greenland, H. Riemann, N. V. Abrosimov, M. L. Thewalt, C. R. Pidgeon, and B. N. Murdin, "Competition between homogeneous and inhomogeneous broadening of orbital transitions in Si:Bi," *Physical Review B*, vol. 96, no. 15, pp. 1–8, 2017.

[66] B. Aspar, M. Bruel, H. Moriceau, C. Maleville, T. Poumeyrol, A. M. Papon, A. Claverie, G. Benassayag, A. J. Auberton-Hervé, and T. Barge, "Basic mechanisms involved in the Smart-Cut® process," *Microelectronic Engineering*, vol. 36, no. 1-4, pp. 233–240, 1997.

[67] T. Peach, K. Stockbridge, J. Li, K. P. Homewood, M. A. Lourenco, S. Chick, M. A. Hughes, B. N. Murdin, and S. K. Clowes, "Enhanced diffusion and bound exciton interactions of high density implanted bismuth donors in silicon," *Applied Physics Letters*, vol. 115, p. 072102, aug 2019.

[68] J. Li, N. H. Le, K. L. Litvinenko, S. K. Clowes, H. Engelkamp, S. G. Pavlov, H.-W. Hübers, V. B. Shuman, L. Portsel, N. Lodygin, Y. A. Astrov, N. V. Abrosimov, C. R. Pidgeon, A. Fisher, Z. Zeng, Y.-M. Niquet, and B. N. Murdin, "Radii of Rydberg states of isolated silicon donors," *Physical Review B*, vol. 98, p. 085423, aug 2018.

[69] T. Shinada, M. Hori, F. Guagliardo, G. Ferrari, A. Komatubara, K. Kumagai, T. Tanii, T. Endo, Y. Ono, and E. Prati, "Quantum transport in determin-

istically implanted single-donors in Si FETs," *Technical Digest - International Electron Devices Meeting, IEDM*, pp. 697–700, 2011.

[70] G. Tosi, F. A. Mohiyaddin, V. Schmitt, S. Tenberg, R. Rahman, G. Klimeck, and A. Morello, "Silicon quantum processor with robust long-distance qubit couplings," *Nature Communications*, vol. 8, no. 1, pp. 1–11, 2017.